

©Copyright 2012

Jacob T. Vanderplas

Karhunen-Loève Analysis for Weak Gravitational Lensing

Jacob T. Vanderplas

A dissertation
submitted in partial fulfillment of the
requirements for the degree of

Doctor of Philosophy

University of Washington

2012

Reading Committee:

Andrew Connolly, Chair

Bhuvnesh Jain

Andrew Becker

Program Authorized to Offer Degree:
Department of Astronomy

University of Washington

Abstract

Karhunen-Loève Analysis for Weak Gravitational Lensing

Jacob T. Vanderplas

Chair of the Supervisory Committee:

Professor Andrew Connolly

Department of Astronomy

In the past decade, weak gravitational lensing has become an important tool in the study of the universe at the largest scale, giving insights into the distribution of dark matter, the expansion of the universe, and the nature of dark energy. This thesis research explores several applications of Karhunen-Loève (KL) analysis to speed and improve the comparison of weak lensing shear catalogs to theory in order to constrain cosmological parameters in current and future lensing surveys. This work addresses three related aspects of weak lensing analysis:

Three-dimensional Tomographic Mapping: (Based on work published in VanderPlas et al., 2011) We explore a new fast approach to three-dimensional mass mapping in weak lensing surveys. The KL approach uses a KL-based filtering of the shear signal to reconstruct mass structures on the line-of-sight, and provides a unified framework to evaluate the efficacy of linear reconstruction techniques. We find that the KL-based filtering leads to near-optimal angular resolution, and computation times which are faster than previous approaches. We also use the KL formalism to show that linear non-parametric reconstruction methods are fundamentally limited in their ability to resolve lens redshifts.

Shear Peak Statistics with Incomplete Data (Based on work published in VanderPlas et al., 2012) We explore the use of KL eigenmodes for interpolation across masked

regions in observed shear maps. Mass mapping is an inherently non-local calculation, meaning gaps in the data can have a significant effect on the properties of the derived mass map. Our KL mapping procedure leads to improvements in the recovery of detailed statistics of peaks in the mass map, which holds promise of improved cosmological constraints based on such studies.

Two-point parameter estimation with KL modes The power spectrum of the observed shear can yield powerful cosmological constraints. Incomplete survey sky coverage, however, can lead to mixing of power between Fourier modes, and obfuscate the cosmologically sensitive signal. We show that KL can be used to derive an alternate orthonormal basis for the problem which avoids mode-mixing and allows a convenient formalism for cosmological likelihood computations. Cosmological constraints derived using this method are shown to be competitive with those from the more conventional correlation function approach. We also discuss several aspects of the KL approach which will allow improved handling of correlated errors and redshift information in future surveys.

TABLE OF CONTENTS

| | Page |
|---|------|
| List of Figures | v |
| List of Tables | x |
| Chapter 1: Brief Introduction to Cosmology | 1 |
| 1.1 FLRW Metric | 3 |
| 1.2 The Friedmann Equations | 4 |
| 1.2.1 Time Dilation and Redshift | 5 |
| 1.2.2 Equation of State | 6 |
| 1.2.3 Evolving Equation of State | 8 |
| 1.2.4 Hubble Parameter | 9 |
| 1.3 Cosmological Distance Measures | 10 |
| 1.4 Standard Candles: Cosmology via Luminosity Distance | 12 |
| 1.5 The Growth of Structure | 13 |
| 1.5.1 Gravitational Instability | 14 |
| 1.5.2 Perturbation Treatment | 17 |
| 1.5.3 Matter Power Spectrum | 17 |
| 1.5.4 Putting it all together | 18 |
| 1.6 Gravitational Lensing | 20 |
| 1.6.1 Simplifying Assumptions | 20 |
| 1.6.2 Lensing Geometry | 21 |
| 1.6.3 Continuous Mass Distribution | 22 |
| 1.7 Weak Gravitational Lensing | 24 |
| 1.7.1 Mapping with Weak Lensing | 26 |
| 1.7.2 Power Spectra | 28 |
| Chapter 2: Introduction to Karhunen-Loève Analysis | 32 |
| 2.1 Notational Conventions | 32 |
| 2.2 Basis function decomposition | 33 |

| | | |
|------------|--|----|
| 2.2.1 | Fourier Series | 33 |
| 2.2.2 | Generalizing Orthonormal Bases | 35 |
| 2.3 | Karhunen-Loève Analysis | 36 |
| 2.3.1 | Derivation of Karhunen-Loève theorem | 36 |
| 2.3.2 | Eigenfunctions | 37 |
| 2.3.3 | Partial Reconstructions | 39 |
| 2.3.4 | KL in the presence of noise | 41 |
| 2.3.5 | Karhunen-Loève: theory to practice | 42 |
| 2.3.6 | KL with missing data | 44 |
| 2.4 | Karhunen-Loève Analysis and Bayesian Inference | 47 |
| 2.5 | Karhunen-Loève Analysis of Shear | 48 |
| Chapter 3: | 3D weak lensing maps with KL | 50 |
| 3.1 | Introduction | 50 |
| 3.2 | Method | 51 |
| 3.2.1 | Linear Mapping | 52 |
| 3.2.2 | KL Filtering | 53 |
| 3.3 | Results | 54 |
| 3.3.1 | Singular Values | 55 |
| 3.3.2 | Evaluation of the SVD Estimator | 56 |
| 3.3.3 | Comparison of Estimators | 58 |
| 3.3.4 | Noise Properties of Line-of-Sight Modes | 59 |
| 3.3.5 | Reconstruction of a Realistic Field | 60 |
| 3.3.6 | Scalability | 61 |
| 3.4 | Conclusion | 62 |
| Chapter 4: | Shear Peak Statistics with KL | 68 |
| 4.1 | Introduction | 68 |
| 4.2 | Karhunen-Loève Analysis of Shear | 70 |
| 4.2.1 | KL Formalism | 71 |
| 4.2.2 | KL in the Presence of Noise | 72 |
| 4.2.3 | Computing the Shear Correlation Matrix | 73 |
| 4.2.4 | Which Shear Correlation? | 74 |
| 4.2.5 | Interpolation using KL Modes | 75 |
| 4.3 | Testing KL Reconstructions | 76 |
| 4.3.1 | KL Decomposition of a Single Field | 78 |

| | | |
|-------------|---|-----|
| 4.3.2 | Testing KL Interpolation | 80 |
| 4.4 | Shear Peak Statistics | 86 |
| 4.4.1 | Aperture Mass Peaks | 87 |
| 4.4.2 | The Effects of Masking | 88 |
| 4.4.3 | M_{ap} Signal-to-Noise | 90 |
| 4.5 | Discussion | 91 |
| 4.5.1 | M_{ap} Peak Distributions | 91 |
| 4.5.2 | Remaining Questions | 97 |
| Chapter 5: | Application to COSMOS lensing data | 99 |
| 5.1 | Introduction | 99 |
| 5.2 | Two-point Statistics in Weak Lensing | 100 |
| 5.3 | KL for Parameter Estimation | 101 |
| 5.3.1 | Shear Noise Properties | 103 |
| 5.3.2 | Constructing the Covariance Matrix | 104 |
| 5.3.3 | Cosmological Likelihood Analysis with KL | 105 |
| 5.4 | COSMOS data | 106 |
| 5.4.1 | Intrinsic Ellipticity estimation | 110 |
| 5.4.2 | Whitened KL modes | 111 |
| 5.4.3 | Is our shear Gaussian? | 112 |
| 5.4.4 | Relationship to Power Spectrum | 115 |
| 5.5 | Results | 117 |
| 5.6 | Next Steps | 118 |
| Chapter 6: | Conclusion | 120 |
| | Bibliography | 123 |
| Appendix A: | Random Fields, Correlation Functions, and Power Spectra | 129 |
| A.1 | Background on Gaussian random fields | 129 |
| A.1.1 | Smoothing of Gaussian Fields | 131 |
| A.2 | Cosmological Mass Power Spectrum | 132 |
| A.2.1 | Power Spectrum Normalization | 132 |
| A.2.2 | Window functions and Measurement Covariance | 133 |
| A.2.3 | The Limber Approximation | 134 |
| A.2.4 | Applying the Limber Approximation | 136 |

| | | |
|-------------|---|-----|
| A.3 | Window Functions and their Fourier Transforms | 137 |
| A.3.1 | Gaussian Window Functions | 138 |
| A.3.2 | Top-hat Window Functions | 138 |
| Appendix B: | Efficient Implementation of the SVD Estimator | 140 |
| B.0.3 | Angular and Line-of-Sight Transformations | 140 |
| B.0.4 | Tensor Decomposition of the Transformation | 142 |
| Appendix C: | Choice of KL Parameters | 144 |

LIST OF FIGURES

| Figure Number | Page |
|---|------|
| 1.1 The geometry of gravitational lensing | 22 |
| 3.1 Ordered singular values of the matrix $\widetilde{\mathbf{M}}_{\gamma\delta}$. The dotted lines show the values of n such that 99%, 99.9%, and 99.99% of the variance is preserved. The sharp drop-off near $n = 60,000$ is due to the 10^{-3} deweighting of border pixels. . . | 55 |
| 3.2 The effect of SVD truncation on a single $z = 0.6$ NFW halo in the center of the field, for three different levels of filtering. <i>left column</i> : reconstructed density parameter $\delta(\theta)$ in the $z = 0.6$ lens-plane. The true matter distribution is represented by a tight “dot” in the center of the plot. <i>right column</i> : line-of-sight profile at the central pixel. The gray shaded area shows the input density parameter. The solid line shows the E-mode signal, while the dashed line shows the B-mode signal. n gives the number of singular values used in the reconstruction (out of a total $n_{\max} = 81920$), and v_{cut} gives the amount of variance cut by the truncation (Equation 3.8); the level of filtration decreases from the top panels to the bottom panels. The bottom panels show a case of under-filtering: for small enough v_{cut} , the noise overwhelms the signal and creates spurious peaks along the line-of-sight. | 57 |
| 3.3 The effect of Wiener filtering on the same input as Figure 3.2. Here we have used both transverse (<i>top panels</i>) and radial (<i>bottom panels</i>) Wiener filtering, both down-tuned by $\alpha = 0.05$ (the value recommended by STH09). The transverse Wiener filter suppresses the response by several orders of magnitude; a closer view of the line-of-sight peak is shown in the inset plot. The radial Wiener filter gives similar angular results to the SVD filter, but takes much longer to compute. | 64 |
| 3.4 Contribution of each shear mode to the reconstruction for three different filters. The dotted line at 10^0 represents the unfiltered result. Each filtering method leads to a different weighting of the shear modes. The SVD filter, by design, completely removes higher-order modes beyond a given cutoff, while the Wiener filter deweights modes in a more gradual fashion. Note that the transverse Wiener filter deweights all modes by up to seven orders of magnitude; it has been scaled by a factor of 10^4 for this plot. The inset plot shows a closeup of the fluctuations within each “step” of the transverse filter. These fluctuations lead to angular spread in the response (see discussion in Section 3.3.3) | 65 |

| | | |
|-----|---|----|
| 3.5 | <i>left panel:</i> The radial components of the first four columns of the matrix \mathbf{V} (see section 3.2.1). This is calculated for 100 equally spaced redshift bins ($0 \leq z \leq 2.5$) in γ , and 80 bins ($0 \leq z \leq 2.0$) in δ . These orthogonal eigenmodes are analogous to radial Fourier modes. Each is labeled by its relative noise level, $n_i = (\sigma_i/\sigma_1)^{-1}$. <i>right panel:</i> The singular values σ_i associated with the 80 radial eigenmodes. | 66 |
| 3.6 | Reconstruction of an artificial shear field with the SVD filter (<i>top panels</i>), Transverse Wiener filter (<i>middle panels</i>), and Radial Wiener filter (<i>bottom panels</i>). The left column shows the projected density reconstruction across the field using each method, all smoothed with a 1-pixel wide Gaussian filter. Red circles indicate the true locations of the input halos. The right column shows the line-of-sight distributions of the twelve most massive NFW halos, labeled A-L. The masses and redshifts of the halos are listed in Table 3.1. The signal suppression of the transverse Wiener filter seen in Figure 3.3 is apparent in the color-bar scaling of the middle panels. The anomalous results seen in halo K are due to its proximity to the dewighted border. As suggested by the discussion in Section 3.3.4, none of the three methods succeed in recovering precise redshifts of the halos. | 67 |
| 4.1 | A sample of nine of the 4096 KL eigenmodes of a $1^\circ \times 1^\circ$ patch of the sky partitioned into 64×64 pixels. Black is positive, red is negative, and each mode has unit norm. The modes are calculated from the theoretical shear correlation function (see Section 4.2.3). As a consequence of the isotropy of the cosmic shear field, the covariance matrix – and thus the associated eigenmodes – are purely real (see Section 4.3.1). | 77 |
| 4.2 | The normalized power spectrum of each KL mode. For constant mode number, the figure represents a histogram of the power in that KL mode, normalized to a constant total power. KL modes represent a linear combination of Fourier modes, so that the power in each KL mode is spread over a range of ℓ values. Nevertheless, the general trend is clear: larger mode numbers are associated with larger wave numbers, and thus smaller length scales. | 79 |

- 4.3 The eigenvalues associated with the eigenmodes discussed in Figure 4.1. By construction, the eigenvalue is proportional to the sum of signal and noise within each mode. The upper figure shows the value per mode, while the lower figure shows the normalized cumulative value. The stepped-pattern evident in the upper panel is due to the presence of degenerate eigenmodes which have identical eigenvalues (e.g. modes $n = 2$ and $n = 3$, related by parity as evident in Figure 4.1). Because the eigenmodes are computed from a whitened covariance matrix (see Section 4.2.2), the noise contribution within each mode is equal to 1. Subtracting this contribution leads to the plot of signal only: this shows that the signal-to-noise ratio is above unity only for the first 17 modes. Still, as seen in the lower panel, higher modes are required: the first 17 modes account for only 12% of the signal on average. To recover 70% of the signal in a particular reconstruction requires about 1000 modes. At this point, each additional mode has a signal-to-noise ratio of less than 0.1. Such a small signal-to-noise ratio is a well-known aspect of cosmic shear studies. 81
- 4.4 This figure illustrates the reconstruction of a small patch of masked shear from simulated shear catalog. *upper panels:* The underlying noiseless shear signal (*left*), the observed, noisy shear signal (*middle*), and the unmasked reconstruction with 900 modes and $\alpha = 0.15$. The amplitude of the noise is calculated using an intrinsic ellipticity $\sigma_\epsilon = 0.3$, with an average number density of $n_{gal} = 20 \text{ arcmin}^{-2}$. The large peak in the upper portion of the figure is well-recovered by the KL reconstruction. *lower panels:* The KL reconstruction of the shear in the presence of 20% masking, with increasing number of modes n . The mask is represented by the shaded regions in panels: within these regions, the value of the shear is recovered through KL interpolation (see Section 4.2.5). We see in this progression the effect of the KL cutoff choice: using too few modes leads to loss of information, while using too many modes leads to over-fitting within the masked regions (See Appendix C for a discussion of the choice of number of modes). 82
- 4.5 Here we show the same field as in Figure 4.4, reconstructed using $n = 900$ modes, with increasing levels of mask coverage. The density of source galaxies has been increased to 100 arcmin^{-2} , typical of a space-based weak lensing survey. At this noise level, smaller halos can be detected within the unmasked KL reconstruction (upper-left panel). Even at a 50% masking level, the large peak at $(\text{RA}, \text{DEC}) = (11.9, 36.75)$ is adequately recovered. 83

- 4.6 The large-field convergence map derived using the method of Kaiser & Squires (1993) from the noiseless input shear (*upper panels*), the noisy input shear (*middle panels*), and the 900-mode, $\alpha = 0.15$ reconstruction of the noisy shear, with 20% of pixels masked out (*lower panels*). The rightmost plots of each row cover one square degree. The larger-field maps are smoothed with Gaussian filters of width 4 and 2 arcmin, while the smaller fields are unsmoothed. These plots show that even with 20% masking of the input signal, the KL interpolation procedure recovers the most significant peaks, and offers improvement over the results derived from unmasked, observed shear. This improvement will be discussed more quantitatively below. 84
- 4.7 Comparison of the masked and unmasked peak distributions. *left panel*: the peak distributions without the use of KL. The black line is the result with no masking, while the red and green lines show the two naïve methods of correcting for the mask (see Section 4.4.2). *right panel*: the masked and unmasked peak distributions after applying KL. Neither naïve method of mask-correction adequately recovers the underlying peak distribution. It is evident, however, that the KL-based interpolation procedure recovers a mass map with a similar peak distribution to the unmasked KL map. It should be noted that the unmasked peak distribution (black line, left panel) is not identical to the unmasked peak distribution after application of KL (black line, right panel). This difference is addressed in Figure 4.8. 89
- 4.8 Comparison of the distribution of M_{ap} peaks for unmasked shear, before and after filtering the field with KL (dotted line and dashed line, respectively). The peak distribution in the absence of noise is shown for comparison (solid line). It is clear that the addition of shape noise leads to many spurious M_{ap} peaks: noise peaks outnumber true peaks by nearly a factor of 10 for smaller peak heights. Filtering by KL reduces these spurious peaks by about a factor of 3, and for larger peaks leads to a distribution similar in scale to that of the noiseless peaks. 92
- 4.9 The comparison between B-mode peak distributions and the peak distributions for a shear field composed entirely of noise. As expected, the B-mode peak distributions are largely consistent with being due to noise only. Because of this, we can use B-mode peaks as a rough proxy for the noise. . . . 93

| | | |
|------|---|-----|
| 4.10 | <i>top panel:</i> The cumulative distributions of peaks in signal-to-noise, for peaks with $M_{\text{ap}}/\sigma_M > 3.25$. This is the statistic used by Dietrich & Hartlap (2010) to discriminate between cosmological models. <i>bottom panel:</i> The ratio of B-mode to E-mode peak distributions. Filtration by KL reduces the relative number of B-mode peaks by about 1/3. Because B-mode peaks are a proxy for contamination by shape noise (see Figure 4.9), this indicates that KL-filtration results in peak distributions less affected by statistical errors. KL also reduces the total number of both E and B peaks by about 2/3; this effect can also be seen in Figure 4.8. | 94 |
| 5.1 | Angular locations of the 194,976 COSMOS galaxies with photometric redshift measurements (top panel) and the 251,958 COSMOS galaxies without photometric redshift estimates (bottom panel). The masking due to bright foreground sources is evident in both panels. | 108 |
| 5.2 | Redshift distributions of the COSMOS data. The top panel shows the distribution of photometric redshifts of the shear catalog cross-matched with the COSMOS30 photometric redshift catalog (Ilbert et al., 2009), while the bottom panel includes the inferred redshift distribution of the remaining faint galaxies. | 109 |
| 5.3 | Bootstrap estimates of the shape noise for each pixel. The estimates reflect an intrinsic ellipticity of 0.393 ± 0.013 | 111 |
| 5.4 | The first nine 2D KL signal-to-noise eigenmodes for the COSMOS bright objects. This uses square pixels that are two arcminutes on a side, leading to $41 \times 40 = 1640$ pixels over the entire field. Compare these results to the KL modes shown in Figure 4.1. | 113 |
| 5.5 | The distribution of KL eigenvalues for the eigenmodes shown in Figure 5.4. There are $41 \times 40 = 1640$ pixels, but approximately 90 of these contain no sources and are part of the mask. This is reflected in the fact that the final 90 KL modes have zero eigenvalue. | 114 |
| 5.6 | The histogram of normalized coefficients $a_i/\sqrt{\lambda_i}$. If the shear is truly a Gaussian random field, this distribution should be a Gaussian with unit variance. | 115 |
| 5.7 | The Fourier power represented by each KL mode. For each KL mode number, the vertical band shows the distribution of power with angular wavenumber ℓ . In general, the larger KL modes correspond to larger values of ℓ , though there is significant mode mixing. | 116 |
| 5.8 | The posterior distribution in the (Ω_M, σ_8) plane for a 2D analysis of the bright galaxy sample. This uses 800 of the 1640 modes, such that the truncated modes have average signal-to-noise ratios of $< \sim 1/10$, and an approximate angular scale of $\ell \sim 7000$, which corresponds to 3 arcmin or 1.5 pixel-lengths. | 118 |

LIST OF TABLES

| Table Number | | Page |
|--------------|--|------|
| 3.1 | Masses and redshifts of halos in Figure 3.6. | 62 |

ACKNOWLEDGMENTS

Thanks first to my wife Cristin for supporting me during the last five years, and understanding my late nights of working and writing. Her genuine and deep love for the people in her life is a daily inspiration.

Thanks to my family: especially to my mother Gretchen for her constant encouragement and support. From collecting butterflies to growing carnivorous plants to counting the stars, she instilled in me a desire to know the world around me.

Thanks to my advisors, Andrew Connolly and Bhuvnesh Jain, for their patient mentorship. Their thoughtfulness, humor, and expectation of excellence has given me a graduate school experience that exceeded even my highest expectations.

Thanks to Andrew Becker for offering detailed and insightful comments on a draft of this work.

I am indebted to several colleagues for helpful discussions through the course of this research, including Debbie Bard, Gary Bernstein, Anna Cabre, Joerg Dietrich, Mike Jarvis, Jan Kratochvil, Tim Schrabback, Patrick Simon, Andy Taylor, Vinu Vikram, Risa Wechsler, and many others.

Support for this research was provided by DOE Grant DESC0002607, NSF Grant AST-0709394, and NASA Grant NNX07-AH07G.

DEDICATION

To my father, Hugh Vander Plas, who lost his battle with cancer just weeks before I presented this dissertation. I will always be thankful for his ceaseless support, encouragement, and willingness to listen. His loyal, loving, and faithful character will remain my highest example of how to live.

Chapter 1

BRIEF INTRODUCTION TO COSMOLOGY

By the late part of the 20th century, the standard model of Cosmology seemed to rest on firm foundations. The model, known as the Cold Dark Matter (CDM) model, consisted of a uniformly expanding universe, composed of baryonic matter, cold non-baryonic (dark) matter, and radiation, with space-time evolving according to the dynamics of Einstein's Theory of General Relativity. This dynamical description, as was realized by Alexander Friedmann, George Lemaitre, Howard Robertson, and Arthur Walker during the 1920s and 1930s, predicts a dynamic universe, where space itself must expand or contract under the influence of the energy within it. The expansion of the universe, first observed via the characteristic redshifts of distant galaxies (Hubble, 1929), was thought to be slowing under the gravitational effect of the matter within it.

Uniform expansion of space-time lent support to the notion that the early universe was filled with a hot, dense plasma from which the constituents of chemical elements formed. This theory of *Big Bang Nucleosynthesis* (BBN: Alpher et al., 1948) was, and remains, extremely successful in explaining the relative abundance of chemical elements in the universe. Another important prediction within the BBN model is that a Cosmic Background Radiation should be present, due to the photons which free-streamed once the universe cooled enough for the gas within it to no longer be ionized (Alpher & Herman, 1948). The CBR signal had been observed in detail (Smoot et al., 1992), resulting in a confirmation of the inflationary hypothesis and the standard model of cosmology.

Nonetheless, the standard model had some cracks in its foundation: cosmological probes and studies of galaxy clusters yielded widely discrepant estimates of the matter content in the universe. The implied age of the universe in the CDM model was younger than the age inferred for the oldest observed globular clusters and white dwarfs. Something needed to

change.

Observations of type Ia supernovae by Riess et al. (1998) and Perlmutter et al. (1999) offered a solution: these showed that distant supernovae were fainter than expected in a standard CDM model. This implied that the expansion of the universe was accelerating, due to a cosmological component dubbed *dark energy*. This dark energy has an effective negative pressure, which overcomes the gravitational attraction of matter and causes the expansion of space to accelerate. This additional energy component in the universe solved many of the problems posed by CDM, and is now part of the standard Λ -CDM cosmological model (Λ refers to the cosmological constant first proposed by Einstein).

Led by these supernova results, as well as new observations of the cosmic microwave background (CMB; Spergel et al., 2003), the baryon acoustic oscillations (BAO; Eisenstein et al., 2005), and other observational campaigns, the last 15 years has seen a surge in precision cosmological measurements. The dark energy postulated to explain supernova distances is now known to make up over 70% of the energy density of the universe, and have an equation of state consistent with it being due to vacuum energy or a cosmological constant (Kessler et al., 2009; Komatsu et al., 2011). Future surveys in many diverse areas of astronomy are seeking to place even tighter constraints, allowing greater insight into the nature and evolution of dark energy.

With such a wide and diverse field as Cosmology, we can't hope to offer a complete introduction of the relevant theory in this work. For a more complete discussion, there are several very well-written books available; much of the material discussed below is taken from formalism developed more fully in these works (see, e.g. Peebles, 1993; Peacock, 1999; Ryden, 2003; Longair, 2008). This chapter will cover the basic physical and mathematical background of the physical study of cosmology. We will begin with a discussion of the FLRW metric (named for Friedmann, Lemaitre, Robertson, and Walker) which describes the geometry of space-time. Next we'll move on to define the Friedmann Equations, which condense the field equations of Einstein's General Relativity to the basic pieces needed to describe the dynamics of a globally homogeneous and isotropic universe. We will then briefly discuss the relevant theory behind gravitational structure formation within this model. This paves the way to relate theory to data, using observations including cluster counts,

correlation functions, and Fourier power spectra. Finally, we will develop the equations describing gravitational lensing in the weak limit, and show how weak lensing observations can be used to gain insight into the parameters of our cosmological model. Throughout, we'll point out the relevant observational work which supports and constrains these theories.

1.1 *FLRW Metric*

The physical study of cosmology in its classical form is based on the fundamental assumption of symmetry: that the universe on the largest scales is isotropic. Homogeneity is an expression of translational symmetry: the appearance of the universe does not depend on the location of the observer. Isotropy is an expression of rotational symmetry: the appearance of the universe does not change with respect to the orientation of the observer. These assumptions are clearly incorrect at small scales – our galaxy has a much higher density of stars in the central bulge than in the outer halo, for example – but they appear to hold at the largest scales. At distance scales larger than the size of typical superclusters (about 50 Mpc or more), the distribution of quasars and galaxies reflect the nearly homogeneous and isotropic nature of large scale structure (Yadav et al., 2005; Sarkar et al., 2009). More importantly, the Cosmic Microwave Background appears homogeneous and isotropic to within one part in 10^5 , giving evidence that our assumptions of homogeneity and isotropy are well-founded for the universe as a whole (For an interesting discussion of the limits of this approach, however, see Maartens, 2011).

The most general metric for a homogeneous and isotropic space-time is due to Howard Robertson and Arthur Walker, who showed that the space-time distance ds in spherical coordinates is given by

$$ds^2 = -c^2 dt^2 + a(t)^2 [dr^2 + S_\kappa^2(r) d\Phi^2] \quad (1.1)$$

where t is the time coordinate, r and Φ are comoving spherical coordinates, $a(t)$ describes the distance scale (which may be an arbitrary function of t), and $S_\kappa^2(r)$ is the curvature

term. The curvature term depends on the curvature, κ , which may be either $+1$, -1 , or 0 :

$$S_{\kappa}(r) = \begin{cases} R \sin(r/R) & \kappa = +1 \\ r & \kappa = 0 \\ R \sinh(r/R) & \kappa = -1 \end{cases} \quad (1.2)$$

where R is the radius of curvature today. Often, the curvature sign κ and radius R are compactly expressed in a single curvature parameter k , such that $\kappa = k/|k|$ and $R = |k|^{-1/2}$.

Robertson and Walker derived the above metric from purely geometric arguments. An interesting aspect of this metric is the scale factor $a(t)$. A general homogeneous and isotropic universe is not necessarily static: it can be expanding or contracting with time. The detailed nature of this expansion cannot be derived from purely geometric means: the description of the dynamics of cosmic expansion comes from the field equations of Einstein's theory of General Relativity.

1.2 The Friedmann Equations

The Robertson-Walker metric (eq. 1.1) is a purely geometric result, where the scale factor $a(t)$ is arbitrary and unspecified. Friedmann and Lemaitre had earlier independently derived this expression from Einstein's field equations, with the addition of certain dynamical constraints on the scale factor. For this reason, the Robertson-Walker metric is often referred to as the Friedmann-Robertson-Walker metric or the Friedmann-Lemaitre-Robertson-Walker (FLRW) metric. The general relativistic constraints on the scale factor $a(t)$ are compactly expressed by the Friedmann equations¹:

$$\left(\frac{\dot{a}}{a}\right)^2 = \frac{8\pi G}{3c^2}\varepsilon + \frac{\Lambda}{3} - \frac{\kappa c^2}{a^2 R^2} \quad (1.3)$$

$$\frac{\ddot{a}}{a} = -\frac{4\pi G}{3c^2}(\varepsilon + 3P) + \frac{\Lambda}{3}. \quad (1.4)$$

where G is the gravitational constant, and c is the speed of light. The scale factor a is understood to be a function of time, with the dots representing derivatives with respect to time. By convention, the scale factor at the present day is chosen to be $a(t_0) = 1$. ε and P

¹For a derivation of the Friedmann equations from the field equations of general relativity, refer to Peebles (1993)

are the energy density and pressure of the mass-energy in the universe, and Λ represents the cosmological constant. Equations 1.3 and 1.4 are the first and second Friedmann equations, respectively. The third Friedmann equation can be easily derived from the first two:

$$\dot{\varepsilon} = -3 \frac{\dot{a}}{a} (\varepsilon + P). \quad (1.5)$$

This expression is equivalent to the first law of thermodynamics expressed for the universe as a whole.

1.2.1 Time Dilation and Redshift

General Relativity tells us that light always travels along null geodesics, that is, the space time interval in eqn. 1.1 satisfies $ds = 0$. For a light beam with no angular deflection $d\Omega$, this gives

$$dr = \frac{c}{a(t)} dt. \quad (1.6)$$

If a beam of light is emitted at time t_e and travels a comoving distance r , the time t_o that the light is observed can be found by solving

$$r = \int_{t_e}^{t_o} \frac{c}{a(t)} dt \quad (1.7)$$

If a second photon is emitted a short time later at time $t_e + \Delta t_e$, and arrives at time $t_o + \Delta t_o$, this gives

$$\begin{aligned} r &= \int_{t_e + \Delta t_e}^{t_o + \Delta t_o} \frac{c}{a(t)} dt \\ &\approx \int_{t_e}^{t_o} \frac{c}{a(t)} dt + \frac{c \Delta t_o}{a(t_o)} - \frac{c \Delta t_e}{a(t_e)}, \end{aligned} \quad (1.8)$$

where we have used a first-order approximation. Equating these two expressions gives for small Δt :

$$\Delta t_o = \Delta t_e \frac{a(t_o)}{a(t_e)}. \quad (1.9)$$

In an expanding universe, the observed time interval is longer than the time interval in the emitted frame. This *time dilation* is a general feature of space-time governed by Einstein's field equations.

The time dilation has an observable effect on emitted light: if an atom emits light with a period $P_e = \Delta t_e = \lambda_e/c$, then the observed wavelength λ_o and the emitted wavelength λ_e are related by

$$\lambda_o = \lambda_e \frac{a(t_o)}{a(t_e)}. \quad (1.10)$$

The wavelength of light is lengthened due to the expansion of space. For historical reasons, this expansion is generally parametrized using the redshift:

$$1 + z \equiv \frac{a(t_o)}{a(t_e)}. \quad (1.11)$$

Because we define $a(t_o) = 1$, we have

$$a(t_e) = \frac{1}{1 + z}. \quad (1.12)$$

Thus the redshift of a light source gives us a direct measurement of the scale factor at the time that photon was emitted. As such, it can be substituted for a as the dependent variable in the above equations with a suitable change-of-variables; we will switch between these two conventions depending on which is convenient.

1.2.2 Equation of State

The Friedmann equations can be further simplified by relating the pressure P and energy density ε in terms of a linear equation of state parameter

$$w \equiv P/\varepsilon. \quad (1.13)$$

Using this, the solution of eqn. 1.5 gives

$$\varepsilon = \varepsilon_0 a^{-3(1+w)} \quad (1.14)$$

for w constant in time. Here $\varepsilon_0 = \varepsilon(t_0)$ is the energy density today, and we have used the standard convention $a(t_0) = 1$. Given this parametrization, we can now separate the various contributions to the mass-energy of the universe and re-write eqn. 1.3 in terms of the equation of state for each:

$$\left(\frac{\dot{a}}{a}\right)^2 = \frac{8\pi G}{3c^2} \sum_w \varepsilon_{w,0} a^{-3(1+w)} \quad (1.15)$$

where $\varepsilon_{w,0}$ is the energy density of each species at present. The various possible contributions are:

Vacuum energy/Cosmological Constant: The vacuum energy or cosmological constant Λ has energy density that does not change with time. So by Equation 1.5, $P = -\varepsilon$ and $w = -1$.

General Quintessence: Quintessence is defined as any sort of matter or energy field that can balance the gravitational attraction, leading to accelerated expansion. By Equation 1.4, $\ddot{a}/a > 0$ only if $w < -1/3$. We see that the cosmological constant is a form of quintessence.

Curvature: Though it may seem strange to think about the curvature of space as having an energy density, in General Relativity the curvature is, in some sense, a stand-in for gravitational potential energy. Comparing eqns. 1.3 and 1.15, the dependence of the curvature term on scale factor $k \propto a^{-2}$ means it has an effective equation of state parameter $w = -1/3$. This makes it clear why curvature does not appear in the second Friedmann equation (eqn. 1.4): for $w = -1/3$, $\varepsilon + 3P = 0$, and the presence of curvature cannot lead to a change in the expansion rate.

Non-relativistic matter: Non-relativistic matter (often known as *cold matter*) has kinetic energy much less than its rest mass; in other words $P \sim kT \ll \varepsilon$. This corresponds to $w \ll 1$, and we will often approximate this as simply $w = 0$.

Relativistic Matter: Relativistic matter (known as *warm matter* or *hot matter*) has energy given by $E^2 = p^2c^2 + m^2c^4$, where p is the total momentum and m is the rest-mass. If $pc \ll mc^2$, we have the non-relativistic case above, and find $w \rightarrow 0$. If $pc \gg mc^2$, then in analogy to the radiation case discussed below, we find $w \rightarrow 1/3$. For general relativistic matter, this leads to $0 \leq w < 1/3$, with the exact value dependent on the energy density.

Radiation: Radiation has energy per particle proportional to the momentum times the speed of light. From basic electrodynamics, one can show that for an ideal photon gas, each spatial degree of freedom contributes equally to the energy, so that the pressure is $P = dp/dt = \varepsilon/3$. So relativistic mass-energy has $w = 1/3$.

1.2.3 Evolving Equation of State

In Equation 1.14 we show the solution of eqn. 1.5 for constant w . Another possibility (especially applicable for general quintessence models) is that the equation of state parameter w evolves with time.

$$\varepsilon(a) = \varepsilon_0 \exp \left[-3 \int_1^a \frac{1 + w(a')}{a'} da' \right]. \quad (1.16)$$

Many parametrizations of the form of $w(a)$ have been proposed. Perhaps the simplest is a model which is simply linear in the redshift z , i.e.

$$w(z) \approx w_0 + w_1 z. \quad (1.17)$$

Though simple, this parametrization is encumbered by the fact that z changes very quickly with time, especially in the early universe. A better choice is the CPL parametrization (Chevallier & Polarski, 2001; Linder, 2003), which is of the form

$$w(z) \approx w_0 + w_a \frac{z}{1+z}, \quad (1.18)$$

or equivalently

$$w(a) \approx w_0 + w_a(1-a) \quad (1.19)$$

which is linear in the scale factor rather than the redshift. Adopting this parametrization gives

$$\varepsilon(a) = \varepsilon_0 a^{-3(1+w_0+w_a)} e^{-3w_a(1-a)}. \quad (1.20)$$

One of the main goals of future cosmological surveys is to put meaningful constraints on the time-evolution of dark energy, often by placing constraints on w_1 or w_a . This will be discussed further in later sections.

1.2.4 Hubble Parameter

The first Friedmann equation (eqn. 1.3) is commonly expressed in terms of dimensionless parameters via the generalization in eqn. 1.15. If we define the Hubble parameter

$$H \equiv \frac{\dot{a}}{a}, \quad (1.21)$$

and let H_0 be the value of the Hubble parameter today, then eqn. 1.15 becomes

$$\left(\frac{H}{H_0}\right)^2 = \frac{8\pi G}{3H_0^2 c^2} \sum_w \varepsilon_{w,0} a^{-3(1+w)}. \quad (1.22)$$

The constant in front of the sum has dimensions of inverse energy density: this motivates the definition of the critical density

$$\varepsilon_c \equiv \frac{\rho_c}{c^2} \equiv \frac{3H^2 c^2}{8\pi G}, \quad (1.23)$$

where, to be explicit, both the critical densities ε_c , ρ_c , and Hubble parameter H are functions of time. With this definition, and defining the dimensionless density parameter

$$\Omega_w(t) \equiv \varepsilon_w(t)/\varepsilon_c(t) \quad (1.24)$$

the Friedmann equation can be compactly expressed

$$\left(\frac{H}{H_0}\right)^2 = \sum_w \Omega_{w,0} a^{-3(1+w)}, \quad (1.25)$$

where the subscript 0 indicates the value at present. Alternatively, we can express the Friedmann equation as simply

$$\sum_w \Omega_w(t) = 1. \quad (1.26)$$

Notice that if the sum of all components Ω_w with the exception of Ω_κ is unity, then we must have curvature $\Omega_\kappa = 0$. This shows the meaning of the critical density (eqn. 1.23): if the energy density in the universe satisfies $\epsilon > \epsilon_c$ (i.e. $\Omega > 1$), then $\kappa = +1$ and the universe is *spatially closed*. If $\epsilon < \epsilon_c$ (i.e. $\Omega < 1$), then $\kappa = -1$ and the universe is *spatially open*. If the energy density is exactly equal to the critical density, then the curvature $\kappa = 0$ and the universe is *flat*. Constraints from the Cosmic Microwave Background show that our universe is flat to a very high precision (Komatsu et al., 2011). In addition, inflationary

perturbation analysis shows that if the Universe is close to flat, it probably is flat. For this reason, in many of the below derivations we will assume for simplicity that $\Omega_\kappa = 0$ and consequently $S_\kappa(r) = r$.

For simplicity, we can limit our consideration to the principal contributors to the density of the universe: dark energy (Ω_Λ), matter (Ω_M), radiation (Ω_R), and curvature (Ω_κ). Neglecting other components gives the familiar dimensionless form of the Friedmann Equation:

$$\left(\frac{H}{H_0}\right)^2 = \Omega_{M,0} a^{-3} + \Omega_{R,0} a^{-4} + \Omega_{\kappa,0} a^{-2} + \Omega_\Lambda \quad (1.27)$$

1.3 Cosmological Distance Measures

The FLRW metric of §1.1 and the Friedmann equations of §1.2 lay the basic framework for the study of cosmology. A large portion of the history of 20th century cosmology surrounds various attempts to understand the relative contributions of matter, radiation, curvature, and dark energy to the Hubble parameter, which measures the expansion rate of the universe. The exact nature of these various contributions has far-reaching consequences, determining how, when, and where galaxies, clusters and other structure form and evolve; determining the age of the universe and the character of its evolution through time; determining cosmic abundances and the initial conditions of stellar evolution and planet formation; and determining the nature of the universe's beginning, and the possibility of its eventual end. Observational measures of these consequences allow constraints of the properties of the various $\Omega_w(z)$.

Eqn. 1.27 is simply a first-order differential equation in a : For various choices of the density parameters Ω_w , it can be solved to yield a curve describing the scale factor a as a function of time t . A straightforward route to placing observational constraints on the densities of various components, then, would require simply measuring the value of a at several times t and performing a multidimensional fit to these observed data points.

As discussed above in §1.2.1, the redshift of light offers a direct measurement of the scale factor at a given time. In order to use eqn. 1.27 to gain information about the cosmological densities Ω_w , then, we must be able to observe some property related to the time t_e of emission of these photons. To enable this, we'll introduce the concept of distances

in Cosmology.

Distance measures in cosmology are a potentially confusing subject. An excellent resource describing these can be found in Hogg (1999). Here we'll briefly define four relevant distance measures: the comoving distance, the proper distance, the angular diameter distance, and the luminosity distance.

Comoving Distance: The comoving distance is the distance r which enters into the FLRW metric, eqn. 1.1. This distance is constant for two objects moving with the expansion of space. Using the FLRW metric and setting $ds = 0$, one can show that the comoving distance for an object with redshift z is given by

$$r(z) = c \int_0^z \frac{dz'}{H(z')}. \quad (1.28)$$

Proper Distance: The proper distance $d_p(z)$ is the simultaneous separation between two objects. From the FLRW metric with time interval $dt = 0$, one can show that the proper distance is given by

$$d_p(z) = \frac{r(z)}{1+z}. \quad (1.29)$$

Angular Diameter Distance: The angular diameter distance $d_A(z)$ is the ratio of the proper size to the observed angular size (in radians) of an extended source. From the FLRW metric with $dt = dr = 0$, one can show that the angular diameter distance is given by

$$d_A(z) = \frac{S_\kappa(r)}{1+z}. \quad (1.30)$$

Luminosity Distance: The luminosity distance $d_L(z)$ relates the emitted flux of a source to the observed flux. Taking into account the angular dilution of the flux, as well as the redshifted energy of each photon and time-delay of photon arrival leads to

$$\begin{aligned} d_L(z) &= (1+z)^2 d_A(z) \\ &= (1+z) S_\kappa(r) \end{aligned} \quad (1.31)$$

By measuring one of these distances as a function of redshift, we are effectively measuring both the dependent and independent variable in the dimensionless Friedmann equation, eqn. 1.27. In this way, it is possible to constrain the combinations of cosmological parameters Ω_w that fit the data.

1.4 Standard Candles: Cosmology via Luminosity Distance

Standard candles have been one of the primary methods for measuring cosmological parameters. The earliest measure, from Edwin Hubble, used Cepheid-type variable stars that have an absolute magnitude correlated with their pulsation period (Leavitt & Pickering, 1912; Hubble, 1929). Through observations of Cepheids in nearby galaxies, Hubble found a positive correlation between the luminosity distance to each galaxy and its apparent recessional velocity, indicating a positive value for H_0 .² Using our formalism above, we can show that the rate of change of the proper distance to any object is

$$\begin{aligned} \frac{d}{dt}d_p(t) &= H(t) d_p(t) \\ &\approx H_0 d_L(t) [1 + \mathcal{O}(z)], \end{aligned} \tag{1.32}$$

where in the second line we have separated corrections of order z . Because Hubble used a sample with $z < \sim 0.005$, the zeroth-order linear fit is well within observed errors. Thus Hubble’s observations can be seen as a first attempt at constraining cosmological parameters in Equation 1.27 through the simultaneous measurement of redshift and luminosity distance.

In the 70 years after Hubble’s discovery, there were many attempts to confirm and improve upon his discovery and use it to derive tighter constraints on the slope H_0 of the Hubble relation. A large majority of these have been based on standard or standardizable candles. These standardizable candles have been based on several empirical relations, including the period-luminosity relationship of Cepheid variables (Leavitt & Pickering, 1912); on the Tully-Fisher relationship between brightness and rotation speed of spiral galaxies (Tully & Fisher, 1977); on the Faber-Jackson/Fundamental Plane relationship between

²Although Hubble does not frame this measurement in terms of the Friedmann equations, he cautiously mentions the potential relationship of the observations to the “de Sitter effect”, a predicted redshift within a particular solution of Einstein’s equations which is a special case of the FLRW metric and Friedmann equations (i.e., that with $\Omega_M = 0$, $\Omega_\kappa = 0$, and $\Omega_\Lambda = 1$).

brightness, velocity, and surface brightness for elliptical galaxies (Faber & Jackson, 1976; Djorgovski & Davis, 1987); and on the relationship between luminosity and decay timescale for type Ia supernovae (Phillips, 1993). Due to their extreme intrinsic brightness and minimal scatter in calibrated luminosity, type Ia supernovae have become a very important tool for determining cosmological parameters, but they cannot be used alone: independent measures are required to calibrate the distance scale of type-I supernovae, making all the above approaches important. Perhaps the most comprehensive study to date of these various standard candles is the HST Key project (Freedman et al., 2001), which combined the above measures and others to arrive at a value of $H_0 = 72 \pm 8$ km/s/Mpc. This is consistent with the tighter constraint from the WMAP 7-year CMB analysis, which gave $H_0 = 70.4 \pm 2.5$ km/s/Mpc.

The common theme in the above methods is that they are based on the idea of a standard candle: if we can determine the intrinsic brightness of an object as well as its redshift, then we can compare this to the apparent brightness and constrain the Hubble parameter $H(t)$. Another path to this sort of constraint comes from standard *rulers* rather than standard candles. If we know the redshift as well as the intrinsic size of an object, then we can use its apparent size to constrain cosmological parameters. One such standard ruler is given by the characteristic scales of structure in the universe.

1.5 The Growth of Structure

There are several methods of cosmological parameter estimation that rely on the idea of standard rulers. Some examples are the observation of the anisotropy scale in the Cosmic Microwave Background, and the observation of the Baryon Acoustic Oscillation scale. Another powerful method relies on detailed modeling of the growth of structure. As we will see, along with offering the possibility of a standard ruler, consideration of structure growth can offer other cosmologically interesting observables.

The distribution of density throughout the universe can be expressed in terms of the density contrast

$$\delta(\mathbf{x}, t) = \frac{\rho(\mathbf{x}, t) - \rho_b(t)}{\rho_b(t)}, \quad (1.33)$$

where the background matter density is

$$\rho_b(t) \propto \frac{1}{a(t)^3} \quad (1.34)$$

(i.e. we assume the background consists of cold matter with $w = 0$). Rearranging this definition results in expressing the density field of the universe as

$$\rho(\mathbf{x}, t) = \rho_b(t)[1 + \delta(\mathbf{x}, t)]. \quad (1.35)$$

1.5.1 Gravitational Instability

We can proceed by treating matter as an ideal fluid with a velocity field $\mathbf{u}(\mathbf{x}, t)$ and pressure $P(\mathbf{x}, t)$ (Longair, 2008). In this case, it is governed by three equations: the continuity equation, which describes conservation of mass,

$$\left(\frac{\partial \rho}{\partial t} \right)_{\mathbf{x}} + \rho \nabla_{\mathbf{x}} \cdot \mathbf{u} = 0, \quad (1.36)$$

the Euler equation, which specifies conservation of momentum,

$$\left(\frac{\partial \mathbf{u}}{\partial t} \right)_{\mathbf{x}} + (\mathbf{u} \cdot \nabla_{\mathbf{x}}) \mathbf{u} + \frac{\nabla_{\mathbf{x}} P}{\rho} = -\nabla_{\mathbf{x}} \Phi, \quad (1.37)$$

and the Poisson equation, which describes gravity in the Newtonian limit

$$\nabla_{\mathbf{x}}^2 \Phi = 4\pi G \rho. \quad (1.38)$$

Transforming to comoving coordinates $\mathbf{r} = \mathbf{x}/a(t)$, defining comoving time derivatives $d/dt \equiv \partial/\partial t + \mathbf{u} \cdot \nabla$, and expressing in terms of the dimensionless density contrast $\delta(\mathbf{r}, t)$ (eq. 1.33) gives

$$\frac{d^2 \delta}{dt^2} + 2H \frac{d\delta}{dt} = \frac{c_s^2}{a^2} \nabla_{\mathbf{r}}^2 \delta + 4\pi G \rho_b \delta \quad (1.39)$$

where $\nabla_{\mathbf{r}}^2$ indicates the Laplacian with respect to comoving coordinates (for derivation see section 11.2 of Longair, 2008).

We can gain insight by expressing this in terms of wave-like solutions of the density contrast $\delta_k(\mathbf{r}, t) \propto \exp[i(\mathbf{k} \cdot \mathbf{r} - \omega t)]$, where \mathbf{k} is the vector of spatial wave-numbers, and ω is the oscillation frequency. In terms of these Fourier modes, eqn. 1.39 becomes

$$\ddot{\delta}_k + 2H\dot{\delta}_k - \delta_k(4\pi G \rho_b - k^2 c_s^2) = 0. \quad (1.40)$$

This differential equation describes an exponentially growing (or decaying) density fluctuation, with a “drag” term governed by the Hubble parameter $H(z)$. The rate of growth of perturbations δ_k depends on the balance between the gravitational force through $4\pi G\rho_b$ and the pressure through $k^2 c_s^2$. The scale $\lambda_J = 2\pi/k_J$ where these forces balance is called the Jeans length:

$$\lambda_J \equiv c_s \sqrt{\frac{\pi}{G\rho_b}}. \quad (1.41)$$

This is the scale above which pressure cannot halt gravitational collapse. The length is directly proportional to the sound speed $c_s = \sqrt{\partial P / \partial \rho}$ and so depends on the equation of state of the total energy in the universe, as well as the average density ρ_b . The different components (radiation, matter, etc.) have different equations of state (§1.2) and evolve with different dependencies on the scale factor a , and so the Jeans length also evolves through the course of cosmic history. Thus the scale of nonlinear collapsed structure as a function of z contains information which can be used to place constraints on the components which make up the Universe.

In particular, we can consider two relevant regimes: radiation dominance and matter dominance. In the regime where radiation dominates the energy density, the equation of state $w = 1/3$ leads to $c_s^2 = c^2/3$. In a flat universe ρ_b is the critical density (eqn. 1.23) and the Jeans length for a radiation dominated universe can be expressed

$$\lambda_J^{(R)} = \frac{\pi c \sqrt{8}}{3H}. \quad (1.42)$$

This scale is on the same order as that of the horizon scale, $\lambda_s \approx 2c/(H\sqrt{3})$. This means that sub-horizon modes cannot collapse during the epoch when radiation dominates the energy of the universe.

In the matter-dominated regime, there are two possibilities: if radiation and matter are coupled, the pressure comes from the radiation while the density is dominated by matter. This gives $c_s^2 \sim c^2 \Omega_r / \Omega_M \sim c^2 (1+z) \Omega_{r,0} / \Omega_{m,0}$. Putting in numbers from WMAP (Komatsu et al., 2011), we find approximately $c_s \approx 10^{-2} c \sqrt{1+z}$. If radiation and matter are decoupled, the pressure comes from the nonzero temperature of matter itself: $c_s^2 \sim kT/m_p$ where m_p is the proton mass. Assuming the matter is in thermal equilibrium with the CMB, then temperature goes as $T \propto (1+z)$. Again using observational constraints from WMAP, we

find $c_s \approx 10^{-7} c \sqrt{1+z}$. Thus the Jeans length during the matter-dominated epoch is given by

$$\lambda_J^{(M)} \approx \lambda_J^{(R)} \sqrt{1+z} \times \begin{cases} 10^{-2} & \text{before decoupling} \\ 10^{-7} & \text{after decoupling} \end{cases} \quad (1.43)$$

The redshift of decoupling is approximately $z \sim 1100$ (for a physical argument for this, see Ryden, 2003). This means that prior to decoupling, growth below approximately sub-horizon scales is suppressed by pressure. After decoupling, the Jeans length shrinks by five orders of magnitude, allowing linear structure on this scale to form. The observable effect of this sharp transition in the growth of structure will be discussed further below.

A related question is that of the rate of structure growth on scales larger than the Jeans length. This can be addressed by defining the linear growth factor $D(t)$ such that

$$\delta(\mathbf{r}, t) = \delta_0(\mathbf{r}) D(t). \quad (1.44)$$

Using $\rho_b = \Omega_M \rho_c$ and assuming negligible pressure (i.e. scales above the Jeans length), we can rewrite eqn. 1.39 as

$$\ddot{D} + 2H\dot{D} - \frac{3}{2}\Omega_M H^2 D = 0. \quad (1.45)$$

This is a second-order differential equation, which will, in general, admit a solution with a growing mode and a decaying mode:

$$D(t) = A_1 D_1(t) + A_2 D_2(t). \quad (1.46)$$

In a flat universe dominated by matter, the Friedmann equation gives $H(t) = 2/(3t)$, leading to solutions

$$D(t) = A_1 t^{2/3} + A_2 t^{-1}. \quad (1.47)$$

The first term quickly dominates the second, and structure grows as $\delta \propto t^{2/3} \propto a$, where the last proportionality comes from solving eqn. 1.27 for a matter dominated universe.

In general, the growth factor for a flat universe is

$$D(a) \propto \int_0^a \frac{da'}{[a' H(a')]^3}, \quad (1.48)$$

where the normalization is usually chosen such that $D(a) = 1$ at the present day.

A radiation-dominated universe presents a more complicated case: eqn. 1.45 assumes the pressure is negligible compared to the gravitational force. This approximation breaks down in cases when $\Omega_M \rightarrow 0$. For these cases, we need a more involved perturbative treatment.

1.5.2 Perturbation Treatment

To explore the growth rate in a universe where Ω_M is small, we will perform a perturbation analysis of Friedmann's equations. A full discussion of this treatment can be found in Peebles (1993). Here we will briefly outline a schematic approach from Kolb & Turner (1990) which leads to the same results.

By Birkhoff's theorem (Birkhoff & Langer, 1923), a small spherical over-density can be treated as if it were an independent homogeneous universe embedded within the background. We'll assume the background is represented by a flat universe with

$$H^2 = \frac{8\pi G}{3c^2} \varepsilon_0, \quad (1.49)$$

and that a spherical perturbation has a small positive curvature

$$H^2 = \frac{8\pi G}{3c^2} \varepsilon_1 - \frac{\kappa c^2}{a^2 R_0^2}. \quad (1.50)$$

The boundary requires that the expansion rate H be equal between the two; combining these we find

$$\delta \equiv \frac{\varepsilon_1 - \varepsilon_0}{\varepsilon_0} = \frac{3\kappa c^4}{8\pi G R_0^2} \frac{1}{a^2 \varepsilon_0}. \quad (1.51)$$

For a matter-dominated universe, $\varepsilon_0 \propto a^{-3}$ which gives $\delta \propto a$ as above. For a radiation-dominated universe, $\varepsilon_0 \propto a^{-4}$ which gives $\delta \propto a^2$.

1.5.3 Matter Power Spectrum

In summary, the above results show that

- In the radiation-dominated regime, fluctuations on scales above $\lambda_J^{(R)} = (\pi c \sqrt{8})/(3H)$ grow as $\delta(a) \propto a^2$.
- In the matter-dominated regime, after decoupling, scales above $\lambda_J^{(M)} \approx 10^{-7} \lambda_J^{(R)} \sqrt{1+z}$ grow as $\delta(a) \propto a$.

The ratio of radiation density to matter density is

$$\frac{\Omega_R(z)}{\Omega_M(z)} = (1+z) \frac{\Omega_{R,0}}{\Omega_{M,0}}. \quad (1.52)$$

So before the redshift of radiation-matter equality, $z_{rm} \approx \Omega_{M,0}/\Omega_{R,0}$, radiation dominates, while after this redshift matter dominates. Thus the important scale is the horizon scale λ_{rm} at redshift $z = z_{rm}$. Modes on length-scales $k > \lambda_{rm}$ will grow as $\delta \propto a^2$ for $a < a_{rm}$, and $\delta \propto a$ for $a > a_{rm}$. Modes with length-scales $k < \lambda_{rm}$ will grow as $\delta \propto a^2$ as long as the horizon distance $d_{hor}(a) < k$, at which point the growth will be suppressed by radiation pressure. At $a > a_{rm}$, the Jeans length shrinks by a factor of about 10^5 , and modes larger than λ_J^M resume growth with $\delta \propto a$.

Thus, density modes with $k > k_{rm}$ (that is, scales smaller than the matter-radiation equality horizon scale) are suppressed by a factor of $(a_k/a_{rm})^2 \propto k^{-2}$. This motivates use of the power spectrum of density fluctuations (for details see Appendix A):

$$P_k \equiv \langle |\delta_k|^2 \rangle, \quad (1.53)$$

in theory a measurable quantity, which will have a distinct break at $k = k_{rm}$ for the reasons discussed above. In particular, if the power spectrum of primordial fluctuations is a simple power law with $P_k \propto k^n$, then after decoupling the power spectrum will be approximately

$$P_k \propto \begin{cases} k^{n-4}, & \text{for } k > k_{rm} \\ k^n, & \text{for } k < k_{rm}. \end{cases} \quad (1.54)$$

Under most inflationary scenarios, it is expected that the power spectral index $n \approx 1$ (Peacock, 1999). The normalization of the power spectrum depends on the magnitude of the primordial fluctuations, and is dependent on the cosmological model. This normalization is typically expressed in terms of the parameter σ_8 , which measures the magnitude of average fluctuations within a sphere of radius 8 Mpc. For a more thorough discussion of power spectra and the σ_8 normalization, see Appendix A.

1.5.4 Putting it all together

The sum of the above discussion paints a general picture of the growth of structure within the universe presents several concepts with readily observable consequences:

- The size and mass/length scale of clusters as a function of redshift depends on the length-scale of gravitational instability λ_J (eqn. 1.41), which in turn depends on the densities of matter and radiation in the universe. Clustering also depends on the linear growth rate $D(z)$ (eqn. 1.48) and its nonlinear extensions, which also depend on the relative cosmic densities as a function of z .
- The power spectrum of density fluctuations (eq. 1.53) has a turn-off at a length scale that is closely related to the horizon distance at the epoch of radiation-matter equality. This scale acts as a standard ruler, such that the angular diameter distance can be estimated at a particular value of z , leading to cosmological constraints through the same means as the standard candle method discussed in §1.4.
- The linear growth factor (eqn. 1.48) affects the normalization of the power spectrum. Therefore, measuring the power spectrum as a function of z leads to cosmological constraints through the dependence of $D(z)$ on cosmological parameters.

So we see that there are powerful cosmological constraints that can be obtained through the observation of the density fluctuations and clustering of matter through the universe. There are several caveats, however: the above discussion focuses on the linear approximation (that is, we discuss the behavior of perturbations of order δ , while ignoring δ^2). This is sufficient for small δ , but not for when δ is much larger than 1. At small scales, structure is well beyond the regime where this approximation holds: for example, δ for our galaxy is approximately 10^5 ! Even moderate-sized galaxy clusters (i.e. a hypothetical cluster 2Mpc across, containing 50 Milky-way sized galaxies) have δ of order $10^2 - 10^3$. Clearly, nonlinear effects must be taken into account when measuring clustering. These effects can be estimated several ways; one of the more successful is the halo model of Smith et al. (2003), which is calibrated using semi-analytic results from N-body simulations. Nonlinear effects lead to a significant boosting of power on small scales.

A second caveat is that the structure we are referring to here is that made up by the bulk of the matter in the universe: collisionless dark matter. Dark matter, being non-luminous, cannot be observed directly through emitted light. The power spectrum of luminous matter

can be theoretically mapped to the underlying mass power spectrum, but this mapping requires uncertain corrections and introduces systematic errors that are difficult to calibrate.

With careful accounting for the above two caveats, observations of the spatial distribution of luminous matter have led to interesting cosmological results. One of the most important surveys in this regard has been the Sloan Digital Sky Survey (SDSS), which measured spectra of nearly a million sources across over 8000 square degrees, leading to accurate photometric redshifts of hundreds of thousands of galaxies across over a third of the sky. Measurements of the angular power of these galaxies have been successfully used to constrain cosmology both from the nonlinear power spectrum (Tegmark et al., 2006) and the Baryon Acoustic Oscillation (BAO) signal (Eisenstein et al., 2005).

The BAO signal is another cosmological constraint based on the idea of a standard ruler. In the above discussion, we mention the role of pressure in suppressing the growth of structure before radiation and matter are decoupled. This suppression by pressure leads to acoustic oscillations in the plasma of the radiation and baryons. When the radiation and matter decouples, these oscillations freeze-out and form the seeds of baryonic structure growth. The remnants of this freeze-out can be observed in baryonic structure today, and the characteristic length scale has been used to place tight constraints on cosmological parameters (Eisenstein et al., 2005).

1.6 Gravitational Lensing

In order to circumvent the astrophysical bias involved with mapping luminous matter to the underlying dark matter, it would be preferable to observe the dark matter directly. This is where gravitational lensing can make an important contribution. Einstein's theory of General Relativity predicts that photons will be deflected in the presence of a gravitational field. Under certain circumstances, this deflection can be detected and used to learn about the nature of the gravitating matter.

1.6.1 Simplifying Assumptions

The propagation of light through a region of gravitational potential $\Phi(\vec{r})$ is, in general, a very complicated problem, only analytically solvable for potentials with various symmetries.

In cosmological contexts, however, it is safe to assume that the universe is described by a Robertson-Walker metric, with only small perturbations due to the density fluctuations described by the potential Φ . In this case, the gravitational deflection of a photon can be described by an effective index of refraction given by

$$n = 1 - \frac{2}{c^2}\Phi \quad (1.55)$$

(see Narayan & Bartelmann, 1996, and references therein). As in conventional optics, light rays are deflected in proportion to the perpendicular gradient of the refraction index, such that the deflection angle $\hat{\alpha}$ is given by

$$\hat{\alpha} = - \int_0^{D_S} \vec{\nabla}_\perp n \, dD = \frac{2}{c^2} \int_0^{D_S} \vec{\nabla}_\perp \Phi \, dD \quad (1.56)$$

where D_S is the distance from the observer to the photon source.

For a point-mass located at a distance D_L and an impact parameter b , with $D_L \gg b$ and $D_S \approx 2D_L$, equation 1.56 can be integrated to give

$$\hat{\alpha} = \frac{4GM}{bc^2} \left[1 - \frac{1}{2} \left(\frac{b}{D_L} \right)^2 + \mathcal{O} \left[\left(\frac{b}{D_L} \right)^3 \right] \right] \quad (1.57)$$

The first-order approximation is twice the deflection predicted by Newtonian gravity for a particle of arbitrary mass moving at a speed c . It is important to note here that to first order, the deflection does not depend on the distance to the lens or source. That is, for a mass distribution located at a distance $D_L \gg b$, equation 1.56 can be approximated

$$\hat{\alpha} \approx \frac{2}{c^2} \int_{D_L-\delta D}^{D_L+\delta D} \vec{\nabla}_\perp \Phi \, dD \quad (1.58)$$

for δD sufficiently greater than the size scale of the mass-distribution in question. So, to a very good approximation, the incremental deflection $\delta\hat{\alpha}$ of a photon at a given point along its trajectory is entirely due to an overdensity of matter with a thickness $2\delta D$, oriented perpendicular to the unperturbed photon trajectory. This is the *thin lens* approximation.

1.6.2 Lensing Geometry

For a mass-sheet located at a distance D_L , and a photon source located at a distance D_S (with $D_{LS} = D_S - D_L$) geometric considerations in the small-angle approximation (see

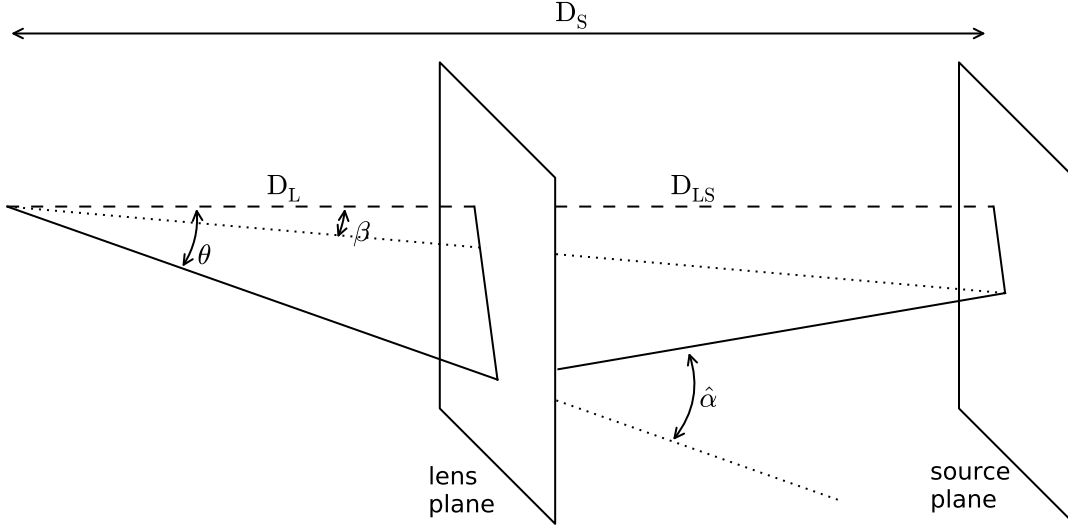


Figure 1.1: The geometry of gravitational lensing

Figure 1.1) yield the relation

$$\vec{\theta} = \vec{\beta} + \frac{D_{LS}}{D_S} \hat{\alpha} \quad (1.59)$$

where $\vec{\theta}$ and $\vec{\beta}$ are the observed and true positions of the source, respectively. Rescaling $\hat{\alpha}$ in more convenient units gives

$$\vec{\theta} = \vec{\beta} + \vec{\alpha} \quad (1.60)$$

where we have defined

$$\vec{\alpha} \equiv \frac{D_{LS}}{D_S} \hat{\alpha} \quad (1.61)$$

1.6.3 Continuous Mass Distribution

In the case of a continuous mass distribution, we can recall the remarks of section 1.6.1, and define a surface-mass density for a mass-sheet located at a redshift z_L :

$$\Sigma(\vec{\theta}, z_L) = \int_{D_L - \delta D}^{D_L + \delta D} \rho_M(\vec{\theta}, D) dD = \frac{1}{c^2} \int_{z_L - \delta z}^{z_L + \delta z} \varepsilon_M(\vec{\theta}, z) \frac{dD}{dz} dz \quad (1.62)$$

where $\varepsilon_M \equiv \rho_M c^2$ is the energy density of matter, $\vec{\theta}$ is the apparent angular position, and z and $D(z)$ are the redshift and line-of-sight distance, respectively, with $D_S = D(z_s)$.

A matter distribution $\rho_M(\vec{\theta}, z)$, and its Newtonian potential $\Phi(\vec{\theta}, z)$ are related by Poisson's equation:

$$\nabla^2 \Phi(\vec{\theta}, z) = 4\pi G \rho_M(\vec{\theta}, z) \quad (1.63)$$

It is convenient to define the unscaled lensing potential $\hat{\psi}$, given by

$$\hat{\psi}(\vec{\theta}, z_s) = \int_0^{D(z_s)} \Phi(\vec{\theta}, z(D)) \, dD = \int_0^{z_s} \Phi(\vec{\theta}, z) \frac{dD}{dz} \, dz \quad (1.64)$$

Using the approximation in equation 1.58, we can write this in terms of multiple mass-sheets, such that

$$\hat{\psi} = \sum_i \delta\hat{\psi}_i = \sum_i \int_{D_i-\delta D}^{D_i+\delta D} \Phi \, dD \quad (1.65)$$

with $D_{i+1} = D_i + 2\delta D$.

The gradient of $\hat{\psi}$ with respect to $\vec{\xi} \equiv D_L \vec{\theta}$ is

$$\vec{\nabla}_\xi \hat{\psi} = \sum_i \vec{\nabla}_\xi (\delta\hat{\psi}_i) = \sum_i \int_{D_i-\delta D}^{D_i+\delta D} \vec{\nabla}_\xi \Phi \, dD \quad (1.66)$$

Comparing this with (1.58) and (1.61) gives the incremental deflection angle in terms of the lensing potential of a mass-sheet:

$$\delta\vec{\alpha}_i = \frac{2}{c^2} \frac{D_{LS}}{D_S} \vec{\nabla}_\xi (\delta\hat{\psi}_i) \quad (1.67)$$

Further simplification can be made by rescaling the lensing potential, defining

$$\delta\psi_i = \frac{2}{c^2} \frac{D_{LS}}{D_L D_S} \delta\hat{\psi}_i \quad (1.68)$$

so that we are left with

$$\delta\vec{\alpha}_i(\vec{\theta}, z_L) = \vec{\nabla}_\theta \left(\delta\psi_i(\vec{\theta}, z_L) \right) \quad (1.69)$$

Defining the total scaled lensing potential $\psi = \sum_i \delta\psi_i$, and the total deflection $\vec{\alpha} = \sum_i \delta\vec{\alpha}_i$, we obtain

$$\vec{\alpha}(\vec{\theta}, z_s) = \vec{\nabla}_\theta \psi(\vec{\theta}, z_s) \quad (1.70)$$

The Laplacian of $\delta\psi_i$ with respect to theta is given by

$$\nabla_\theta^2 (\delta\psi_i) = \frac{2}{c^2} \frac{D_{LS} D_L}{D_S} \int_{D_L-\delta D}^{D_L+\delta D} \nabla_\xi^2 \Phi \, dD \quad (1.71)$$

Using (1.62) and (1.63) this becomes

$$\nabla_{\vec{\theta}}^2(\delta\psi_i) = \frac{8\pi G}{c^2} \frac{D_{LS}D_L}{D_S} \Sigma(\vec{\theta}, z_i) \quad (1.72)$$

We now define the critical surface density,

$$\Sigma_c(z) \equiv \frac{c^2 D_S}{4\pi G D_L(z) D_{LS}(z)} \quad (1.73)$$

and the convergence

$$\kappa(\vec{\theta}, z_s) \equiv \sum \frac{\Sigma(\vec{\theta}, z_i)}{\Sigma_c(z_i)} \quad \forall z_i < z_s \quad (1.74)$$

Now summing all the mass-sheets in (1.72) gives the relation between the scaled lensing potential and the convergence

$$\nabla_{\vec{\theta}}^2 \psi(\vec{\theta}, z_s) = 2\kappa(\vec{\theta}, z_s) \quad (1.75)$$

Solving this two-dimensional differential equation gives the effective potential in terms of the convergence:

$$\psi(\vec{\theta}, z) = \frac{1}{\pi} \int_{\mathbb{R}^2} \kappa(\vec{\theta}', z) \ln |\vec{\theta} - \vec{\theta}'| d^2\theta' \quad (1.76)$$

1.7 Weak Gravitational Lensing

The local properties of the mapping in (1.60) are contained in its Jacobian matrix, given by

$$\mathcal{A} \equiv \frac{\partial \vec{\beta}}{\partial \vec{\theta}} = \left(\delta_{ij} - \frac{\partial \alpha_i}{\partial \theta_j} \right) = \left(\delta_{ij} - \frac{\partial^2 \psi}{\partial \theta_i \partial \theta_j} \right), \quad (1.77)$$

where i, j index the two components of the angular position.

Introducing the abbreviation

$$\psi_{ij} = \frac{\partial^2 \psi}{\partial \theta_i \partial \theta_j} \quad (1.78)$$

We can then rewrite the convergence κ (eqn 1.75) and define the complex shear $\gamma \equiv \gamma_1 + i\gamma_2$ of the mapping and write:

$$\begin{aligned} \kappa &= (\psi_{11} + \psi_{22})/2 \\ \gamma_1 &= (\psi_{11} - \psi_{22})/2 \\ \gamma_2 &= \psi_{21} = \psi_{12} \end{aligned} \quad (1.79)$$

The local Jacobian matrix (1.77) of the lens mapping can then be written

$$\mathcal{A} = \begin{pmatrix} 1 - \kappa - \gamma_1 & -\gamma_2 \\ -\gamma_2 & 1 - \kappa + \gamma_1 \end{pmatrix} \quad (1.80)$$

Equations 1.76, 1.78 and 1.79 can be combined and simplified to yield the following relationship between the convergence and the shear, where for simplicity we define the complex angle $\theta \equiv \theta_1 + i\theta_2$:

$$\gamma(\theta) = \frac{-1}{\pi} \int_{\mathbb{R}^2} \mathcal{D}(\theta - \theta') \kappa(\theta') d^2\theta' \quad (1.81)$$

where

$$\mathcal{D}(\theta) = \frac{\theta_1^2 - \theta_2^2 + 2i\theta_1\theta_2}{(\theta_1^2 + \theta_2^2)^2} = \frac{\theta^2}{|\theta|^4} \quad (1.82)$$

is the Kaiser-Squires kernel (Kaiser & Squires, 1993). The lens mapping in eqn. 1.80 describes an image transformation consisting of a magnification with magnitude given by the real convergence κ and a distortion with magnitude and orientation given by the complex shear $\gamma = \gamma_1 + i\gamma_2$. This distortion results in a measurable effect, at least in principle. If the intrinsic shape, size, or brightness of a distant image were known, then the observed shape, size, or brightness could be observed to determine the shear and convergence at that point. Unfortunately, the intrinsic shape and size of a galaxy cannot be known *a priori*, but using well-founded assumptions about the statistics of the *distribution* of shapes and sizes of sources can lead to useful estimates of the shear and/or convergence across the sky.

In the most common approach to weak lensing, the ellipticities of source galaxies are measured, giving a noisy estimate of the *reduced shear*

$$\gamma_r(\theta) = \frac{\gamma(\theta)}{1 - \kappa(\theta)}. \quad (1.83)$$

In the weak limit where $\kappa(\theta) \ll 1$, analyses often assume $\gamma_r(\theta) \approx \gamma(\theta)$, though with higher-precision measurements, this second-order effect can introduce systematic errors in mass maps and power spectra (Dodelson et al., 2006; Shapiro, 2009; Krause & Hirata, 2010). Once the shear field is estimated, the measurements can be utilized in a number of ways to learn about fundamental physical principles; this work will focus on three areas:

Direct mapping: Having measured the shear γ at locations across the sky, the convergence κ can be estimated. κ relates to the projected density via eqn. 1.74. Thus the measured shear can be used to directly estimate a map of the distribution of dark matter in two dimensions. Using redshift information for the lensed sources, there is the potential to extend this mapping to three dimensions. This is the subject of Chapter 3.

Peak statistics: The two dimensional maps recovered as above represent a two-dimensional projection of the three-dimensional distribution of large scale structure, in particular massive galaxy clusters. As discussed in §1.5, both the number of clusters and their mass distribution depend on the details of the geometry, expansion, and makeup of the universe. By computing the statistics of observed lensing peaks to that predicted by theory, it is possible to constrain cosmological parameters using the peaks alone. This is one of the subjects reviewed and explored in Chapter 4.

Power spectrum: The power spectrum of the shear is closely related to the power spectrum of the matter distribution that generates it. By measuring two point information of observed shear, it is possible to constrain cosmological parameters in a way that is complementary to the peak counts mentioned above. This is the subject of Chapter 5.

To enable these three analyses, we will develop a bit further the basic principles of weak lensing mappings and power spectra.

1.7.1 Mapping with Weak Lensing

The tomographic approach to the 3D lensing mapping problem can be computed using the following steps (see, e.g. Hu & Keeton, 2002; Simon et al., 2009; VanderPlas et al., 2011):

1. From the measured ellipticities and redshifts of photometrically observed galaxies, obtain noisy estimates of the shear $\gamma_{obs}(\theta, z)$.
2. Using eqn. 1.81, recover an estimate of $\kappa(\theta, z)$. Note that due to the integral over the lensing kernel $\mathcal{D}(\theta)$, the convergence estimate is non-local: the value of κ at a given

location is related to the value of the γ at *all other* locations.

3. Using eqn. 1.74, determine the projected density $\Sigma(\theta, z)$.
4. As a final step, it is possible in principle to use eqn. 1.62 to recover the 3D mass density $\rho(\theta, z)$. This is the subject of Chapter 3.

To accomplish this, it is convenient to combine steps 3-4 and write the expression for $\kappa(\theta, z)$ in terms of $\rho(\theta, z)$ explicitly. From (1.62) and (1.74), approximating the sum as an integral, we find

$$\kappa(\vec{\theta}, z_s) = 4\pi G \int_0^{z_s} \frac{D^{(A)}(z)[D^{(A)}(z_s) - D^{(A)}(z)]}{D^{(A)}(z_s)} \rho_M(\vec{\theta}, z) \frac{dD^{(A)}(z)}{dz} dz \quad (1.84)$$

The notation has been changed here to make clear that the distances in question are in fact angular diameter distance, the relevant distance in the context of lensing calculations (See §1.3). Recall that angular diameter distance $D^{(A)}$ is related to the comoving distance D by

$$D^{(A)}(z) = a S_\kappa(D) \quad (1.85)$$

where $S_\kappa(D) = D$ for a flat universe. Assuming a flat universe, converting to comoving distances, and writing this in terms of $\varepsilon = \rho c^2$, we find

$$\kappa(\vec{\theta}, z_s) = \frac{4\pi G}{c^2} \int_0^{z_s} dz \frac{dD}{dz} a^2 \frac{D(D_S - D)}{D_S} \varepsilon_M(\vec{\theta}, z), \quad (1.86)$$

where we've used the shorthand $D \equiv D(z)$ and $D_S \equiv D(z_s)$.

To further progress, we can follow §1.5 and write the matter density $\varepsilon_M(\theta, z)$ in equation 1.86 in terms of the density contrast δ :

$$\varepsilon_M(\vec{\theta}, z) = \Omega_M(z) \varepsilon_c(z) [1 + \delta(\vec{\theta}, z)] \quad (1.87)$$

where we have assumed a flat universe, such that the total density is equal to the critical density $\varepsilon_c(z)$ (eqn. 1.23). We'll make use of two further algebraic substitutions: from the definition of comoving distance (eq. 1.28), we can write

$$\frac{dD}{dz} = \frac{c}{H(z)}, \quad (1.88)$$

and from the Friedmann equation (eqn. 1.27) matter density fraction can be written

$$\Omega_M(z) = \frac{H_0^2 \Omega_{M,0} (1+z)^3}{[H(z)]^2}. \quad (1.89)$$

Combining these equations gives

$$\kappa(z_s) = \frac{3cH_0^2 \Omega_{M,0}}{2} \int_0^{z_s} dz \frac{(1+z)}{H(z)} \frac{D(D_S - D)}{D_S} [1 + \delta(z)] \quad (1.90)$$

Because of the mass-sheet degeneracy, $\kappa(z_s)$ can only be determined up to an additive constant across a given redshift bin (see Seitz & Schneider, 1996, for discussion). Assuming the observed field is large enough to average the effects of cosmic variance, the additive constant will be due simply to the background matter distribution. Defining $\bar{\kappa}(z_s)$ to be the convergence due to the background matter distribution in matter-dominated growth, and $\Delta(z) \equiv \delta(z)/a$ we find

$$\kappa(z_s) \equiv \hat{\kappa}(z_s) - \bar{\kappa}(z_s) = \frac{3cH_0^2 \Omega_{M,0}}{2} \int_0^{z_s} dz \frac{1}{H(z)} \frac{D(D_S - D)}{D_S} \Delta(z) \quad (1.91)$$

where, to be explicit,

$$\bar{\kappa}(z_s) = \frac{3cH_0^2 \Omega_{M,0}}{2} \int_0^{z_s} dz \frac{(1+z)}{H(z)} \frac{D(D_S - D)}{D_S} \quad (1.92)$$

To be clear, here, D is the comoving distance to a redshift z , and D_S is the comoving distance to the redshift z_s of the photon source. Equation 1.91 defines the mapping from $\kappa(z_s)$ to $\Delta(z)$ for $z < z_s$.

1.7.2 Power Spectra

Mass mapping can lead to deep astrophysical and cosmological insights through the comparison of dark and luminous matter distributions (e.g. Clowe et al., 2006), through constraints on the mass profiles of collapsed structures (e.g. Oguri et al., 2012), or through the comparison of observed mass peaks to theoretical predictions (see Chapter 4). Because of the noise inherent in lensing observations, most of these localized analyses are limited to very dense regions, far from the linear regime.

The linear regime, as well as the presence of nonlinear effects on small scales, can be measured using power spectra of the weak lensing shear. In order to accomplish this, however, the power spectra of observed shear must be related to the mass power spectra discussed in §1.5.

E and B modes

In this section, we will outline the basic results of Schneider et al. (2002b). We will start by defining the E/B decomposition of the shear field γ . If the shear γ and convergence κ can be expressed as shown in eqn. 1.79, then the gradient of κ can be written

$$\nabla_{\theta}\kappa = \begin{pmatrix} \partial\kappa/\partial\theta_1 \\ \partial\kappa/\partial\theta_2 \end{pmatrix} = \begin{pmatrix} \partial\gamma_1/\partial\theta_1 + \partial\gamma_2/\partial\theta_2 \\ \partial\gamma_2/\partial\theta_1 - \partial\gamma_1/\partial\theta_2 \end{pmatrix} \equiv \mathbf{u}. \quad (1.93)$$

If κ and γ are due entirely to weak lensing, then the vector \mathbf{u} should be a pure gradient field, as will every quantity in the equality in eqn. 1.93. This condition can be compactly expressed by noting that the curl of a gradient is identically zero:

$$\nabla \times \mathbf{u} = 0. \quad (1.94)$$

If, however, other effects are involved (e.g. shot noise, second-order lensing effects, intrinsic alignments, systematic errors, etc.) then \mathbf{u} will not be a pure gradient field and will have a nonzero curl. With this in mind, we will use an analogy from electrodynamics and decompose κ into a curl-free “E-mode” κ_E and a divergence-free “B-mode” κ_B such that

$$\nabla^2\kappa_E = \nabla \cdot \mathbf{u} \quad (1.95)$$

$$\nabla^2\kappa_B = \nabla \times \mathbf{u}. \quad (1.96)$$

We’ll also define the E-mode and B-mode lensing potential following eqn. 1.75:

$$\nabla^2\psi_{E,B} = 2\kappa_{E,B}. \quad (1.97)$$

This allows us to define the E and B modes of γ via eqn. 1.79. Explicitly,

$$\gamma_{E,B} = \left(\frac{1}{2} \left[\frac{\partial^2}{\partial\theta_1\partial\theta_1} - \frac{\partial^2}{\partial\theta_2\partial\theta_2} \right] + i \frac{\partial^2}{\partial\theta_1\partial\theta_2} \right) \psi_{E,B}. \quad (1.98)$$

Combining the convergence E and B modes as a complex linear combination $\kappa = \kappa_E + i\kappa_B$, we find in analogy to eqn. 1.81,

$$[\gamma_E(\theta) + i\gamma_B(\theta)] = \frac{-1}{\pi} \int_{\mathbb{R}^2} \mathcal{D}(\theta - \theta') [\kappa_E(\theta') + i\kappa_B(\theta')] d^2\theta' \quad (1.99)$$

We can define the Fourier transform of the convergence

$$\hat{\kappa}_{E,B}(\ell) = \int d^2\boldsymbol{\theta} e^{i\boldsymbol{\ell}\cdot\boldsymbol{\theta}} \kappa_{E,B}(\boldsymbol{\theta}), \quad (1.100)$$

where ℓ is the angular Fourier variable. We can then define the power spectra (e.g. Schneider et al., 2002b)

$$\langle \hat{\kappa}_{E,B}(\ell) \hat{\kappa}_{E,B}^*(\ell') \rangle = (2\pi)^2 \delta_D(\ell - \ell') P_{E,B}(\ell). \quad (1.101)$$

By the convolution theorem, the Fourier transform of eqn. 1.99 gives

$$\hat{\gamma}_{E,B}(\ell) = \left(\frac{\ell_1^2 - \ell_2^2 + 2i\ell_1\ell_2}{|\ell|^2} \right) \hat{\kappa}_{E,B}(\ell). \quad (1.102)$$

The factor relating $\hat{\gamma}$ and $\hat{\kappa}$ can be expressed as a simple phase $e^{2i\beta}$, so that

$$\langle \hat{\gamma}_{E,B}(\ell) \hat{\gamma}_{E,B}^*(\ell') \rangle = \langle \hat{\kappa}_{E,B}(\ell) \hat{\kappa}_{E,B}^*(\ell') \rangle. \quad (1.103)$$

Based on this equality, we can define the shear correlation function and relate it to the convergence power spectra P_{EB} ,

$$\begin{aligned} \xi_+(\theta) &\equiv \langle \gamma(\mathbf{0}) \gamma^*(\boldsymbol{\theta}) \rangle \\ &= \int_0^\infty \frac{d\ell \ell}{2\pi} J_0(\ell \theta) [P_E(\ell) + P_B(\ell)], \end{aligned} \quad (1.104)$$

where $J_0(x)$ is a Bessel function of the first kind. The “+” distinguishes this correlation measure from two other shear correlations that can be defined, ξ_- and ξ_\times (see Schneider et al., 2002a, for details). We will limit the discussion here to ξ_+ , because this is the relevant measure for our purposes (See discussion in §4.2.4).

The E-mode angular shear power spectrum $P_E(\ell)$ can be expressed as a weighted line-of-sight integral over the matter power spectrum via eqn. 1.90. Taking into account the redshift distribution of galaxies gives (see Takada & Jain, 2004)

$$P_E(\ell) = \int_0^{r_s} dr W^2(r) r^{-2} P_\delta \left(k = \frac{\ell}{r}; z(r) \right) \quad (1.105)$$

Here r is the comoving distance, r_s is the distance to the source, and $W(r)$ is the lensing weight function,

$$W(r) = \frac{3\Omega_{m,0}H_0^2}{2a(r)} \frac{r}{\bar{n}_g} \int_{z(r)}^{z(r_s)} dz n(z) \frac{r(z) - r}{r(z)} \quad (1.106)$$

where $n(z)$ is the empirical redshift distribution of galaxies, with $\bar{n}_g = \int_0^\infty n(z)dz$. This allows us to predict an analytic relation between the 3D mass fluctuation power spectrum $P_\delta(k, z)$ and the correlation function of the shear signal $\xi_+(\ell, z)$. The nonlinear mass fluctuation power spectrum $P_\delta(k, z)$ can be predicted semi-analytically (e.g. Smith et al. (2003)) and has a form dependent on the assumed cosmological model. The shear correlation function $\xi_+(\ell)$ can be computed from observed data. The important point is that this relation provides a direct (if noisy) measure of the distribution of mass: it requires no assumptions about the mass to light ratio or how the non-baryonic matter distribution relates to that of luminous matter. The observations can be related directly to theoretical expectations for the nonlinear power spectrum. For this reason, weak lensing studies provide a powerful probe for constraining the cosmological parameters that describe the geometry and dynamics of the Universe.

In the following sections we undertake a systematic study of gravitational lensing applications enabled by Karhunen-Loève (KL) analysis. We begin in Chapter 2 with a development of the mathematical theory behind KL analysis. In Chapter 3, we explore the use of a KL-based method for reconstruction of three-dimensional mass maps from shear data. In Chapter 4, we explore how KL can be used to address incompleteness in shear surveys, allowing us to interpolate the signal across masked regions. In Chapter 5, we use KL as a basis for computing parameter constraints from two-point statistics of a shear field with incomplete sky coverage.

Chapter 2

INTRODUCTION TO KARHUNEN-LOÈVE ANALYSIS

Karhunen-Loève (KL) analysis is a commonly used statistical tool in a broad range of astronomical applications, from, e.g. studies of correlations in observed properties of galaxy photometry (Efstathiou & Fall, 1984) and galaxy and quasar spectra (Connolly et al., 1995; Connolly & Szalay, 1999; Yip et al., 2004a,b), to analysis of the spatial distribution of galaxies (Vogeley & Szalay, 1996; Matsubara et al., 2000; Szalay et al., 2003; Pope et al., 2004; Tegmark et al., 2006), to characterization of the expected errors in weak lensing surveys (Kilbinger & Munshi, 2006; Munshi & Kilbinger, 2006). In this chapter, we will develop the formalism of KL that will form the basis of the applications in the subsequent chapters.

The KL formalism requires the liberal employment of algebra with vectors, scalars, matrices, and their generalizations. For clarity, we will begin by briefly specifying the notational conventions used in this chapter and throughout this work.

2.1 Notational Conventions

It is important to clearly distinguish between vectors, matrices, and scalars in the following formulation. Vectors will be denoted by bold lower-case symbols; e.g. \mathbf{x} . Matrices will be denoted by bold upper-case symbols; e.g. \mathbf{X} . Scalars will be denoted by non-bold symbols, either upper or lower-case. All vectors are assumed to be column vectors, while a row-vector is indicated by the transpose, \mathbf{x}^T . Single elements of a given vector or matrix are given with subscripts: x_i is the i^{th} element of the vector \mathbf{x} , and X_{ij} is the element in the i^{th} row and j^{th} column of the matrix \mathbf{X} . The vector making up the j^{th} column of \mathbf{X} is indicated by $\mathbf{x}^{(j)}$. Note then, that by this convention, the (i, j) component of matrix \mathbf{X} can be equivalently expressed X_{ij} or $x_i^{(j)}$.

In algebraic expressions, the normal linear algebra rules are assumed. For example, the

expression

$$\mathbf{y} = \mathbf{M}\mathbf{x} + \mathbf{b} \quad (2.1)$$

involves the vectors \mathbf{y} , \mathbf{x} , and \mathbf{b} and the matrix \mathbf{M} . This expression is short-hand for the summation:

$$y_i = \sum_{j=1}^n M_{ij}x_j + b_i \quad (2.2)$$

Using these rules, we can define the magnitude of a vector

$$|\mathbf{x}| \equiv \sqrt{\mathbf{x}^T \mathbf{x}} \quad (2.3)$$

2.2 Basis function decomposition

KL analysis is simply a basis function decomposition, where the basis functions are derived based on the variance and covariance properties of a class of functions. We'll start by describing what is perhaps the best-known basis function decomposition, the Fourier series. We start here because it's a familiar concept that generalizes well to the fundamental ideas of KL analysis.

2.2.1 Fourier Series

The Fourier Series is a means of expressing a bounded function in terms of a certain class of oscillatory basis functions. It is a discrete version of the Fourier Transforms used in cosmological power spectrum analysis, and discussed in §1.7.2.

We'll define a set of oscillatory basis functions

$$\Phi_k(t) = \frac{1}{\sqrt{t_b - t_a}} \exp \left[\frac{2\pi i k(t - t_a)}{t_b - t_a} \right] \quad (2.4)$$

where t is the arbitrary dependent variable, k is the wave-number, and the function is defined in the region $t_a \leq t \leq t_b$. We'll postulate that a function $f(t)$ can be expressed as a linear combination of these basis functions:

$$f(t) = \sum_{k=-\infty}^{\infty} a_k \Phi_k(t). \quad (2.5)$$

Here a_k are an infinite set of complex coefficients. Our claim is that any piecewise continuous and square-integrable function $f(t)$ in the interval $[t_a, t_b]$ can be represented this way. A

rigorous mathematical proof of this statement can be found elsewhere, but below we will lend support to this claim.

Given the claim that Equation 2.5 holds, how can we compute the Fourier coefficients a_k associated with a particular $f(t)$? Though the expression is well-known, we'll briefly derive it here because it illuminates some of the properties of Fourier transforms that will generalize to KL transforms.

To begin, we'll multiply both sides of Equation 2.5 by the complex conjugate $\Phi_{k'}^*(x)$ of the basis function given in Equation 2.4, and integrate both sides over t from t_a to t_b :

$$\int_{t_a}^{t_b} \Phi_{k'}^*(t) f(t) dt = \int_{t_a}^{t_b} \Phi_{k'}^*(t) \sum_{k=-\infty}^{\infty} a_k \Phi_k(x) dt \quad (2.6)$$

On the right-hand side, we can exchange the order of integration and summation to find

$$\int_{t_a}^{t_b} \Phi_{k'}^*(t) f(t) dt = \sum_{k=-\infty}^{\infty} a_k \left[\int_{t_a}^{t_b} \Phi_{k'}^*(t) \Phi_k(x) dt \right]. \quad (2.7)$$

Let's examine the term in the square brackets. Plugging in the definition of the basis functions from Equation 2.4, we have

$$\left[\int_{t_a}^{t_b} \Phi_{k'}^*(t) \Phi_k(x) dt \right] = \left[\frac{1}{t_b - t_a} \int_{t_a}^{t_b} \exp \left(\frac{2\pi i (k - k')(t - t_a)}{t_b - t_a} \right) dt \right] \quad (2.8)$$

This gives two distinct situations for the integral on the right-hand side: when $k = k'$, both the integrand and the term in the brackets is exactly 1. When $k \neq k'$, the integrand oscillates through an integer number of cycles between t_a and t_b (remember that k and k' here are integers), and the result of the integral is exactly 0. So we see that the term in brackets is equal to simply the Kronecker delta function $\delta_{kk'}$, defined as

$$\delta_{ij} = \begin{cases} 1 & \text{if } i = j \\ 0 & \text{if } i \neq j. \end{cases} \quad (2.9)$$

Putting this result into Equation 2.7, only one term of the sum remains and we find

$$a_k = \frac{1}{t_b - t_a} \int_{t_a}^{t_b} \Phi_k^*(t) f(t) dt \quad (2.10)$$

Equation 2.10 shows how to compute the Fourier coefficients a_k for a given $f(t)$. But one might wonder if this is a unique result. Could there be several possible sets of valid Fourier coefficients for a given function?

Let's assume that given a function $f(t)$, there are two valid sets of Fourier coefficients a_k and a'_k that satisfy Equation 2.5. In this case, subtracting the two equations gives

$$f(t) - f(t) = \sum_{k=-\infty}^{\infty} (a_k - a'_k) \Phi_k(t) = 0. \quad (2.11)$$

In a similar manner to above, we can multiply by $\Phi_k^*(t)$, integrate over t from t_a to t_b , and extract a Kronecker delta function to yield

$$\sum_{k=-\infty}^{\infty} (a_k - a'_k) \delta_{kk'} = 0 \quad (2.12)$$

Collapsing the sum, we find that $a_k = a'_k$ for all k . This shows the uniqueness of the Fourier coefficients a_k for a given function $f(t)$ on an interval $[t_a, t_b]$. Thus, given an orthonormal basis Φ_k , there is a single unique linear combination that reconstructs a function $f(t)$ on the defined interval.

2.2.2 Generalizing Orthonormal Bases

Stepping back for a moment, we have shown that for a particular class of basis functions $\Phi_k(t)$, one can find unique coefficients a_k such that one of the expansions of Equation 2.5 holds. A key observation is that all the derivations above rested solely on two special properties of these basis functions:

1. The basis functions are *orthonormal* on the interval $[a, b]$. That is, $\Phi_k(t)$ satisfies

$$\int_{t_a}^{t_b} \Phi_k(t) \Phi_{k'}^*(t) dt = \delta_{kk'} \quad (2.13)$$

2. The basis functions are *complete* on the interval $[t_a, t_b]$. That is, an arbitrary function $f(t)$ can be approximated by

$$f(t) = \sum_{k=1}^N a_k \Phi_k(t) \quad (2.14)$$

and the mean square error satisfies

$$\lim_{N \rightarrow \infty} \int_{t_a}^{t_b} \left[f(t) - \sum_{k=1}^N a_k \Phi_k(t) \right]^2 dt = 0. \quad (2.15)$$

As long as these two properties hold for a class of functions $\Phi_k(t)$, we would be able to repeat the above derivations and express any $f(t)$ via Equation 2.5. This suggests the possible existence of other functions that fit these criteria. Some examples are the Legendre polynomials on the interval $[-1, 1]$, the Laguerre polynomials on the interval $[0, \infty)$, and the Hermite polynomials on the interval $(-\infty, \infty)$. In fact, these different orthonormal basis functions are simply a generalization of well-known geometric bases (such as the x and y axis of a two dimensional vector space) into an abstract function space. Just as there are an infinite number of possible orientations for an (x, y) axis in a two-dimensional vector space, there are an infinite number of possible orthogonal function bases that work in the above formalism. Choosing the right basis can lead to a much easier analysis of a given problem.

2.3 Karhunen-Loève Analysis

Because of the infinite number of possible orthogonal function classes, one might wonder how to choose the optimal class for any particular problem. Karhunen-Loève analysis seeks to answer this question in a very general case.

2.3.1 Derivation of Karhunen-Loève theorem

Imagine now that we have a random process F_t . This can be thought of as an arbitrarily large collection of functions $f^{(i)}(t)$ defined on the interval $t \in [a, b]$. At a given location t , the expectation value of the random process is given by

$$E[F_t] = \lim_{N \rightarrow \infty} \frac{1}{N} \sum_{i=1}^N f^{(i)}(t) \quad (2.16)$$

For simplicity, we'll assume that the random process F_t is *centered*; that is $E[F_t] = 0$. A general random process can be centered by subtracting the expectation value for each t . A centered random process F_t can be characterized by its covariance function, which is defined as

$$\begin{aligned} C_F(t, t') &\equiv E[F_t F_{t'}] \\ &= \lim_{N \rightarrow \infty} \frac{1}{N} \sum_{i=1}^N f^{(i)}(t) f^{(i)}(t'). \end{aligned} \quad (2.17)$$

For an *uncorrelated* random process, $C_F(t, t') = \mathcal{V}_F(t) \delta_{t,t'}$ where $\mathcal{V}_F(t)$ is the *variance* of F_t .

2.3.2 Eigenfunctions

We'll now introduce the *eigenfunctions* $e_k(t)$ of the covariance function $\mathcal{C}_F(t, t')$, which satisfy

$$\int_{t_a}^{t_b} \mathcal{C}_F(t, t') e_k(t') dt' = \lambda_k e_k(t) \quad (2.18)$$

subject to the constraint that $\int_{t_a}^{t_b} |e_k(t)|^2 dt \neq 0$ (i.e. $e_k(t)$ is not everywhere zero). Here λ_k is the *eigenvalue* associated with the eigenfunction $e_k(t)$.

Now what are the properties of these eigenfunctions? First of all, they are orthogonal on the interval $[t_a, t_b]$. We can show this by considering two arbitrary eigenfunctions $e_k(t)$ and $e_{k'}(t)$. Consider the quantity

$$\int_{t_a}^{t_b} dt \int_{t_a}^{t_b} dt' \mathcal{C}_F(t, t') e_{k'}(t') e_k(t) \quad (2.19)$$

Because of the symmetry of the covariance, i.e. $\mathcal{C}_F(t, t') = \mathcal{C}_F(t', t)$, and because the order of integration can be switched, this can be evaluated two different ways, which must be equal:

$$\begin{aligned} \int_{t_a}^{t_b} dt e_k(t) \int_{t_a}^{t_b} dt' \mathcal{C}_F(t, t') e_{k'}(t') &= \int_{t_a}^{t_b} dt' e_{k'}(t') \int_{t_a}^{t_b} dt \mathcal{C}_F(t', t) e_k(t) \\ \int_{t_a}^{t_b} dt \lambda_{k'} e_k(t) e_{k'}(t) &= \int_{t_a}^{t_b} dt' \lambda_k e_k(t') e_{k'}(t') \end{aligned} \quad (2.20)$$

Rearranging the bottom line leads to

$$(\lambda_k - \lambda_{k'}) \int_{t_a}^{t_b} dt e_k(t) e_{k'}(t) = 0 \quad (2.21)$$

So for $\lambda_k \neq \lambda_{k'}$, then e_k and $e_{k'}$ must be orthogonal¹. From the definition in Equation 2.18, we see that if $e_k(t)$ is an eigenfunction with eigenvalue λ_k , then for any arbitrary constant K , $K e_k(t)$ is an eigenfunction with eigenvalue λ_k as well. To make the choice of eigenfunction more definite, we will assume all eigenfunctions are normalized: that is

$$\int_{t_a}^{t_b} dt e_k(t) e_{k'}(t) = \delta_{kk'} \quad (2.22)$$

¹In the degenerate case when $\lambda_k = \lambda_{k'}$, one can still construct orthogonal vectors by linear combinations:

$$\begin{aligned} e_+(t) &= \frac{e_k(t) + e_{k'}(t)}{\sqrt{2}} \\ e_-(t) &= \frac{e_k(t) - e_{k'}(t)}{\sqrt{2}}. \end{aligned}$$

This leads to two new orthogonal eigenfunctions e_+ and e_- with the same eigenvalue λ_k .

for all k . This still allows any eigenfunction to have an arbitrary phase: that is, an eigenfunction may be multiplied by $e^{i\theta}$ for any θ , and still satisfy our orthogonality condition. This fact will become important later.

The net result is that the eigenfunctions $e_k(t)$ form an orthonormal basis for the space of functions represented by the random process F_t . In general, the eigenfunctions also satisfy the completeness relation (see eqn. 2.15). The proof of the completeness of eigenfunctions for a symmetric kernel $\mathcal{C}_F(t, t')$ is rather involved, and can be found in, e.g. Courant & Hilbert (1989).

Let's now consider the expansion of the random process F_t onto the eigenvectors $e_k(t)$. Analogously to the Fourier case discussed above, we have

$$F_t = \sum_{k=1}^{\infty} A_k e_k(t). \quad (2.23)$$

where here A_k can be thought of as a set of coefficients $a_k^{(i)}$ in the same way that the random process F_t can be thought of as a set of functions $f^{(i)}(t)$. Multiplying both sides by $e_{k'}(t)$, integrating, and using the orthogonality of eigenvectors (this is analogous to the derivation in Equations 2.7-2.10) leads to

$$A_k = \int_{t_a}^{t_b} F_t e_k(t) dt \quad (2.24)$$

Because of the fact that the random process is centered (i.e. $E[F_t] = 0$), it is straightforward to show that $E[A_k] = 0$ as well. The more interesting computation is that of the covariance of the eigenvectors, $\mathcal{C}_A(k, k')$. From Equations 2.17 and 2.24, we have

$$\begin{aligned} \mathcal{C}_A(k, k') &= E[A_k A_{k'}] \\ &= E \left[\int_{t_a}^{t_b} dt \int_{t_a}^{t_b} dt' F_t e_k(t) F_{t'} e_{k'}(t') \right] \\ &= \int_{t_a}^{t_b} dt \int_{t_a}^{t_b} dt' E[F_t F_{t'}] e_{k'}(t') e_k(t) \\ &= \int_{t_a}^{t_b} dt \int_{t_a}^{t_b} dt' \mathcal{C}_F(t, t') e_{k'}(t') e_k(t) \end{aligned}$$

Substituting Equation 2.18, we find that this gives

$$\begin{aligned} \mathcal{C}_A(k, k') &= \int_{t_a}^{t_b} dt \lambda_{k'} e_{k'}(t) e_k(t) \\ &= \lambda_k \delta_{kk'} \end{aligned} \quad (2.25)$$

So we see that projection of the centered random process \tilde{F}_t onto the eigenvectors of its covariance matrix yields coefficients which are uncorrelated, with variance equal to the eigenvalues λ_k . This result is the Karhunen-Loève theorem, and it has many ramifications that will be discussed below.

2.3.3 Partial Reconstructions

We have shown that Karhunen-Loève provides an orthonormal basis for a random field with uncorrelated projection coefficients. We can go further and show that Karhunen-Loève provides the optimal orthonormal basis for low-rank approximations of functions in a random field.

Above, we expressed the completeness relation for a single function $f(t)$ (eqn. 2.15). For a random process, an orthonormal basis $\phi_k(t)$ is complete if and only if there exists a random process B_k such that

$$\lim_{N \rightarrow \infty} \int_{t_a}^{t_b} \left[F_t - \sum_{k=1}^N B_k \phi_k(t) \right]^2 dt = 0. \quad (2.26)$$

A random process is *low-rank* if and only if there exists a complete orthonormal basis $\phi_k(t)$ such that $E[B_k^2] = 0$ for one or more values of k . In other words, a random process is low-rank if for some basis $\phi_k(t)$, some values of k are not required for a perfect reconstruction of the function.

Let us consider an arbitrary complete orthonormal basis $\phi_k(t)$, with $F_t = \sum_{k=1}^{\infty} B_k \phi_k(t)$. Given this basis, we'll define the low-rank approximation of F_t

$$F_t^{(N)} = \sum_{k=1}^N B_k \phi_k(t) \quad (2.27)$$

We'll seek to minimize the expectation value of the squared error

$$\begin{aligned} \mathcal{E}_N^2 &= \int_{t_a}^{t_b} \left[F_t - F_t^{(N)} \right]^2 dt \\ &= \int_{t_a}^{t_b} \left[\sum_{k=N+1}^{\infty} B_k \phi_k(t) \right]^2 dt. \end{aligned} \quad (2.28)$$

Expanding the sum leads to

$$\begin{aligned}
\mathcal{E}_N^2 &= \sum_{k=N+1}^{\infty} \sum_{k'=N+1}^{\infty} \int_{t_a}^{t_b} [B_k B_{k'} \phi_k(t) \phi_{k'}(t)] dt \\
&= \sum_{k=N+1}^{\infty} \sum_{k'=N+1}^{\infty} B_k B_{k'} \delta_{kk'} \\
&= \sum_{k=N+1}^{\infty} B_k^2
\end{aligned} \tag{2.29}$$

Taking the expectation value and plugging in the equivalent of Equation 2.24 for B_k , we find

$$\begin{aligned}
E[\mathcal{E}_N^2] &= E \left[\sum_{k=N+1}^{\infty} \int_{t_a}^{t_b} dt \int_{t_a}^{t_b} dt' F_t F_{t'} \phi_m(t) \phi_m(t') \right] \\
&= \sum_{k=N+1}^{\infty} \int_{t_a}^{t_b} dt \int_{t_a}^{t_b} dt' C_F(t, t') \phi_m(t) \phi_m(t')
\end{aligned} \tag{2.30}$$

We'd like to minimize this expected error over the basis $\phi_m(t)$, subject to the constraint that $\phi_m(t)$ are an orthonormal basis. We'll accomplish this by the method of Lagrange multipliers. Our Lagrangian is

$$\mathcal{L}(\{\phi(t)\}) = \sum_{k=N+1}^{\infty} \left[\int_{t_a}^{t_b} dt \int_{t_a}^{t_b} dt' C_F(t, t') \phi_m(t) \phi_m(t') - \lambda_k \left(1 - \int_{t_a}^{t_b} \phi_m(t)^2 dt \right) \right] \tag{2.31}$$

Minimizing this with respect to ϕ_k gives

$$\frac{\partial \mathcal{L}}{\partial \phi_k(t)} = \int_{t_a}^{t_b} dt' C_F(t, t') \phi_k(t') - \lambda_k \phi_k(t). \tag{2.32}$$

The optimum for each k is where this derivative equals zero; setting to zero and solving recovers the original eigenvalue problem (Eq. 2.18) from which we derived the KL basis $\{e_k(t)\}$. By the uniqueness of the eigenvalue decomposition, this shows that the KL basis is the optimal basis for low-rank approximations of functions drawn from F_t . Furthermore, for an approximation using N eigenvectors, the mean squared error is given by

$$\begin{aligned}
E[\mathcal{E}_N^2] &= \sum_{k=N+1}^{\infty} E[A_k^2] \\
&= \sum_{k=N+1}^{\infty} \lambda_k
\end{aligned} \tag{2.33}$$

This is an interesting result: it says that in order to minimize the expectation value of the reconstruction error \mathcal{E}_N for all N , we simply need to order the eigenvalues such that $\lambda_k \geq \lambda_{k+1}$ for all eigenvalue-eigenfunction pairs $(\lambda_k, e_k(t))$.

Because of this, throughout this work we will follow this convention when ordering the eigenvalues in a KL decomposition.

2.3.4 KL in the presence of noise

In practice, the observed random field F_t is composed of the sum of a signal S_t and noise N_t . We'll continue to assume that both of these are centered. The covariance matrix then becomes

$$\mathcal{C}_F(t, t') = E[(S_t + N_t)(S_{t'} + N_{t'})] \quad (2.34)$$

Under the assumption that the signal S_t and noise N_t are uncorrelated, this can be simplified to

$$\begin{aligned} \mathcal{C}_F(t, t') &= E[S_t S_{t'}] + E[N_t N_{t'}] \\ &= \mathcal{C}_S(t, t') + \mathcal{C}_N(t, t') \end{aligned} \quad (2.35)$$

The Karhunen-Loève eigenfunctions always diagonalize the full covariance $\mathcal{C}_F(t, t')$. In the case of uncorrelated “white” noise, $\mathcal{C}_N(t, t') = \sigma^2 \delta(t - t')$ and both the signal and the noise become diagonalized. In this case, the noise per mode is a constant σ^2 , and the ranking of the eigenfunctions leads to modes which are ranked in signal-to-noise. This is why KL modes are often referred to as “signal-to-noise eigenmodes” (Vogele & Szalay, 1996).

In cases when the noise is not white, we can still recover signal-to-noise information by preprocessing with a whitening transformation. The eigenvectors $n_k(t)$ of the noise covariance, which satisfy

$$\int_{t_a}^{t_b} \mathcal{C}_N(t, t') n_k(t') dt' = \sigma_k n_k(t) \quad (2.36)$$

can be used to apply a whitening transform to both the signal and the noise. The whitened covariance is given by

$$\begin{aligned} \mathcal{C}_F^{(W)}(k, k') &\equiv \int_{t_a}^{t_b} dt \int_{t_a}^{t_b} dt' \mathcal{C}_F(t, t') \frac{n_k(t) n_{k'}(t')}{\sigma_k \sigma_{k'}} \\ &= \mathcal{C}_S^{(W)}(k, k') + \delta_{kk'}. \end{aligned} \quad (2.37)$$

The signal is now expressed in the basis of the noise eigenmodes $n_k(t)$, and the noise has been made white with unit variance. The KL modes derived from the whitened covariance $\mathcal{C}_F^{(W)}(k, k')$ will have eigenvalues that represent the signal-to-noise in each mode.

2.3.5 Karhunen-Loève: theory to practice

The abstract formalism presented above is interesting in itself, but one might wonder what practical advantages can be gained from this discussion. In practice, we don't deal with an abstract stochastic process F_t , but with discrete, measured data. For this reason, the continuous formalism from above can be transformed into a discrete linear algebraic formalism, as seen below. In this section we will discuss the practical computational aspects of KL analysis.

Imagine, for the moment, that an astronomer has observed the spectra of N galaxies. After normalization and correction for redshift effects, the spectra can be encoded as a series of N real-valued functions $f^{(i)}(\lambda)$ over some defined domain $\lambda \in [a, b]$. In practice, we measure these spectra at a finite set of wavelengths $\boldsymbol{\lambda}^T = [\lambda_1, \lambda_2 \dots \lambda_M]$ so that our observations $\mathbf{f}^{(i)}$ become M -dimensional vectors. For convenience, we'll store these spectra in a $N \times M$ matrix $\mathbf{F} = [\mathbf{f}^{(1)}, \mathbf{f}^{(2)} \dots \mathbf{f}^{(N)}]^T$, where each row of the matrix represents one spectrum. These series of spectra \mathbf{F} can be considered a finite realization of a particular random process F_λ .

The expectation value $E[F_\lambda]$ can be approximated via the sample mean:

$$E[F_\lambda] \approx \bar{\mathbf{f}} = \frac{1}{N} \sum_{i=1}^N \mathbf{f}^{(i)} \quad (2.38)$$

and the covariance function can be approximated by the covariance matrix

$$E[F_\lambda F_{\lambda'}] \approx \mathbf{C}_F = \frac{1}{N-1} \tilde{\mathbf{F}}^T \tilde{\mathbf{F}} \quad (2.39)$$

where we have defined the centered matrix

$$\tilde{\mathbf{F}} \equiv \mathbf{F} - \mathbf{1}_N \bar{\mathbf{f}}^T. \quad (2.40)$$

and $\mathbf{1}_N$ is the length- N vector of ones. The $N-1$ in the denominator of Equation 2.39 is called the *Bessel Correction*, and results from the reduced number of degrees of freedom after the mean is subtracted.

We can approximate the eigenfunctions $e^{(i)}(\lambda)$ and eigenvalues λ_i via the diagonalization of \mathcal{C}_F , computed using standard linear algebra techniques. The diagonalization of the covariance matrix is

$$\mathcal{C}_F = \mathbf{V} \mathbf{\Lambda} \mathbf{V}^T, \quad (2.41)$$

where the columns of the matrix \mathbf{V} are the eigenvectors (such that $\mathbf{V}^T \mathbf{V} = \mathbf{I}$, the identity matrix), and $\mathbf{\Lambda}$ is the diagonal matrix of eigenvalues, such that $\Lambda_{ij} = \lambda_i \delta_{ij}$. In practice, the eigenvalues and eigenvectors can often be computed more efficiently via a singular value decomposition:

$$\mathbf{U} \mathbf{\Sigma} \mathbf{V}^T = \frac{1}{\sqrt{N-1}} \tilde{\mathbf{F}} \quad (2.42)$$

where the orthogonal matrices \mathbf{U} and \mathbf{V} are called the left and right singular vectors, respectively, and $\mathbf{\Sigma}$ is a diagonal matrix of singular values. One can quickly show from Equations 2.39 and 2.42 that

$$\begin{aligned} \mathcal{C}_F &= \mathbf{V} \mathbf{\Sigma} \mathbf{U}^T \mathbf{U} \mathbf{\Sigma} \mathbf{V}^T \\ &= \mathbf{V} \mathbf{\Sigma}^2 \mathbf{V}^T. \end{aligned} \quad (2.43)$$

Comparing to Equation 2.41, we see that $\mathbf{\Lambda} = \mathbf{\Sigma}^2$, and the eigenvectors \mathbf{V} are identical to the right singular vectors of Equation 2.42, up to an arbitrary ordering of columns. Ordering our eigenvalues according to the rule in §2.3.3 takes care of this uncertainty.

The columns of \mathbf{V} are the *eigenvectors*, and are the discrete representation of the eigenfunctions $e^{(i)}(\lambda)$. These eigenvectors satisfy all the properties of the KL bases discussed above: they diagonalize the sample correlation matrix, they provide the best possible low-rank linear approximation to any spectrum from the sample, and in the presence of uncorrelated noise, they allow an orthogonal decomposition onto a basis with a natural ranking in signal-to-noise.

In the case of the spectrum example, we have no theoretical expectation for the correlation matrix $\mathcal{C}(\lambda, \lambda')$, so we are forced to approximate the matrix based on the sample correlation using Equation 2.39. If we had sufficient physical understanding of every process at work in each galaxy, it might be possible to compute that correlation matrix from theory alone. The number of variables involved, however, make this prospect near impossible.

There are other situations in astronomical measurement, however, when a theoretical expectation of the correlation matrix is possible in practice. We will see in the following sections how the correlation matrix of particular cosmological observations can be approximated from theory alone.

2.3.6 KL with missing data

Along with discrete data samples, another challenge when applying KL to real data is the presence of missing data: given a KL basis, how can one derive the projected coefficients when data are missing? Note that in this section we'll assume that the KL basis has been obtained independently. It is also possible to derive a KL eigenbasis from incomplete data using an iterative approach: see, e.g. Connolly & Szalay (1999); Yip et al. (2004a).

To begin, we'll assume that we have an observed object represented by the K -dimensional vector $\mathbf{x} = [x_1, x_2 \cdots x_K]^T$ and a set of normalized KL basis functions $\mathbf{V} = [\mathbf{v}_1, \mathbf{v}_2 \cdots \mathbf{v}_K]$ arranged in order of decreasing eigenvalue λ_i . We have shown above that the best rank- N linear approximation of \mathbf{x} is given by

$$\mathbf{x}^{(N)} = \sum_{i=1}^N a_i \mathbf{v}_i. \quad (2.44)$$

where the coefficients can be calculated as

$$a_i = \mathbf{v}_i^T \mathbf{x}. \quad (2.45)$$

When \mathbf{x} has missing data, however, the question of how to compute a_i is not as straightforward. Simply setting the missing values to zero will not work: the reconstruction will then faithfully recover those zero values. We desire instead to constrain the expected contribution of each eigenvector to \mathbf{x} while *ignoring* the contribution of the missing data.

A simple solution may be to simply truncate the vectors such that the dot product is only computed over unmasked values. It is easy to see that this is identical to the “set to zero” solution just discussed. Furthermore, there is the problem that in general, a set of bases truncated in this way does not retain its orthogonality.

Another approach may be to derive a new basis which *is* orthogonal over the truncated space. This is similar in spirit to the method explored by Gorski (1994) in analysis of CMB

data. While this leads to a complete orthogonal basis for the observed portion of the field, coefficients of these new modes have no simple relationship to coefficients of modes covering the full field. In general, a rank-deficient transformation matrix must be inverted in order to convert between the two.

We'll use a different approach. We have shown above that when noise is not present, the KL vectors define the optimal basis for rank- N reconstruction in the least-squares sense. That is, for an arbitrary truncated orthonormal basis $\mathbf{\Phi}_{(N)}$, (where truncated means we use only the first N columns of $\mathbf{\Phi}$, with $0 < N \leq K$),

$$\chi^2 = \left| \left(\mathbf{x} - \mathbf{\Phi}_{(N)}^T \mathbf{a}^{(N)} \right) \right|^2 \quad (2.46)$$

is minimized on average when $\mathbf{\Phi} = \mathbf{V}_{(N)} = [\mathbf{v}_1, \mathbf{v}_2 \cdots \mathbf{v}_N]$, $N \leq K$. Here we flip the problem: we know the desired basis $\mathbf{V}_{(N)}$, and hope to find the optimal vector of coefficients $\mathbf{a}^{(N)}$ which minimizes the χ^2 in the presence of the missing data (Connolly & Szalay, 1999). We'll define a diagonal weight matrix \mathbf{W} such that $W_{ij} = w_i \delta_{ij}$, where $w_i = 1$ where x_i is defined, and $w_i = 0$ where x_i is missing. Our expression to minimize then becomes

$$\chi^2(\mathbf{a}^{(N)}) = \left(\mathbf{x} - \sum_{i=1}^N a_i^{(N)} \mathbf{v}^{(i)} \right)^T \mathbf{W}^2 \left(\mathbf{x} - \sum_{i=1}^N a_{(N),i} \mathbf{v}^{(i)} \right). \quad (2.47)$$

To minimize this with respect to the coefficients $a_{(N),i}$, we differentiate and find

$$\frac{\partial \chi^2}{\partial a_{(N),i}} = -2\mathbf{x}^T \mathbf{W}^2 \mathbf{v}^{(i)} + 2 \sum_{j=1}^N a_{(N),j} \mathbf{v}^{(j)T} \mathbf{W}^2 \mathbf{v}^{(i)}. \quad (2.48)$$

Setting the derivative to zero and combining terms gives

$$\mathbf{x}^T \mathbf{W}^2 \mathbf{v}^{(i)} = \sum_{j=1}^N a_j^{(N)} \mathbf{v}^{(j)T} \mathbf{W}^2 \mathbf{v}^{(i)}. \quad (2.49)$$

If there are no areas of missing data, then $\mathbf{W} = \mathbf{I}$ and we simply recover $a_i = \mathbf{v}_i^T \mathbf{x}$, our standard expression for finding the KL coefficients with no missing data. In the general case, however, because the inner-product of $\mathbf{v}^{(i)}$ and $\mathbf{v}^{(j)}$ is modulated by \mathbf{W} , there is no delta function to collapse the sum.

We can simplify this notation by defining the correlation matrix of the mask \mathbf{M}_N , such that

$$[\mathbf{M}_N]_{ij} \equiv \mathbf{v}^{(j)T} \mathbf{W}^2 \mathbf{v}^{(i)} \quad (2.50)$$

so that eq. 2.49 can be compactly written

$$\mathbf{x}^T \mathbf{W}^2 \mathbf{V}_{(N)} = \mathbf{a}^{(N)T} \mathbf{M}_N. \quad (2.51)$$

From this, we can quickly see that the optimal set of coefficients $\mathbf{a}^{(N)}$ is given by

$$\mathbf{a}^{(N)} = [\mathbf{M}_N]^{-1} \mathbf{V}_{(N)}^T \mathbf{W}^2 \mathbf{x}. \quad (2.52)$$

This can be viewed as a generalized form of the expression in eq. 2.45: if \mathbf{W} is set equal to the identity matrix (indicating no missing data), then \mathbf{M}_N is also the identity and we recover eq. 2.45 exactly.

If some of the diagonal entries in \mathbf{W} are zero, then the correlation matrix \mathbf{M}_K for the full set of K eigenvectors is rank-deficient and cannot be inverted as required for eq. 2.52. For this reason, it is essential to use the truncated eigenvectors $\mathbf{V}_{(N)}$, with $N \leq \text{rank}(\mathbf{W})$. It is not strictly necessary to discard the eigenvectors corresponding to the smallest eigenvalues, but this choice leads to the highest signal-to-noise result. For the simple binary masking case where \mathbf{W} is a diagonal matrix consisting of zeros and ones, the rank of \mathbf{W} is equivalent to its trace, or the sum of nonzero diagonal terms.

Once these approximate KL coefficients $\mathbf{a}^{(N)}$ are determined, it is straightforward to use these to approximate the unmasked vector \mathbf{x} :

$$\mathbf{x} \approx \sum_{i=0}^N a_i^{(N)} \mathbf{v}^{(i)}. \quad (2.53)$$

Here we have used the coefficients determined from the unmasked region of the data to constrain the unobserved value in the masked regions.

This could be further generalized by allowing \mathbf{W} to be an arbitrary matrix, for instance encoding the inverse of the noise covariance associated with the observed vector \mathbf{x} . In unconstrained regions, the noise is infinite and the inverse is zero. This leads to very similar results to those expressed here (in this case, \mathbf{W}^2 is replaced by $\mathbf{W}^T \mathbf{W}$). This is equivalent to the whitening operation discussed in §2.3.4. We will not use this formalism here, so we leave it only as a suggested extension.

2.4 Karhunen-Loève Analysis and Bayesian Inference

Because of the signal-to-noise optimality properties of KL, it can be very useful within Bayesian parameter estimation. Given observations D and prior information I , Bayes' theorem specifies the posterior probability of a model described by the parameters $\{\theta_i\}$:

$$P(\{\theta_i\}|DI) = P(\{\theta_i\}|I) \frac{P(D|\{\theta_i\}I)}{P(D|I)} \quad (2.54)$$

The term on the left hand side is the *posterior* probability of the set of model parameters $\{\theta_i\}$, which is the quantity we are interested in.

The first term on the right side of the equation is the *prior*. It quantifies how our prior information I affects the probabilities of the model parameters. The prior is where information from other surveys (e.g. WMAP, etc) can be included. The likelihood function for the observed coefficients \mathbf{a} enters into the numerator $P(D|\{\theta_i\}I)$. The denominator $P(D|I)$ is essentially a normalization constant, set so that the sum of probabilities over the parameter space equals unity.

KL is useful in the case where the model $\{\theta\}$ can be expressed in terms of a covariance $\mathbf{C}_{\{\theta\}}$ (see Vogeley & Szalay, 1996). Given a data vector \mathbf{d} with observed noise covariance \mathcal{N} , the KL vectors are the eigenvectors $\mathbf{V}_{\{\theta\}}$ of the whitened total covariance

$$\mathbf{C}_{\{\theta\},W} = \mathcal{N}^{-1/2} \mathbf{C}_{\{\theta\}} \mathcal{N}^{-1/2}. \quad (2.55)$$

These eigenvectors can be used to quickly compute the KL coefficients of the observed data,

$$\mathbf{a}_{\{\theta\}} = \mathbf{V}_{\{\theta\}}^\dagger \mathcal{N}^{-1/2} \mathbf{d}. \quad (2.56)$$

For a given model $\{\theta_i\}$, we can predict the expected distribution of coefficients $\mathbf{a}_{\{\theta_i\}}$:

$$\begin{aligned} \mathbf{X}_{\{\theta_i\}} &\equiv \langle \mathbf{a}_{\{\theta_i\}} \mathbf{a}_{\{\theta_i\}}^\dagger \rangle \\ &= \mathbf{V}_{\{\theta\}}^\dagger \mathcal{N}^{-1/2} \mathbf{C}_{\{\theta_i\}} \mathcal{N}^{-1/2} \mathbf{V}_{\{\theta\}} + \mathbf{I}. \end{aligned} \quad (2.57)$$

If the length of the data vector \mathbf{d} is N , then the full analysis results in $\mathbf{X}_{\{\theta_i\}}$ being an $N \times N$ matrix. Alternatively, one can truncate the eigenvectors to $n < N$ terms: this leads to $\mathbf{X}_{\{\theta_i\}}$ being an $n \times n$ matrix, and is equivalent to working with an optimal low-rank

approximation of the data \mathbf{d} . Using this, the measure of departure from the model $\{\theta\}$ is given by the quadratic form

$$\chi_{\{\theta\}}^2 = \mathbf{a}^\dagger \mathbf{X}_{\{\theta_i\}}^{-1} \mathbf{a} \quad (2.58)$$

The likelihood is then given by

$$P(D|\{\theta\}I) = \mathcal{L}(\mathbf{a}|\{\theta_i\}) = (2\pi)^{n/2} |\det(X_{\{\theta_i\}})|^{-1/2} \exp(-\chi_{\{\theta\}}^2/2) \quad (2.59)$$

where n is the number of degrees of freedom: in most cases, $n = N$, the number of eigenmodes included in the analysis. The likelihood given by Equation 2.59 enters into Equation 2.54 when computing the posterior probability. This sort of approach will be applied to observed shear in Chapter 5.

2.5 Karhunen-Loève Analysis of Shear

In the case of shear observations, the observed vector $\boldsymbol{\gamma}$ consists of the N ellipticity observations within the series of window functions $A_i(\boldsymbol{\theta}, z)$, with $i = 1 \dots N$. In general, these window functions can overlap, though in most cases this would lead to correlated noise which makes the analysis more difficult. The expected correlation matrix of the observed shear $\boldsymbol{\gamma}$ is given by

$$[\mathcal{C}_\gamma]_{ij} = \int d^2\theta A_i(\boldsymbol{\theta}, z) \int d^2\theta' A_j(\boldsymbol{\theta}', z) \xi_+(|\boldsymbol{\theta} - \boldsymbol{\theta}'|) + \mathcal{N}_{ij}. \quad (2.60)$$

where the matrix \mathcal{N}_{ij} is the noise covariance between bins. The shear correlation function ξ_+ can be computed from the theoretical 3D mass power spectrum, using the results from the previous chapter (eqs. 1.104-1.106).

The noise matrix \mathcal{N} can be estimated from the measurement process: in the simplest case where noise is due to shot-noise only and the windows A_i are non-overlapping, $\mathcal{N} \propto \sigma_i^2 \mathbf{I}$ where $\sigma_i = \sigma_{int}/\sqrt{N_i}$ is the shot noise, given the intrinsic ellipticity σ_{int} and the number of galaxies N_i in the bin described by A_i .

Once the theoretical correlation matrix is computed, the KL basis can be determined using linear algebraic methods, and the basis functions can be employed in any of the variety of ways suggested above. In this work, we will explore three applications of this procedure. In Chapter 3, we will use the properties of the theoretical covariance as a basis for a filter

for constructing 3D mass maps from weak lensing shear observations. In Chapter 4, the KL modes will be used to correct for masking in a realistic shear map, and the resulting maps will be analyzed using shear peak statistics. In Chapter 5, the KL modes will be used for cosmological parameter estimation using shear catalogs from the COSMOS weak lensing survey. In all three cases, the ability to theoretically compute the covariance matrix of the observations leads to an analysis optimally tuned to the noise properties of the observed signal.

Chapter 3

3D WEAK LENSING MAPS WITH KL

The material in this chapter is adapted from VanderPlas et al. (2011). In it, we present a new method for constructing three-dimensional mass maps from gravitational lensing shear data. We solve the lensing inversion problem using truncation of singular values (within the context of generalized least squares estimation) without a priori assumptions about the statistical nature of the signal. This singular value framework allows a quantitative comparison between different filtering methods: we evaluate our method beside the previously explored Wiener filter approaches. Our method yields near-optimal angular resolution of the lensing reconstruction and allows cluster sized halos to be de-blended robustly. It allows for mass reconstructions which are 2-3 orders-of-magnitude faster than the Wiener filter approach; in particular, we estimate that an all-sky reconstruction with arcminute resolution could be performed on a time-scale of hours on a current workstation. We find however that linear, non-parametric reconstructions have a fundamental limitation in the resolution achieved in the redshift direction.

This chapter was originally published in collaboration with Andrew Connolly, Bhuvnesh Jain, and Mike Jarvis in the February 2011 edition of the *Astronomical Journal* (VanderPlas et al., 2011, ApJ, Vol. 727, p. 118; © 2011 by the American Astronomical Society) and is reproduced below with permission of the American Astronomical Society.

3.1 Introduction

Taylor (2001), Hu & Keeton (2002, hereafter HK02) and Bacon & Taylor (2003) first looked at non-parametric 3D mapping of a gravitational potential. HK02 presented a linear-algebraic method for *tomographic mapping* of the matter distribution – splitting the sources and lenses into discrete planes in redshift. They found that the inversion along each line-of-sight is ill-conditioned, and requires regularization through *Wiener filtering*. Wiener filtering

reduces reconstruction noise by using the expected statistical properties of the signal as a prior: for the present problem, this prior is the nonlinear mass power spectrum. Simon et al. (2009, hereafter STH09) made important advances to this method by constructing an efficient framework in which the inversions for every line-of-sight are computed simultaneously, allowing for greater flexibility in the type of filter used. They introduced two types of Wiener filters: a “radial Wiener filter”, based on the HK02 method, and a “transverse Wiener filter”, based on the Limber approximation to the 3D mass power spectrum. They showed that the use of a generalized form of either filter leads to a biased result – the filtered reconstruction of the line-of-sight matter distribution for a localized lensing mass is both shifted and spread-out in redshift.

One issue with the Wiener filter approach is the assumption of Gaussian statistics in the reconstructed signal. In reality, the matter distribution at relevant scales can be highly non-Gaussian. It is possible that the redshift bias found in STH09 is not inherent to nonparametric linear mapping, but rather a result of this deficiency in the Wiener filtering method.

In this chapter, we develop an alternate noise-suppression scheme for tomographic mapping that, unlike Wiener filtering, has no dependence on assumptions about the signal. Our goal is to explore improvements in the reconstruction and examine, in particular, the recovery of redshift information using the different methods. We begin in Section 3.2 by discussing the tomographic weak-lensing model developed by HK02 and STH09 and presenting our estimator for the density parameter, δ . In Sections 3.3 and 3.4 we implement this method for a simple case, and compare the results with those of the STH09 transverse and radial Wiener filters.

3.2 Method

For tomographic weak lensing, we are concerned with three quantities: the complex-valued shear $\gamma(\vec{\theta}, z)$, the real-valued convergence $\kappa(\vec{\theta}, z)$, and the dimensionless density parameter $\delta(\vec{\theta}, z)$. As discussed in §1.7, the relationship between γ and κ is given by a convolution over all angles $\vec{\theta}$, and the density δ is related to κ by a line-of-sight integral over the lensing efficiency function, $W(z, z_s)$. The key observation is that in the weak lensing regime, each

of these operations is linear: if the variables are discretized, they become systems of linear equations, which can in principle be solved using standard matrix methods.

3.2.1 Linear Mapping

Details of the weak lensing formalism are covered in §1.7.1. Here we'll briefly review the most relevant pieces. To compute 3D mass maps with weak lensing, we begin by creating a common pixel binning of the observed field of N_x by N_y equally sized square pixels of angular width $\Delta\theta_x = \Delta\theta_y$. Within each of the $N_x N_y \equiv N_{xy}$ individual lines of sight, we bin γ into N_s source-planes, and bin δ into N_l lens-planes, $N_l \leq N_s$. Thus we have two 1D data vectors, which are concatenations of the line-of-sight vectors within each pixel: $\boldsymbol{\gamma}$, of length $N_{xy}N_s$; and $\boldsymbol{\delta}$, of length $N_{xy}N_l$. (Note that throughout this section, boldface denotes a vector quantity.) As a result of this binning, we can write the discretized lensing equations in a particularly simple form:

$$\boldsymbol{\gamma} = M_{\gamma\delta}\boldsymbol{\delta} + \mathbf{n}_{\gamma} \quad (3.1)$$

where $\boldsymbol{\gamma}$ is the vector of binned shear observations with noise given by \mathbf{n}_{γ} , and $\boldsymbol{\delta}$ is the vector of binned density parameter. For details on the form of the matrix $M_{\gamma\delta}$, refer to Appendix B.

The linear estimator $\hat{\boldsymbol{\delta}}$ of the signal is found by minimizing the quantity

$$\chi^2 = (\boldsymbol{\gamma} - M_{\gamma\delta}\boldsymbol{\delta})^\dagger \mathcal{N}_{\gamma\gamma}^{-1} (\boldsymbol{\gamma} - M_{\gamma\delta}\boldsymbol{\delta}) \quad (3.2)$$

where \dagger indicates the conjugate transpose, and $\mathcal{N}_{\gamma\gamma} \equiv \langle \mathbf{n}_{\gamma} \mathbf{n}_{\gamma}^\dagger \rangle$ is the noise covariance of the measurement $\boldsymbol{\gamma}$, and we assume $\langle \mathbf{n}_{\gamma} \rangle = 0$. The best linear unbiased estimator for this case is due to Aitken (1934):

$$\hat{\boldsymbol{\delta}}_A \equiv \left[M_{\gamma\delta}^\dagger \mathcal{N}_{\gamma\gamma}^{-1} M_{\gamma\delta} \right]^{-1} M_{\gamma\delta}^\dagger \mathcal{N}_{\gamma\gamma}^{-1} \boldsymbol{\gamma} \quad (3.3)$$

The noise properties of this estimator can be made clear by defining the matrix $\widetilde{M}_{\gamma\delta} \equiv \mathcal{N}_{\gamma\gamma}^{-1/2} M_{\gamma\delta}$ and computing the singular value decomposition (SVD) $\widetilde{M}_{\gamma\delta} \equiv U \Sigma V^\dagger$. Here $U^\dagger U = V^\dagger V = \mathbf{I}$ and Σ is the square diagonal matrix of singular values $\sigma_i \equiv \Sigma_{ii}$, ordered such that $\sigma_i \geq \sigma_{i+1}$, $i \geq 1$. Using these properties, the Aitken estimator can be equivalently

written

$$\hat{\delta}_A = \mathbf{V} \mathbf{\Sigma}^{-1} \mathbf{U}^\dagger \mathcal{N}_{\gamma\gamma}^{-1/2} \gamma \quad (3.4)$$

It is apparent in this expression that the presence of small singular values $\sigma_i \ll \sigma_1$ can lead to extremely large diagonal entries in the matrix $\mathbf{\Sigma}^{-1}$, which in turn amplify the errors in the estimator $\hat{\delta}_A$. This can be seen formally by expressing the noise covariance in terms of the components of the SVD:

$$\mathcal{N}_{\delta\delta} = \mathbf{V} \mathbf{\Sigma}^{-2} \mathbf{V}^\dagger. \quad (3.5)$$

This makes clear the connection with KL, as discussed in Chapter 2. The columns of the matrix \mathbf{V} are eigenvectors of $\mathcal{N}_{\delta\delta}$, with eigenvalues σ_i^{-2} . When many small singular values are present, the noise will dominate the reconstruction, and it is necessary to use a more sophisticated estimator to recover the signal.

3.2.2 KL Filtering

One strategy that can be used to reduce this noise is to add a penalty function to the χ^2 that will suppress the large spikes in signal. This is the Wiener filter approach explored by HK02 and STH09. A more direct noise-reduction method, which does not require knowledge of the statistical properties of the signal, involves approximating the SVD in Equation 3.4 to remove the contribution of the high-noise modes. We choose a cutoff value σ_{cut} , and determine n such that $\sigma_n > \sigma_{\text{cut}} \geq \sigma_{n+1}$. We then define the truncated matrices \mathbf{U}_n , $\mathbf{\Sigma}_n$, and \mathbf{V}_n , such that \mathbf{U}_n (\mathbf{V}_n) contains the first n columns of \mathbf{U} (\mathbf{V}), and $\mathbf{\Sigma}_n$ is a diagonal matrix of the largest n singular values, $n \leq n_{\text{max}}$. To the extent that $\sigma_{\text{cut}}^2 \ll \sum_{i=1}^n \sigma_i^2$, the truncated matrices satisfy

$$\mathbf{U}_n \mathbf{\Sigma}_n \mathbf{V}_n^\dagger \approx \mathbf{U} \mathbf{\Sigma} \mathbf{V}^\dagger = \widetilde{\mathbf{M}}_{\gamma\delta} \quad (3.6)$$

and the signal estimator in Equation 3.3 can be approximated by the SVD estimator:

$$\hat{\delta}_{\text{svd}}(n) \equiv \mathbf{V}_n \mathbf{\Sigma}_n^{-1} \mathbf{U}_n^\dagger \mathcal{N}_{\gamma\gamma}^{-1/2} \gamma \quad (3.7)$$

This approximation is optimal in the sense that it preferentially eliminates high-noise orthogonal components in δ (cf. equation 3.5), leading to an estimator which is much more robust to noise in γ .

SVDs are often used in the context of KL or Principal Component Analysis, where the square of the singular value is equal to the variance described by the corresponding principal component (see §2.3.5). The variance can be thought of, roughly, as a measure of the information contributed by the vector to the matrix in question. It will be useful for us to think about SVD truncation in this way. To that end, we define a measure of the truncated variance for a given value of n :

$$v_{\text{cut}}(n) = 1 - \frac{\sum_{i=1}^n \sigma_i^2}{\sum_{i=1}^{n_{\text{max}}} \sigma_i^2} \quad (3.8)$$

such that $0 \leq v_{\text{cut}} \leq 1$. If $v_{\text{cut}} = 0$, then $n = n_{\text{max}}$ and we are using the full Aitken estimator. As $v_{\text{cut}} \rightarrow 1$, we are increasing the amount of truncation.

In practice, taking the SVD of the transformation matrix $\mathcal{N}_{\gamma\gamma}^{-1/2} M_{\gamma\delta}$ is not entirely straightforward: the matrix is of size $(N_{xy} N_s) \times (N_{xy} N_l)$. With a 128×128 -pixel field, 20 lens-planes, and 25 source-planes, the matrix contains 1.3×10^{11} mostly nonzero complex entries, amounting to 2TB in memory (double precision). Computing the SVD for a non-sparse matrix of this size is far from trivial.

We have developed a technique to speed-up this process, which involves decomposing the matrices $\mathcal{N}_{\gamma\gamma}$ and $M_{\gamma\delta}$ into tensor products, so that the full SVD can be determined through computing SVDs of two smaller matrices: an $N_s \times N_l$ matrix, and an $N_{xy} \times N_{xy}$ matrix. The second of these individual SVDs can be approximated using the Fourier-space properties of the $\gamma \rightarrow \kappa$ mapping. The result is that the entire SVD estimator can be computed very quickly. The details of this method are described in Appendix B.

3.3 Results

Using the above formalism, we can now explore the tomographic weak lensing problem using the techniques of Section 3.2. For the following discussion, we will use a field of approximately one square degree: a 64×64 grid of $1' \times 1'$ pixels, with 25 source redshift bins ($0 \leq z \leq 2.0$, $\Delta z = 0.08$) and 20 lens redshift bins ($0 \leq z \leq 2.0$, $\Delta z = 0.1$). This binning approximates the expected photometric redshift errors of future surveys. We suppress edge effects by increasing the noise of all pixels within $4'$ of the field border by a factor of 10^3 , effectively deweighting the signal in these pixels (cf. STH09). The noise for each redshift

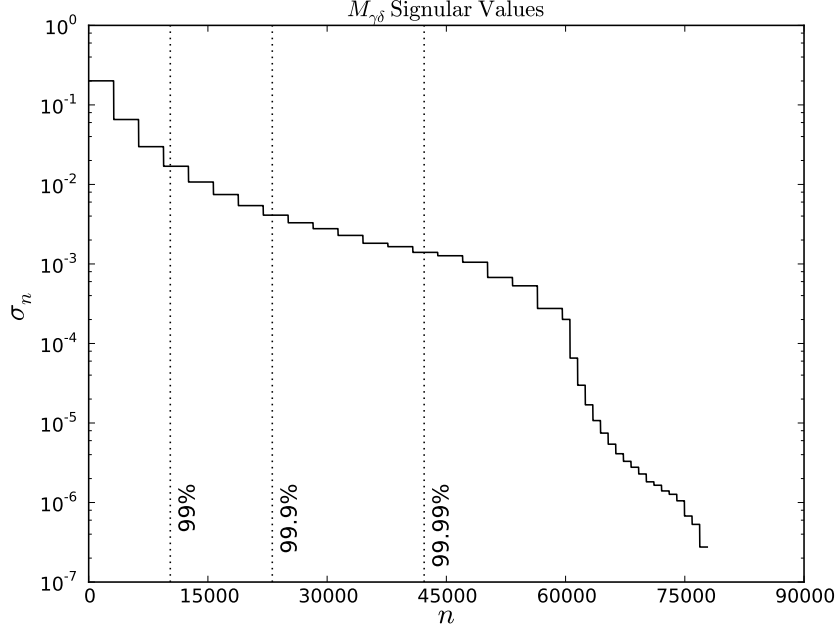


Figure 3.1: Ordered singular values of the matrix $\widetilde{\mathbf{M}}_{\gamma\delta}$. The dotted lines show the values of n such that 99%, 99.9%, and 99.99% of the variance is preserved. The sharp drop-off near $n = 60,000$ is due to the 10^{-3} deweighting of border pixels.

bin is set to $n_i = \sigma_\gamma / \sqrt{N_i}$, where σ_γ is the intrinsic ellipticity dispersion, and N_i is the number of galaxies in the bin. We assume $\sigma_\gamma = 0.3$ (based on the Hubble Deep Field image Mellier, 1999), and 70 galaxies per square arcminute, with a redshift distribution given by

$$n(z) \propto z^2 \exp \left[-(z/z_0)^{3/2} \right], \quad (3.9)$$

with $z_0 = 0.57$. We assume a flat cosmology with $h = 0.7$, $\Omega_M = 0.27$ and $\Omega_\Lambda = 0.73$ at the present day.

3.3.1 Singular Values

The singular values of the transformation matrix for this configuration are depicted in Figure 3.1. The step pattern visible in this plot is due to the fact that the noise across each source plane is identical, aside from the $4'$ deweighted border. It is apparent from this

figure that the large majority of the singular values are very small: 99.9% of the variance in the transformation is contained in less than 1/3 of the singular values. The large number of very small singular values will, therefore, dominate in the Aitken estimator (Equation 3.4), leading to the very noisy unfiltered results seen in HK02.

3.3.2 Evaluation of the SVD Estimator

To evaluate the performance of the SVD filter, we first create a field-of-view containing a single halo at redshift $z = 0.6$. One well-supported parametrization of halo shapes is the NFW profile (Navarro et al., 1997). We use the analytic form of the shear and projected density due to an NFW profile, given by equations 13-18 in Takada & Jain (2003).

We reconstruct the density map using the SVD filter (Figure 3.2) with the above survey parameters. We show the results for three different values of v_{cut} : 0.1, 0.01, and 0.005. In all three cases, the halo is easily detected at its correct location (left panels), although as v_{cut} decreases, there is more noise in the surrounding field. The right panels show the computed density profile along the line of sight for the central pixel. The peak of this curve is close to the correct redshift, but there is a significant spread in redshift, as well as a bias. As the level of SVD filtering (measured by v_{cut}) decreases, the magnitude of these effects decreases, but the increased noise leads to spurious peaks.

Similar plots for the transverse Wiener filter recommended by STH09 are shown in the upper panels of Figure 3.3, using their recommended value of $\alpha = 0.05$. The response shows a significant spread in angular space, and the signal is seen to be suppressed by six orders-of-magnitude along with a similar suppression of the noise. These effects worsen, in general, as the filtering level α increases. Mathematically it is apparent why the transverse filter performs so poorly: the small singular values primarily come from the line-of-sight part of the mapping, and the this filter has no effect along the line-of-sight.

The effect of the radial Wiener filter is shown in the bottom panels of Figure 3.3. It shares the positive aspects of the SVD filter, having very little signal suppression or angular spread. However, this filter uses some priors on the statistical form of the signal that are not as physically well-motivated as those for the transverse Wiener filter. In contrast,

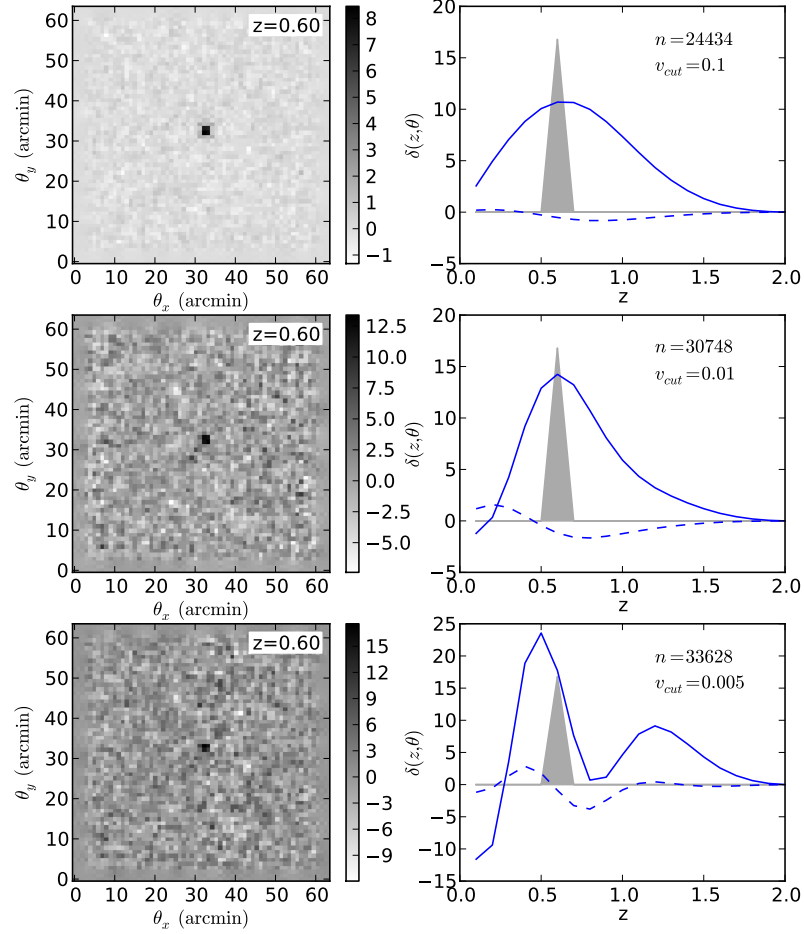


Figure 3.2: The effect of SVD truncation on a single $z = 0.6$ NFW halo in the center of the field, for three different levels of filtering. *left column:* reconstructed density parameter $\delta(\theta)$ in the $z = 0.6$ lens-plane. The true matter distribution is represented by a tight “dot” in the center of the plot. *right column:* line-of-sight profile at the central pixel. The gray shaded area shows the input density parameter. The solid line shows the E-mode signal, while the dashed line shows the B-mode signal. n gives the number of singular values used in the reconstruction (out of a total $n_{\text{max}} = 81920$), and v_{cut} gives the amount of variance cut by the truncation (Equation 3.8); the level of filtration decreases from the top panels to the bottom panels. The bottom panels show a case of under-filtering: for small enough v_{cut} , the noise overwhelms the signal and creates spurious peaks along the line-of-sight.

the SVD filter does not make any prior assumptions about the signal. In this way, the SVD reconstruction can be thought of as even more non-parametric than the Wiener filter reconstructions.

3.3.3 Comparison of Estimators

The SVD framework laid out in Section 3.2.2 can be used to quantitatively compare the behavior of different estimators. A general linear estimator has the form

$$\hat{\delta}_R = R\gamma \quad (3.10)$$

for some matrix R . This general estimator can be expressed in terms of the components of the unbiased estimator (Equation 3.4):

$$R = V_R \Sigma^{-1} U^\dagger \mathcal{N}_{\gamma\gamma}^{-1/2}. \quad (3.11)$$

Here the matrices Σ , U and $\mathcal{N}_{\gamma\gamma}$ are defined as in Equation 3.4, and we have defined the matrix

$$V_R \equiv R \mathcal{N}_{\gamma\gamma}^{1/2} U \Sigma \quad (3.12)$$

The rows of the matrix $\Sigma^{-1} U^\dagger \mathcal{N}_{\gamma\gamma}^{-1/2}$ provide a convenient basis in which to work: they are the weighted principal components of the shear, ordered with decreasing signal to noise. The norm of the i^{th} column of V_R measures the contribution of the i^{th} mode to the reconstruction of δ . For the unfiltered estimator, $V_R = V$ and all the norms are unity. This leads to a very intuitive comparison between different filtering schemes. Figure 3.4 compares the column-norms of V_R for the SVD filter with those of the radial and transverse Wiener filters.

The steps visible in the plot originate the same way as the steps in Figure 3.1: the flatness of each step comes from the assumption of uniform noise in each source plane. This plot shows the tradeoff between noise and bias. The flat line at norm=10⁰ represents a noisy but unbiased estimator. Any departure from this will impose a bias, but can increase signal-to-noise. There are two important observations from this figure. First, because each step on the plot is relatively flat for the SVD filter and radial Wiener filter, we don't expect much bias *within* each lens plane. The transverse filter, on the other hand, has fluctuations at the 10%

level within each step (visible in the inset of Figure 3.4), which will lead to a noticeable bias within each lens plane, resulting in the degraded angular resolution of the reconstruction seen in Figure 3.3. Second, the transverse Wiener filter deweights even the highest signal-to-noise modes by many orders of magnitude, resulting in the signal suppression seen in Figure 3.3. The SVD filter and radial Wiener filter, on the other hand, have weights near unity for the highest signal-to-noise modes. These two observations show why the SVD filter and radial Wiener filter are the more successful noise reduction techniques for the present problem.

3.3.4 Noise Properties of Line-of-Sight Modes

As seen in equation 3.5, the columns of \mathbf{V} provide a natural orthogonal basis in which to express the signal $\boldsymbol{\delta}$. It should be emphasized that this eigenbasis is valid for any linear filtering scheme: the untruncated SVD is simply an equivalent re-expression of the original transformation. Examining the characteristics of these eigenmodes can yield insight regardless of the filtering method used.

The radial components of the first four eigenmodes are plotted in figure 3.5. Each is labeled by its normalized noise level, $n_i \equiv (\sigma_i/\sigma_1)^{-1}$. The total number of modes will be equal to the number of output redshift bins; here, for clarity, we've used 80 equally-spaced bins out to redshift 2.0. As the resolution is lessened, the overall shape and relative noise level of the lower-order modes is maintained. These radial modes are analogous to angular Fourier modes, and are related to the signal-to-noise KL modes discussed in HK02. It is clear from this plot that any linear, non-parametric estimator will be fundamentally limited in its redshift resolution: the noise level of the i^{th} mode approximately scales as

$$n_i \propto i^2 \tag{3.13}$$

The signal-to-noise level for any particular halo will depend on its mass and redshift. The magnitude of the signal scales linearly with mass (see discussion in STH09), but the redshift dependence is more complicated: it is affected by the lensing efficiency function, which depends on the redshift of the lensed galaxies. Using the above survey parameters, with an NFW halo of mass $M_{200} = 10^{15} M_\odot$ and redshift $z = 0.6$, the signal-to-noise ratio of the

central pixel for the fundamental radial mode is ~ 5.9 , consistent with the results for Wiener filtered reconstructions of singular isothermal halos explored in STH09. This means that for even the largest halos, with a very deep survey, only the first few modes will contribute significantly to the reconstructed halo. Adding higher-order modes can in theory provide redshift information, but at the cost of increasingly high noise contamination. This is a general result which will apply to all nonparametric linear reconstruction algorithms.

This lack of information in the redshift direction leads directly to an inability to accurately determine halo masses: the lensing equations relate observed shear γ to density parameter δ , which is related to mass in a redshift-dependent way. This is a fundamental limitation on the ability of linear nonparametric methods to determine halo masses from shear data. Indeed, even moving to fully parametric models, line-of-sight effects can lead to halo mass errors of 20% or more (Hoekstra, 2003; de Putter & White, 2005).

3.3.5 *Reconstruction of a Realistic Field*

To compare the performance of the three filtering methods for a realistic field, we create a 4 square degree field with approximately 20 halos between masses of 2×10^{14} and $8 \times 10^{14} M_{\odot}$ with a mass distribution approximating the cluster mass function of Rines et al. (2007), and a redshift distribution given by Equation 3.9, adding a hard cutoff at $z = 1.0$. These parameters are chosen to approximate the true distribution of observable halos in a field this size. The results of the reconstruction are shown in Figure 3.6

The red circles are the locations of the input halos, not the result of some halo-detection algorithm. However, it is clear that, for at least most of the mass range, we are able to produce a map for which any reasonable detection algorithm should detect the halos in the correct locations. A few of the lower mass halos would certainly be missed though, since they are not significantly different from the noise peaks in the image.

In practice, one may vary the parameter v_{cut} as in Figure 3.2 to trade-off robustness of detecting peaks with resolution in angle and in redshift. As shown in Section 3.3.3, we expect filtering to introduce very little bias in angular resolution, so large values of v_{cut} lead to the most robust angular results. On the other hand, as shown in Section 3.3.4,

filtering introduces an extreme bias along the line-of-sight. The effects of this bias can be seen qualitatively in the right column of Figure 3.2. Optimal redshift resolution requires choosing a filtering level which balances the effects of noise and bias, and may require some form of bias correction. In future work, we will explore in detail the ways in which the SVD method allows for a near optimal reconstruction of projected mass maps and halo redshifts from data on galaxy shapes and photometric redshifts.

3.3.6 Scalability

As we look forward to future surveys, it becomes important to consider methods that will scale upward with increasing survey volumes. Present weak lensing surveys cover fields on the order of a few square degrees (e.g. COSMOS, Massey et al., 2007). Future surveys will increase the field size exponentially: up to $\sim 20,000$ square degrees for LSST (LSST Science Collaborations et al., 2009). Though the flat-sky approximation used in this work is not appropriate for such large survey areas, the weak lensing formalism can be modified to account for spherical geometry (see, e.g. Heavens, 2003).

The main computational cost for both SVD and Wiener filtering is the Fast Fourier Transform (FFT) required to implement the mapping from γ to κ . For an $N \times N$ pixel field, the FFT algorithm performs in $\mathcal{O}[N \log N]$ in each dimension, meaning that the 2D FFT takes $\mathcal{O}[(N \log N)^2] \approx \mathcal{O}[N^2]$. The Wiener filter method, however, requires the inversion of a very large matrix using, for example, a conjugate-gradient method. The exact number of iterations depends highly on the condition number of the matrix to be inverted; STH09 finds that up to 150 iterations are required for this problem. We find that *each iteration* takes over 3 times longer than the entire SVD reconstruction. The net result is that both algorithms scale nearly linearly with the area of the field (for constant pixel scale), though the SVD estimator is computed up to 500 times faster than the Wiener filter.

Extrapolating this scaling, the appropriately scaled SVD filter will allow reconstruction of the entire $\sim 20,000$ square-degree LSST field in a few hours on a single \sim GHz processor, given enough memory. On the same computer, the Wiener-filter method would take over a month, depending on the amount and type of filtering and assuming that the required

Table 3.1: Masses and redshifts of halos in Figure 3.6.

| | θ_x | θ_y | z | M/M_\odot |
|---|------------|------------|------|----------------------|
| A | 37.5 | 44.9 | 0.60 | 7.2×10^{14} |
| B | 67.1 | 70.5 | 0.47 | 6×10^{14} |
| C | 46.9 | 106.5 | 0.63 | 5.5×10^{14} |
| D | 108.9 | 94.3 | 0.63 | 5.4×10^{14} |
| E | 97.9 | 63.6 | 0.39 | 4.9×10^{14} |
| F | 102.4 | 84.8 | 0.70 | 3.8×10^{14} |
| G | 77.0 | 49.6 | 0.58 | 3.2×10^{14} |
| H | 52.0 | 48.5 | 0.36 | 3.2×10^{14} |
| I | 72.6 | 45.6 | 0.78 | 2.9×10^{14} |
| J | 68.6 | 64.5 | 0.68 | 2.5×10^{14} |
| K | 8.6 | 34.5 | 0.32 | 2.3×10^{14} |
| L | 10.5 | 49.5 | 0.51 | 2.3×10^{14} |
| M | 99.4 | 56.5 | 0.22 | 2.3×10^{14} |
| N | 21.7 | 53.1 | 0.76 | 2.3×10^{14} |
| O | 31.6 | 102.1 | 0.69 | 2.2×10^{14} |
| P | 69.7 | 33.2 | 0.39 | 2.2×10^{14} |

number of iterations stays constant with increasing field size. For the SVD-filtered reconstruction of this large field, the real challenge will not be computational time, but memory constraints: the complex shear vector itself for such a field will require ~ 30 GB of memory, with the entire algorithm consuming approximately three times this. The memory requirements for the Wiener filter will be comparable. This is within reach of current high-end workstations as well as shared-memory parallel clusters.

3.4 Conclusion

We have presented a new method for producing tomographic maps of dark matter through weak lensing, using truncation of singular values. We have tested and compared our method

to the Wiener filter based method of STH09, which is the first three-dimensional mass mapping approach that is applicable to large area surveys. Our reconstruction shares many of the aspects of the Wiener filter reconstruction, in the sense that it massively reduces the noise inherent in the problem. Our SVD method may be considered even more non-parametric than the Wiener filter method, since it does not rely on any a priori assumptions of the statistical properties of the signal: all of the noise reduction is derived from the observed noise properties of the data.

The SVD framework allows a unique quantitative comparison between the different filtering methods and filtering strengths. Using the coefficients of the weighted principal components contained in the SVD, we have compared the three filtering methods, and have found that the radial Wiener filter of HK02 and SVD filter of this work are less-biased noise reduction techniques than the transverse Wiener filter of STH09. These authors have recently implemented the radial Wiener filter and obtain results consistent with our findings (P. Simon and A. Taylor, private communication).

The angular resolution of the SVD-reconstructed mass maps seems to be significantly better than that of the transverse Wiener filter method, the method chosen in the STH09 analysis. This allows for more robust separation of pairs of halos into two separate halos rather than blurring them into a single mass peak. We discuss how our reconstruction method provides a scheme for optimizing the 3D reconstruction of projected mass maps by balancing the goals of robustness of detecting specific structures and improved redshift resolution.

The SVD method can compute the three-dimensional mass maps rapidly provided sufficient computational memory is available. This allows for the possibility of solving the full-sky tomographic lensing inversion on the scale of hours, rather than months, which makes it readily applicable to upcoming surveys.

On the other hand, the redshift resolution with the SVD method is not significantly better than that of either Wiener filter method. This was a problem identified by STH09, and unfortunately the SVD method does not significantly improve the situation. Our analysis of the noise characteristics of radial modes indicates that linear, non-parametric reconstruction methods are fundamentally limited in this regard.

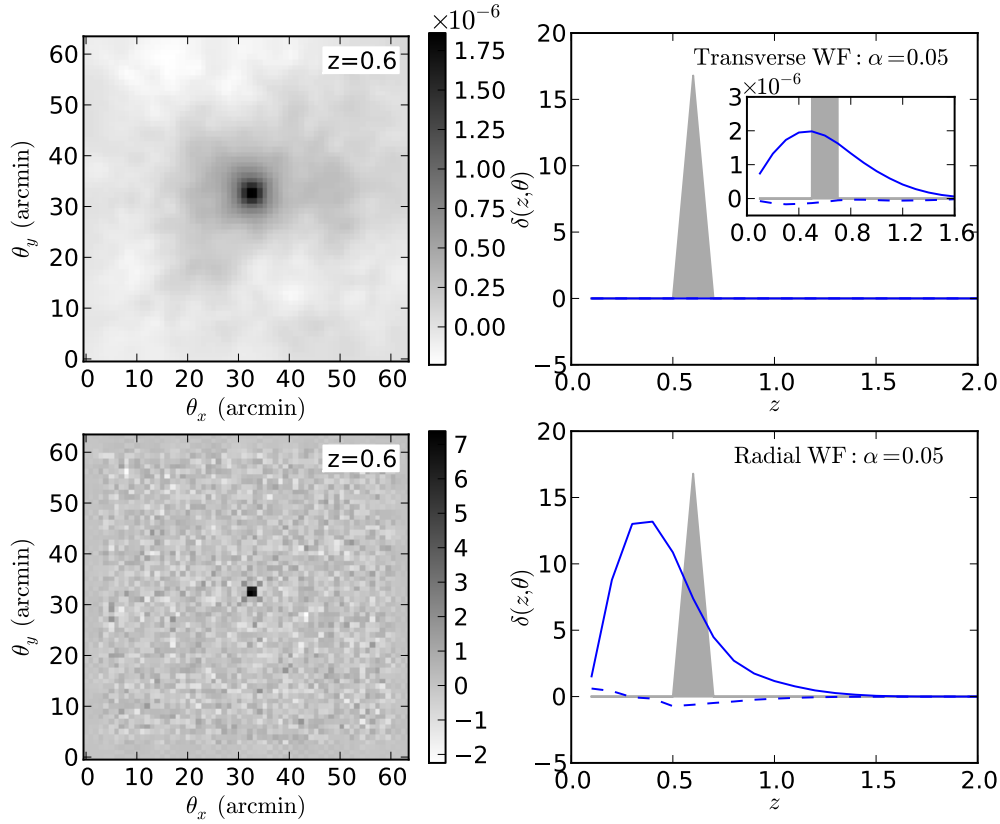


Figure 3.3: The effect of Wiener filtering on the same input as Figure 3.2. Here we have used both transverse (*top panels*) and radial (*bottom panels*) Wiener filtering, both down-tuned by $\alpha = 0.05$ (the value recommended by STH09). The transverse Wiener filter suppresses the response by several orders of magnitude; a closer view of the line-of-sight peak is shown in the inset plot. The radial Wiener filter gives similar angular results to the SVD filter, but takes much longer to compute.

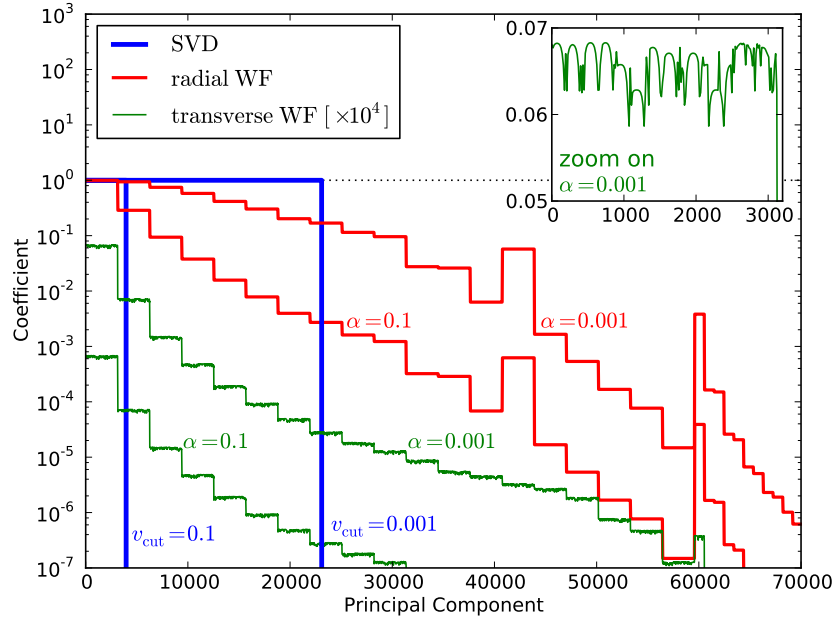


Figure 3.4: Contribution of each shear mode to the reconstruction for three different filters. The dotted line at 10^0 represents the unfiltered result. Each filtering method leads to a different weighting of the shear modes. The SVD filter, by design, completely removes higher-order modes beyond a given cutoff, while the Wiener filter deweights modes in a more gradual fashion. Note that the transverse Wiener filter deweights all modes by up to seven orders of magnitude; it has been scaled by a factor of 10^4 for this plot. The inset plot shows a closeup of the fluctuations within each “step” of the transverse filter. These fluctuations lead to angular spread in the response (see discussion in Section 3.3.3)

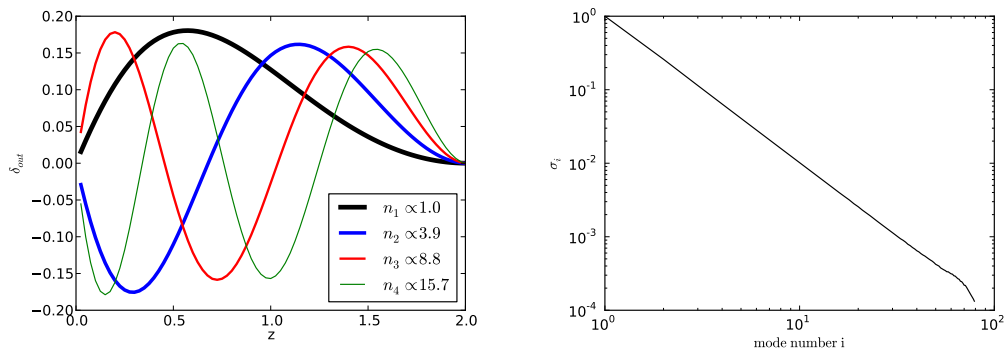


Figure 3.5: *left panel:* The radial components of the first four columns of the matrix \mathbf{V} (see section 3.2.1). This is calculated for 100 equally spaced redshift bins ($0 \leq z \leq 2.5$) in γ , and 80 bins ($0 \leq z \leq 2.0$) in δ . These orthogonal eigenmodes are analogous to radial Fourier modes. Each is labeled by its relative noise level, $n_i = (\sigma_i/\sigma_1)^{-1}$. *right panel:* The singular values σ_i associated with the 80 radial eigenmodes.

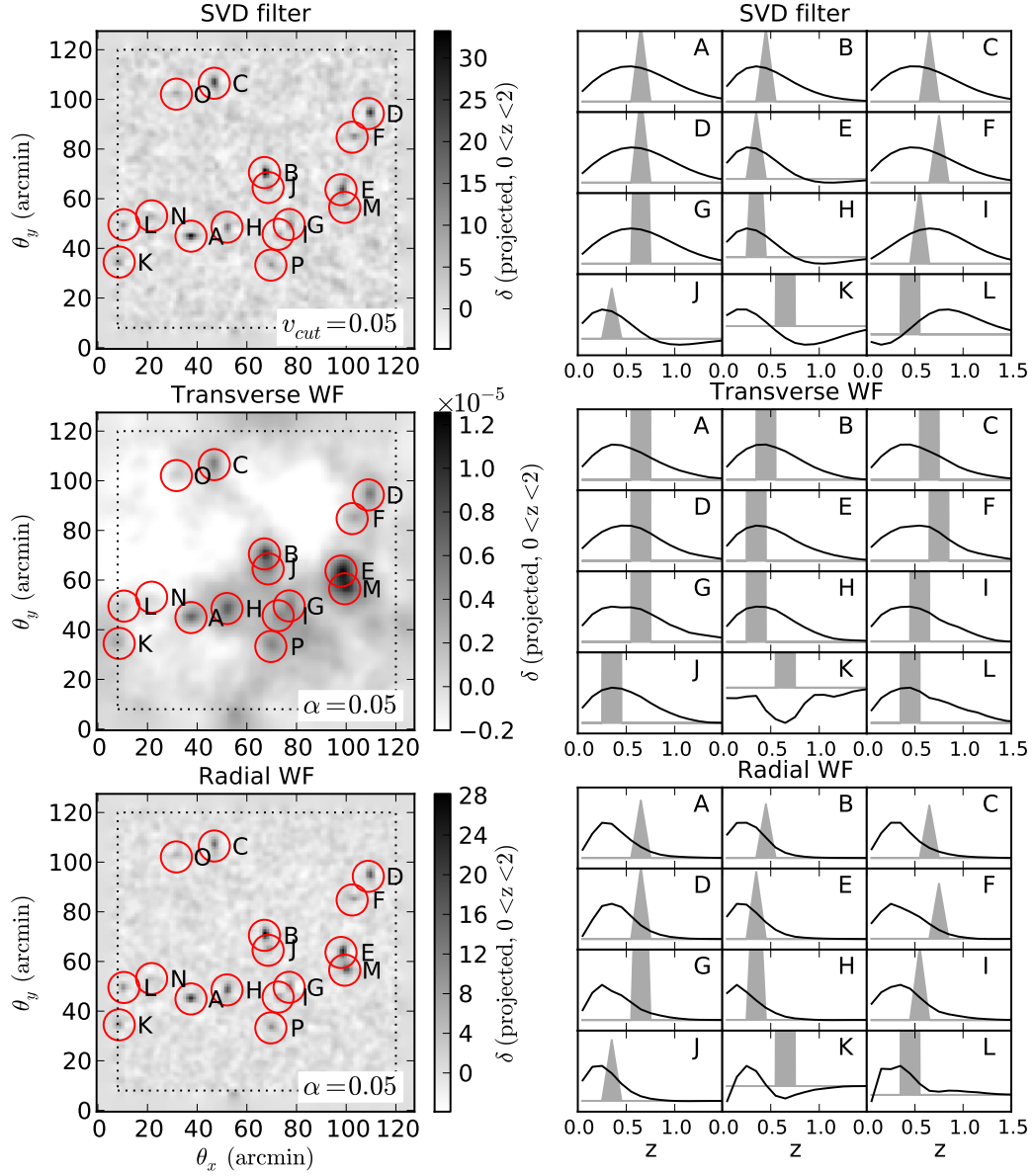


Figure 3.6: Reconstruction of an artificial shear field with the SVD filter (*top panels*), Transverse Wiener filter (*middle panels*), and Radial Wiener filter (*bottom panels*). The left column shows the projected density reconstruction across the field using each method, all smoothed with a 1-pixel wide Gaussian filter. Red circles indicate the true locations of the input halos. The right column shows the line-of-sight distributions of the twelve most massive NFW halos, labeled A-L. The masses and redshifts of the halos are listed in Table 3.1. The signal suppression of the transverse Wiener filter seen in Figure 3.3 is apparent in the color-bar scaling of the middle panels. The anomalous results seen in halo K are due to its proximity to the deweighted border. As suggested by the discussion in Section 3.3.4, none of the three methods succeed in recovering precise redshifts of the halos.

Chapter 4

SHEAR PEAK STATISTICS WITH KL

This chapter will cover the results from VanderPlas et al. (2012). In it, we explore the utility of Karhunen Loève (KL) analysis in solving practical problems in the analysis of gravitational shear surveys, with a specific application to cosmological constraints from shear peak statistics. Shear catalogs from large-field weak lensing surveys will be subject to many systematic limitations, notably incomplete coverage and pixel-level masking due to foreground sources. We develop a method to use two dimensional KL eigenmodes of shear to interpolate noisy shear measurements across masked regions. We explore the results of this method with simulated shear catalogs, using statistics of high-convergence regions in the resulting map. We find that the KL procedure not only minimizes the bias due to masked regions in the field, it also reduces spurious peak counts from shape noise by a factor of ~ 3 in the cosmologically sensitive regime. This indicates that KL reconstructions of masked shear are not only useful for creating robust convergence maps from masked shear catalogs, but also offer promise of improved parameter constraints within studies of shear peak statistics.

This chapter was originally published in collaboration with Andrew Connolly, Bhuvnesh Jain, and Mike Jarvis in the January 2012 edition of the *Astronomical Journal* (VanderPlas et al., 2012, ApJ, Vol. 744, p. 180; © 2012 by the American Astronomical Society) and is reproduced below with permission of the American Astronomical Society.

4.1 Introduction

Currently, a new generation of wide-field weak lensing surveys are in the planning and construction stages. Among them are the the Dark Energy Survey (DES), the Panoramic Survey Telescope & Rapid Response System (PanSTARRS), the Wide Field Infrared Survey Telescope (WFIRST), and the Large Synoptic Survey Telescope (LSST), to name a few.

These surveys, though not as deep as small-field space-based lensing surveys, will cover orders-of-magnitude more area on the sky: up to $\sim 20,000$ square degrees in the case of LSST.

This is a fundamentally different regime than early weak lensing reconstructions of single massive clusters: the strength of the shear signal is only $\sim 1\%$, and is dominated by $\sim 30\%$ intrinsic shape noise. This, combined with source galaxy densities of only $n \sim 20 - 50 \text{ arcmin}^{-2}$ (compared with $n > 100 \text{ arcmin}^{-2}$ for deep, space-based surveys) and atmospheric PSF effects leads to a situation where the signal is very small compared to the noise. Additionally, in the wide-field regime, the above-mentioned priors cannot be used. Nevertheless, many methods have been developed to extract useful information from wide-field cosmic shear surveys, including measuring the N-point power spectra and correlation functions (Schneider et al., 2002a; Takada & Jain, 2004; Hikage et al., 2010), performing log transforms of the convergence field (Neyrinck et al., 2009, 2010; Scherrer et al., 2010; Seo et al., 2011), analyzing statistics of convergence and aperture mass peaks (Marian et al., 2010; Dietrich & Hartlap, 2010; Schmidt & Rozo, 2010; Kratochvil et al., 2010; Maturi et al., 2011). Another well-motivated application of wide-field weak lensing is using wide-field mass reconstructions to minimize the effect mass-sheet degeneracy in halo mass determination.

Many of the above applications require reliable recovery of the projected density, either in the form of the convergence κ , or filter-based quantities such as aperture mass (Schneider et al., 1998). Because each of these amounts to a non-local filtering of the shear, the presence of masked regions can lead to a bias across significant portions of the resulting maps. Many of these methods have been demonstrated only within the context of idealized surveys, with exploration of the complications of real-world survey geometry left for future study. Correction for masked pixels has been studied within the context of shear power spectra (Schneider et al., 2010; Hikage et al., 2010) but has not yet been systematically addressed within the context of mapmaking and the associated statistical methods (see, however, Padmanabhan et al., 2003; Pires et al., 2009, for some possible approaches). We propose to address this missing data problem through Karhunen-Loève (KL) analysis.

In Section 4.2 we summarize the theory of KL analysis in the context of shear measurements, including the use of KL for interpolation across masked regions of the observed field.

In Section 4.3 we show the shear eigenmodes for a particular choice of survey geometry, and use these eigenmodes to interpolate across an artificially masked region in a simulated shear catalog. In Section 4.4 we discuss the nascent field of “shear peak statistics”, the study of the properties of projected density peaks, and propose this as a test of the possible bias imposed by KL analysis of shear. In Section 4.5 we utilize simulated shear catalogs in order to test the effect of KL interpolation on the statistics of shear peaks.

4.2 *Karhunen-Loève Analysis of Shear*

As discussed in Chapter 2, KL analysis is a commonly used statistical tool in a broad range of astronomical applications, from, e.g. studies of galaxy and quasar spectra (Connolly et al., 1995; Connolly & Szalay, 1999; Yip et al., 2004a,b), to analysis of the spatial distribution of galaxies (Vogeley & Szalay, 1996; Matsubara et al., 2000; Pope et al., 2004), to characterization of the expected errors in weak lensing surveys (Kilbinger & Munshi, 2006; Munshi & Kilbinger, 2006). A full description of KL analysis is presented in Chapter 2; here we will briefly review the points relevant to this chapter.

In general, any set of N -dimensional data can be represented as a sum of N orthogonal basis functions: this amounts to a rotation and scaling of the N -dimensional coordinate axis spanning the space in which the data live. KL analysis seeks a set of orthonormal basis functions which can optimally represent the dataset. The sense in which the KL basis is optimal will be discussed below. For the current work, the data we wish to represent are the observed gravitational shear measurements across the sky. We will divide the survey area into N discrete cells, at locations \mathbf{x}_i , $1 \leq i \leq N$. From the ellipticity of the galaxies within each cell, we infer the observed shear $\gamma^o(\mathbf{x}_i)$, which we assume to be a linear combination of the true underlying shear, $\gamma(\mathbf{x}_i)$ and the shape noise $n_\gamma(\mathbf{x}_i)$.¹ In general, the cells may be of any shape (even overlapping) and may also take into account the redshift of sources. In this analysis, the cells will be square pixels across the locally flat shear field, with no use of source redshift information. For notational clarity, we will represent quantities with a vector notation, denoted by bold face: i.e. $\boldsymbol{\gamma} = [\gamma_1, \gamma_2 \cdots]^T$; $\gamma_i = \gamma(\mathbf{x}_i)$.

¹Throughout this chapter, we assume we are in the regime where the convergence $\kappa \ll 1$ so that the average observed ellipticity in a cell is an unbiased estimator of shear; see Bartelmann & Schneider (2001)

4.2.1 KL Formalism

As discussed in Chapter 2, KL analysis provides an optimal framework such that our measurements γ can be expanded in a set of N orthonormal basis functions $\{\Psi_j(\mathbf{x}_i), j = 1, N\}$, via a vector of coefficients \mathbf{a} . In matrix form, the KL projection of the observed shear can be written

$$\gamma = \Psi \mathbf{a} \quad (4.1)$$

where the columns of the matrix Ψ are the basis vectors Ψ_i . Orthonormality is given by the condition $\Psi_i^\dagger \Psi_j = \delta_{ij}$, so that the coefficients can be determined by

$$\mathbf{a} = \Psi^\dagger \gamma \quad (4.2)$$

A KL decomposition is optimal in the sense that it seeks basis functions for which the coefficients are statistically orthogonal;² that is, they satisfy

$$\langle a_i^* a_j \rangle = \langle a_i^2 \rangle \delta_{ij} \quad (4.3)$$

where angled braces $\langle \dots \rangle$ denote averaging over all realizations. This definition leads to several important properties (see Vogeley & Szalay, 1996, for a thorough discussion & derivation):

1. **KL as an Eigenvalue Problem:** Defining the correlation matrix $\xi_{ij} = \langle \gamma_i \gamma_j^* \rangle$, it can be shown that the KL vectors Ψ_i are eigenvectors of ξ with eigenvalues $\lambda_i = \langle a_i^2 \rangle$. For clarity, we'll order the eigenbasis such that $\lambda_i \geq \lambda_{i+1} \forall i \in (1, N-1)$. We define the diagonal matrix of eigenvalues Λ , such that $\Lambda_{ij} = \lambda_i \delta_{ij}$ and write the eigenvalue decomposition in compact form:

$$\xi = \Psi \Lambda \Psi^\dagger \quad (4.4)$$

2. **KL as a Ranking of Signal-to-Noise** It can be shown that KL vectors of a whitened covariance matrix (see Section 4.2.2) diagonalize both the signal and the noise of the problem, with the signal-to-noise ratio proportional to the eigenvalue. This is why KL modes are often called “Signal-to-noise eigenmodes”.

²Note that statistical orthogonality of coefficients is conceptually distinct from the geometric orthogonality of the basis functions themselves; see Vogeley & Szalay (1996) for a discussion of this property.

3. **KL as an Optimal Low-dimensional Representation:** An important consequence of the signal-to-noise properties of KL modes is that the optimal rank- n representation of the data is contained in the KL vectors corresponding to the n largest eigenvalues: that is,

$$\hat{\gamma}^{(n)} \equiv \sum_{i=1}^{n < N} a_i \Psi_i \quad (4.5)$$

minimizes the reconstruction error between $\hat{\gamma}^{(n)}$ and γ for reconstructions using n orthogonal basis vectors. This is the theoretical basis of Principal Component Analysis (sometimes called Discrete KL), and leads to a common application of KL decomposition: filtration of noisy signals. For notational compactness, we will define the truncated eigenbasis $\Psi_{(n)}$ and truncated vector of coefficients $\mathbf{a}_{(n)}$ such that Equation 4.5 can be written in matrix form: $\hat{\gamma}^{(n)} = \Psi_{(n)} \mathbf{a}_{(n)}$.

4.2.2 KL in the Presence of Noise

When noise is present in the data, the above properties do not necessarily hold. To satisfy the statistical orthogonality of the KL coefficients \mathbf{a} and the resulting signal-to-noise properties of the KL eigenmodes, it is essential that the noise in the covariance matrix be “white”: that is, $\mathcal{N}_\gamma \equiv \langle \mathbf{n}_\gamma \mathbf{n}_\gamma^\dagger \rangle \propto \mathbf{I}$. This can be accomplished through a judicious choice of binning, or by rescaling the covariance with a whitening transformation. We take the latter approach here.

Defining the noise covariance matrix \mathcal{N}_γ as above, the whitened covariance matrix can be written $\xi_W = \mathcal{N}_\gamma^{-1/2} \xi \mathcal{N}_\gamma^{-1/2}$. Then the whitened KL modes become $\Psi_W \Lambda_W \Psi_W^\dagger \equiv \xi_W$. The coefficients \mathbf{a}_W are calculated from the noise-weighted signal, that is

$$\mathbf{a}_W = \Psi_W^\dagger \mathcal{N}_\gamma^{-1/2} (\gamma + \mathbf{n}_\gamma) \quad (4.6)$$

For the whitened KL modes, if signal and noise are uncorrelated, this leads to $\langle \mathbf{a}_W \mathbf{a}_W^\dagger \rangle = \Lambda_W + \mathbf{I}$: that is, the coefficients \mathbf{a}_W are statistically orthogonal. For the remainder of this work, we will drop the subscript “ W ” and assume all quantities to be those associated with the whitened covariance.

4.2.3 Computing the Shear Correlation Matrix

The KL reconstruction of shear requires knowledge of the form of the pixel-to-pixel correlation matrix ξ . In many applications of KL (e.g. analysis of galaxy spectra, Connolly et al., 1995) this correlation matrix is determined empirically from many realizations of the data (i.e. the set of observed spectra). In the case of weak lensing shear, we generally don't have many realizations of the data, so this approach is not tenable. Instead, we compute this correlation matrix analytically. The correlation of the cosmic shear signal between two regions of the sky A_i and A_j is given by

$$\begin{aligned}\xi_{ij} &= \langle \gamma_i \gamma_j^* \rangle + \langle n_i n_j^* \rangle \\ &= \left[\int_{A_i} d^2 x_i \int_{A_j} d^2 x_j \xi_+(|\mathbf{x}_i - \mathbf{x}_j|) \right] + \delta_{ij} \frac{\sigma_\epsilon^2}{\bar{n}}\end{aligned}\quad (4.7)$$

where σ_ϵ is the intrinsic shape noise (typically assumed to be ~ 0.3), \bar{n} is the average galaxy count per pixel, and $\xi_+(\theta)$ is the “+” shear correlation function (Schneider et al., 2002a). $\xi_+(\theta)$ can be expressed as an integral over the shear power spectrum:

$$\xi_+(\theta) = \frac{1}{2\pi} \int_0^\infty d\ell \ell P_\gamma(\ell) J_0(\ell\theta) \quad (4.8)$$

where J_0 is the zeroth-order Bessel function of the first kind. The shear power spectrum $P_\gamma(\ell)$ can be expressed as an appropriately weighted line-of-sight integral over the 3D mass power spectrum (see, e.g. Takada & Jain, 2004):

$$P_\gamma(\ell) = \int_0^{\chi_s} d\chi W^2(\chi) \chi^{-2} P_\delta\left(k = \frac{\ell}{\chi}; z(\chi)\right) \quad (4.9)$$

Here χ is the comoving distance, χ_s is the distance to the source, and $W(\chi)$ is the lensing weight function,

$$W(\chi) = \frac{3\Omega_{m,0}H_0^2}{2a(\chi)} \frac{\chi}{\bar{n}_g} \int_{z(\chi)}^{z(\chi_s)} dz n(z) \frac{\chi(z) - \chi}{\chi(z)} \quad (4.10)$$

where $n(z)$ is the redshift distribution of galaxies. We assume a DES-like survey, where $n(z)$ has the approximate form

$$n(z) \propto z^2 \exp[-(z/z_0)^{1.5}] \quad (4.11)$$

with $z_0 = 0.5$, where $n(z)$ is normalized to the observed galaxy density $\bar{n}_g = 20 \text{ arcmin}^{-2}$.

The 3D mass power spectrum $P_\delta(k, z)$ in Equation 4.9 can be computed theoretically. In this work we compute $P_\delta(k, z)$ using the halo model of Smith et al. (2003), and compute the correlation matrix ξ using Equations 4.7-4.11. When computing the double integral of Equation 4.7, we calculate the integral in two separate regimes: for large separations ($\theta > 20$ arcmin), we assume $\xi_+(\theta)$ doesn't change appreciably over the area of the pixels, so that only a single evaluation of the $\chi_+(\theta)$ is necessary for each pixel pair. For smaller separations, this approximation is insufficient, and we evaluate ξ_{ij} using a Monte-Carlo integration scheme. Having calculated the theoretical correlation matrix ξ for a given field, we compute the KL basis directly using an eigenvalue decomposition.

4.2.4 Which Shear Correlation?

Above we note that the correlation matrix of the measured shear can be expressed in terms of the “+” correlation function, $\xi_+(\theta)$. This is not the only option for measurement of shear correlations (see, e.g. Schneider et al., 2002a). So why use $\xi_+(\theta)$ rather than $\xi_-(\theta)$? The answer lies in the KL formalism itself. The KL basis of a quantity γ is constructed via its correlation $\langle \gamma \gamma^\dagger \rangle$. Because of the complex conjugation involved in this expression, the only relevant correlation function for KL is $\xi_+(\theta)$ *by definition*. Nevertheless, one could object that by neglecting ξ_- , KL under-utilizes the theoretical information available about the correlations of cosmic shear. However, in the absence of noise, the two correlation functions contain identical information: either function can be determined from the other. In this sense, the above KL formalism uses all the shear correlation information that is available.

One curious aspect of this formalism is that the theoretical covariance matrix and associated eigenmodes are real-valued, while the shear we are trying to reconstruct is complex-valued. This can be traced to the computation of the shear correlation:

$$\xi_+ \equiv \langle \gamma \gamma^* \rangle = \langle \gamma_t \gamma_t \rangle + \langle \gamma_\times \gamma_\times \rangle + i[\langle \gamma_t \gamma_\times \rangle - \langle \gamma_\times \gamma_t \rangle] \quad (4.12)$$

By symmetry, the imaginary part of this expression is zero. At first glance, this might seem a bit strange: how can a complex-valued data vector be reconstructed from a real-valued orthogonal basis? The answer lies in the complex KL coefficients a_i : though each KL mode contributes only a single phase across the field (given by the phase of the associated a_i), the

reconstruction has a plurality of phases due to the varying magnitudes of the contributions at each pixel (given by the elements of each basis vector Ψ_i).

An important consequence of this observation is that the KL modes themselves are not sensitive by construction to the E-mode (curl-free) and B-mode (divergence-free) components of the shear field. As we will show below, however, the signal-to-noise properties of KL modes lead to some degree of sensitivity to the E and B-mode information in a given shear field (See Section 4.5).

4.2.5 Interpolation using KL Modes

Shear catalogs, in general, are an incomplete and inhomogeneous tracer of the underlying shear field, and some regions of the field may contain no shear information. This sparsity of data poses a problem, because the KL modes are no longer orthogonal over the incomplete field. Connolly & Szalay (1999) demonstrated how this missing-information problem can be addressed for KL decompositions of galaxy spectra. This application is discussed in more detail in Chapter 2; here we will briefly summarize the results using the notation of shear studies. First we define the weight function $w(\mathbf{x}_i)$. The weight function can be defined in one of two ways: a binary weighting convention where $w(\mathbf{x}_i) = 0$ in masked pixels and 1 elsewhere, or a continuous weighting convention where $w(\mathbf{x}_i)$ scales inversely with the noise $[\mathcal{N}_\gamma]_{ii}$. The binary weighting convention treats the noise as part of the data, and so the measurements should be whitened as outlined in Section 4.2.2. The continuous weighting convention assumes the noise is part of the mask, so data and noise are not whitened. We find that the two approaches lead to qualitatively similar results, and choose to use the binary weighting convention for the simplicity of comparing masked and unmasked cases.

Let γ^o be the observed data vector, which is unconstrained where $w(\mathbf{x}_i) = 0$. Then we can obtain the KL coefficients a_i by minimizing the reconstruction error of the whitened data

$$\chi^2 = (\mathcal{N}_\gamma^{-1/2} \gamma^o - \Psi_{(n)} \mathbf{a}_{(n)})^\dagger \mathbf{W} (\mathcal{N}_\gamma^{-1/2} \gamma^o - \Psi_{(n)} \mathbf{a}_{(n)}) \quad (4.13)$$

where we have defined the diagonal weight matrix $\mathbf{W}_{ij} = w(\mathbf{x}_i) \delta_{ij}$. Minimizing Equa-

tion 4.13 with respect to \mathbf{a} leads to the optimal estimator $\hat{\mathbf{a}}$, which can be expressed

$$\hat{\mathbf{a}}_{(n)} = \mathbf{M}_{(n)}^{-1} \mathbf{\Psi}_{(n)}^\dagger \mathbf{W} \mathcal{N}_\gamma^{-1/2} \gamma^o \quad (4.14)$$

Where we have defined the mask convolution matrix $\mathbf{M}_{(n)} \equiv \mathbf{\Psi}_{(n)}^\dagger \mathbf{W} \mathbf{\Psi}_{(n)}$. These coefficients $\hat{\mathbf{a}}_{(n)}$ can then be used to construct an estimator for the unmasked shear field:

$$\hat{\gamma}^{(n)} = \mathcal{N}_\gamma^{1/2} \mathbf{\Psi}_{(n)} \hat{\mathbf{a}}_{(n)} \quad (4.15)$$

In cases where the mask convolution matrix $\mathbf{M}_{(n)}$ is singular or nearly singular, the estimator in Equation 4.15 can contain unrealistically large values within the reconstruction $\hat{\gamma}^{(n)}$. This can be addressed either by reducing n , or by adding a penalty function to the right side of Equation 4.13. One convenient form of this penalty is the generalized Wiener filter (see Tegmark, 1997), which penalizes results which deviate from the expected correlation matrix. Because the correlation matrix has already been computed when determining the KL modes, this filter requires very little extra computation. With Wiener filtering, Equation 4.13 becomes

$$\begin{aligned} \chi^2 &= (\mathcal{N}_\gamma^{-1/2} \gamma^o - \mathbf{\Psi}_{(n)} \mathbf{a}_{(n)})^\dagger \mathbf{W} (\mathcal{N}_\gamma^{-1/2} \gamma^o - \mathbf{\Psi}_{(n)} \mathbf{a}_{(n)}) \\ &\quad + \alpha \mathbf{a}_{(n)}^\dagger \mathbf{C}_{a(n)}^{-1} \mathbf{a}_{(n)} \end{aligned} \quad (4.16)$$

where $\mathbf{C}_{a(n)} \equiv \langle \mathbf{a}_{(n)} \mathbf{a}_{(n)}^\dagger \rangle$ and α is a tuning parameter which lies in the range $0 \leq \alpha \leq 1$. Note that for $\alpha = 0$, the result is the same as in the unfiltered case. Minimizing Equation 4.16 with respect to \mathbf{a} gives the filtered estimator

$$\hat{\mathbf{a}}_{(n,\alpha)} = \mathbf{M}_{(n,\alpha)}^{-1} \mathbf{\Psi}_{(n)}^\dagger \mathbf{W} \mathcal{N}_\gamma^{-1/2} \gamma^o \quad (4.17)$$

where we have defined $\mathbf{M}_{(n,\alpha)} \equiv [\mathbf{\Psi}_{(n)}^\dagger \mathbf{W} \mathbf{\Psi}_{(n)} + \alpha \mathbf{\Lambda}_{(n)}^{-1}]$, and $\mathbf{\Lambda}_{(n)}$ is the truncated diagonal matrix of eigenvalues associated with $\mathbf{\Psi}_{(n)}$.

4.3 Testing KL Reconstructions

In this section we show results of the KL analysis of shear fields for a sample geometry. In Section 4.3.1 we discuss the general properties of shear KL modes for unmasked fields, while in Section 4.3.2 we discuss KL shear reconstruction in the presence of masking.

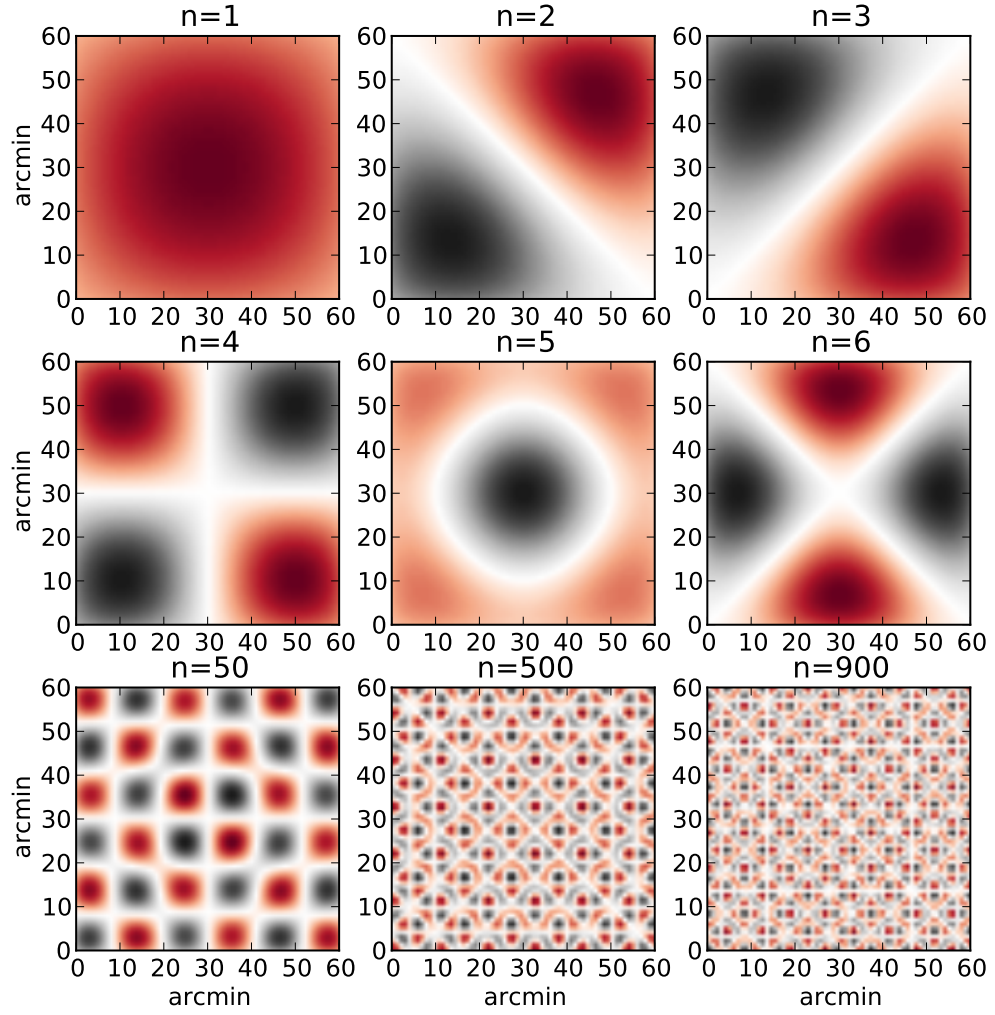


Figure 4.1: A sample of nine of the 4096 KL eigenmodes of a $1^\circ \times 1^\circ$ patch of the sky partitioned into 64×64 pixels. Black is positive, red is negative, and each mode has unit norm. The modes are calculated from the theoretical shear correlation function (see Section 4.2.3). As a consequence of the isotropy of the cosmic shear field, the covariance matrix – and thus the associated eigenmodes – are purely real (see Section 4.3.1).

4.3.1 *KL Decomposition of a Single Field*

To demonstrate the KL decomposition of a shear field, we assume a square field of size $1^\circ \times 1^\circ$, divided into 64×64 pixels. We assume a source galaxy density of 20 arcmin^{-2} – appropriate for a ground-based survey such as DES – and calculate the KL basis following the method outlined in Section 4.2.1. For the computation of the nonlinear matter power spectrum, we assume a flat Λ CDM cosmology with $\Omega_M = 0.27$ at the present day, with the power spectrum normalization given by $\sigma_8 = 0.81$.

Figure 4.1 shows a selection of nine of the 4096 shear eigenmodes within this framework. The KL modes are reminiscent of 2D Fourier modes, with higher-order modes probing progressively smaller length scales. This characteristic length scale of the eigenmodes can be seen quantitatively in Figure 4.2. Here we have computed the rotationally averaged power spectrum C_ℓ for each individual Fourier mode, and plotted the power vertically as a density plot for each mode number. Because the KL modes are not precisely equivalent to the 2D Fourier modes, each contains power at a range of values in ℓ . But the overall trend is clear: larger modes probe smaller length scales, and the modes are very close to Fourier in nature.

As noted in Section 4.2, one useful quality of a KL decomposition is its diagonalization of the signal and noise of the problem. To explore this property, we plot in the upper panel of Figure 4.3 the eigenvalue profile of these KL modes. By construction, higher-order modes have smaller KL eigenvalues. What is more, because the noise in the covariance matrix is whitened (see Section 4.2.2), the expectation of the noise covariance within each mode is equal to 1. Subtracting this noise from each eigenvalue gives the expectation value of the signal-to-noise ratio: thus we see that the expected signal-to-noise ratio of the eigenmodes is above unity only for the first 17 of the 4096 modes.

At first glance, this may seem to imply that only the first 17 or so modes are useful in a reconstruction. On the contrary: as seen in the lower panel of Figure 4.3, these first 17 modes contain only a small fraction of the total information in the shear field (This is not an unexpected result: cosmic shear measurements have notoriously low signal-to-noise ratios!) About 900 modes are needed to preserve an average of 70% of the total signal, and at this

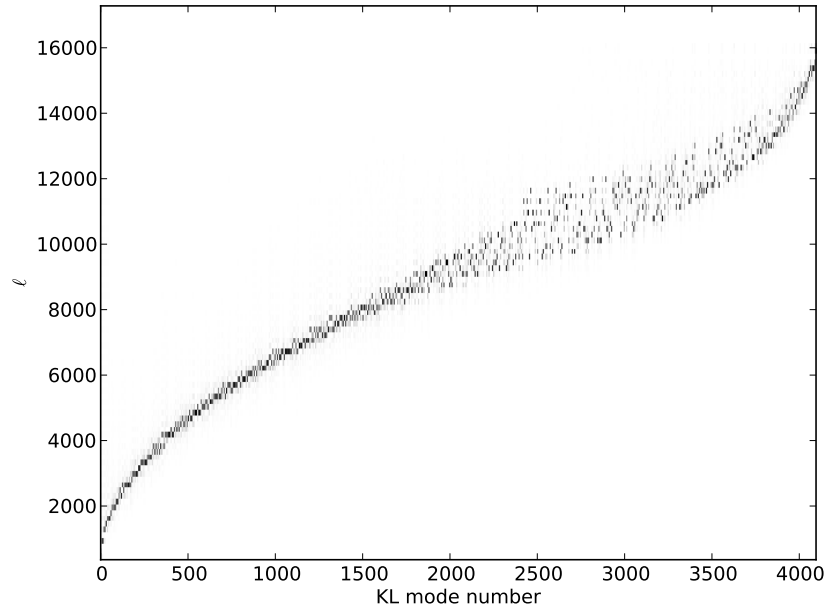


Figure 4.2: The normalized power spectrum of each KL mode. For constant mode number, the figure represents a histogram of the power in that KL mode, normalized to a constant total power. KL modes represent a linear combination of Fourier modes, so that the power in each KL mode is spread over a range of ℓ values. Nevertheless, the general trend is clear: larger mode numbers are associated with larger wave numbers, and thus smaller length scales.

level, each additional mode has a signal-to-noise ratio of below $1/10$. The noisy input shear field can be exactly recovered by using all 4096 modes: in this case, though, the final few modes contribute two orders-of-magnitude more noise than signal.

4.3.2 Testing KL Interpolation

To test this KL interpolation technique, we use simulated shear catalogs³. These catalogs contain 220 square degrees of simulated shear maps, computed using a ray-tracing grid through a cosmological N-body simulation of the standard Λ -CDM model. The shear signal is computed at the locations of background galaxies with a median redshift of about 0.7. Galaxies are incorporated in the simulation using the ADDGALS algorithm (Wechsler, 2004, Wechsler *et al.* in preparation), tuned to the expected observational characteristics of the DES mission.

We pixelize this shear field using the same pixel size as above: 64×64 pixels per square degree. To perform the KL procedure on the full field with this angular resolution would lead to a data vector containing over 10^6 elements, and an associated covariance matrix containing 10^{12} entries. A full eigenvalue decomposition of such a matrix is computationally infeasible, so we reconstruct the field in $1^\circ \times 1^\circ$ tiles, each 64×64 pixels in size. To reduce edge effects between these tiles, we use only the central $0.5^\circ \times 0.5^\circ$ region of each, so that covering the 300 square degree field requires 1200 tiles.

In order to generate a realistic mask over the field area, we follow the procedure outlined in Hikage et al. (2010) which generates pixel-level masks characteristic of point-sources, saturation spikes, and bad CCD regions. We tune the mask so that 20% of the shear pixels have no data. The geometry of the mask over a representative patch of the field can be seen in the lower panels of Figure 4.4, where we also show the result of the KL interpolation using 900 out of 4096 modes, with $\alpha = 0.15$ (For a discussion of these parameter choices, see Appendix C).

The upper panels of Figure 4.4 give a qualitative view of the difficulty of cosmic shear measurements. The top left panel shows the noiseless shear across the field, while the top

³The simulated shear catalogs were kindly made available to us by R. Wechsler, M. Busha, and M. Becker.

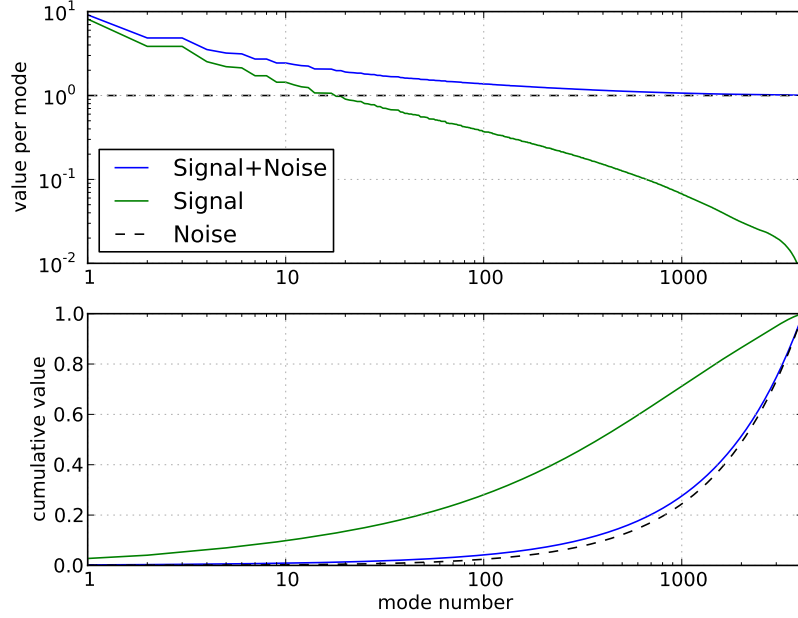


Figure 4.3: The eigenvalues associated with the eigenmodes discussed in Figure 4.1. By construction, the eigenvalue is proportional to the sum of signal and noise within each mode. The upper figure shows the value per mode, while the lower figure shows the normalized cumulative value. The stepped-pattern evident in the upper panel is due to the presence of degenerate eigenmodes which have identical eigenvalues (e.g. modes $n = 2$ and $n = 3$, related by parity as evident in Figure 4.1). Because the eigenmodes are computed from a whitened covariance matrix (see Section 4.2.2), the noise contribution within each mode is equal to 1. Subtracting this contribution leads to the plot of signal only: this shows that the signal-to-noise ratio is above unity only for the first 17 modes. Still, as seen in the lower panel, higher modes are required: the first 17 modes account for only 12% of the signal on average. To recover 70% of the signal in a particular reconstruction requires about 1000 modes. At this point, each additional mode has a signal-to-noise ratio of less than 0.1. Such a small signal-to-noise ratio is a well-known aspect of cosmic shear studies.

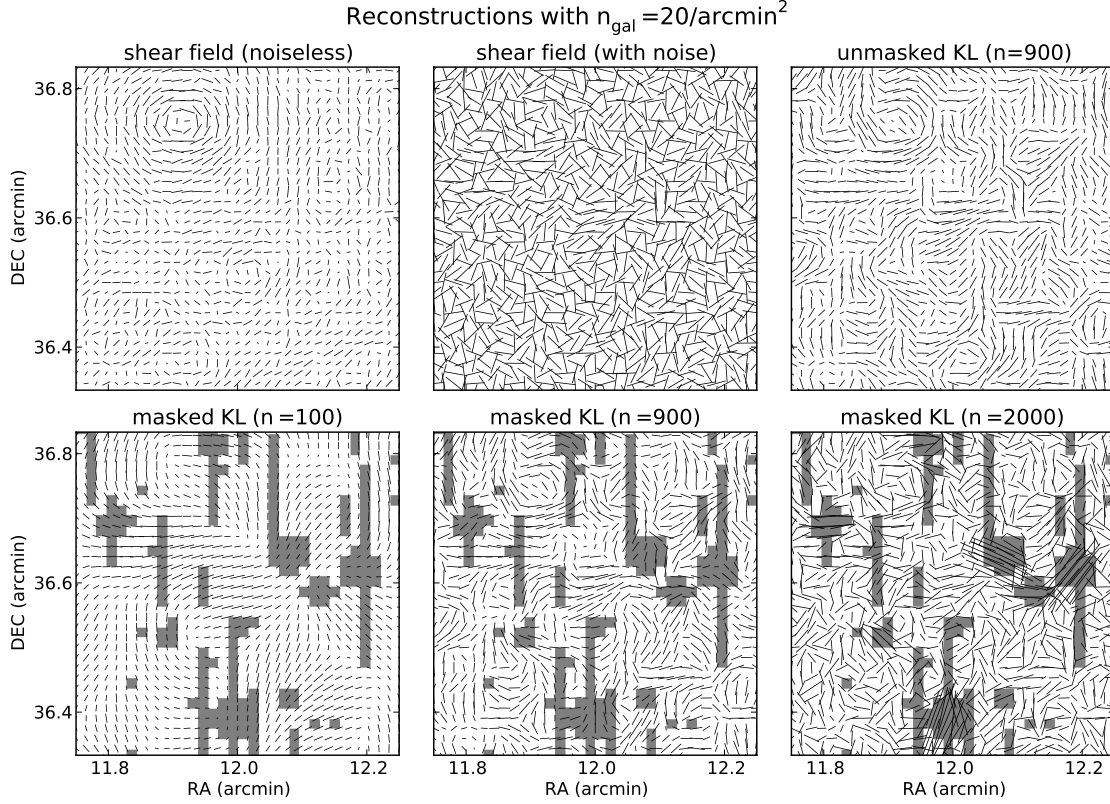


Figure 4.4: This figure illustrates the reconstruction of a small patch of masked shear from simulated shear catalog. *upper panels:* The underlying noiseless shear signal (*left*), the observed, noisy shear signal (*middle*), and the unmasked reconstruction with 900 modes and $\alpha = 0.15$. The amplitude of the noise is calculated using an intrinsic ellipticity $\sigma_\epsilon = 0.3$, with an average number density of $n_{\text{gal}} = 20 \text{ arcmin}^{-2}$. The large peak in the upper portion of the figure is well-recovered by the KL reconstruction. *lower panels:* The KL reconstruction of the shear in the presence of 20% masking, with increasing number of modes n . The mask is represented by the shaded regions in panels: within these regions, the value of the shear is recovered through KL interpolation (see Section 4.2.5). We see in this progression the effect of the KL cutoff choice: using too few modes leads to loss of information, while using too many modes leads to over-fitting within the masked regions (See Appendix C for a discussion of the choice of number of modes).

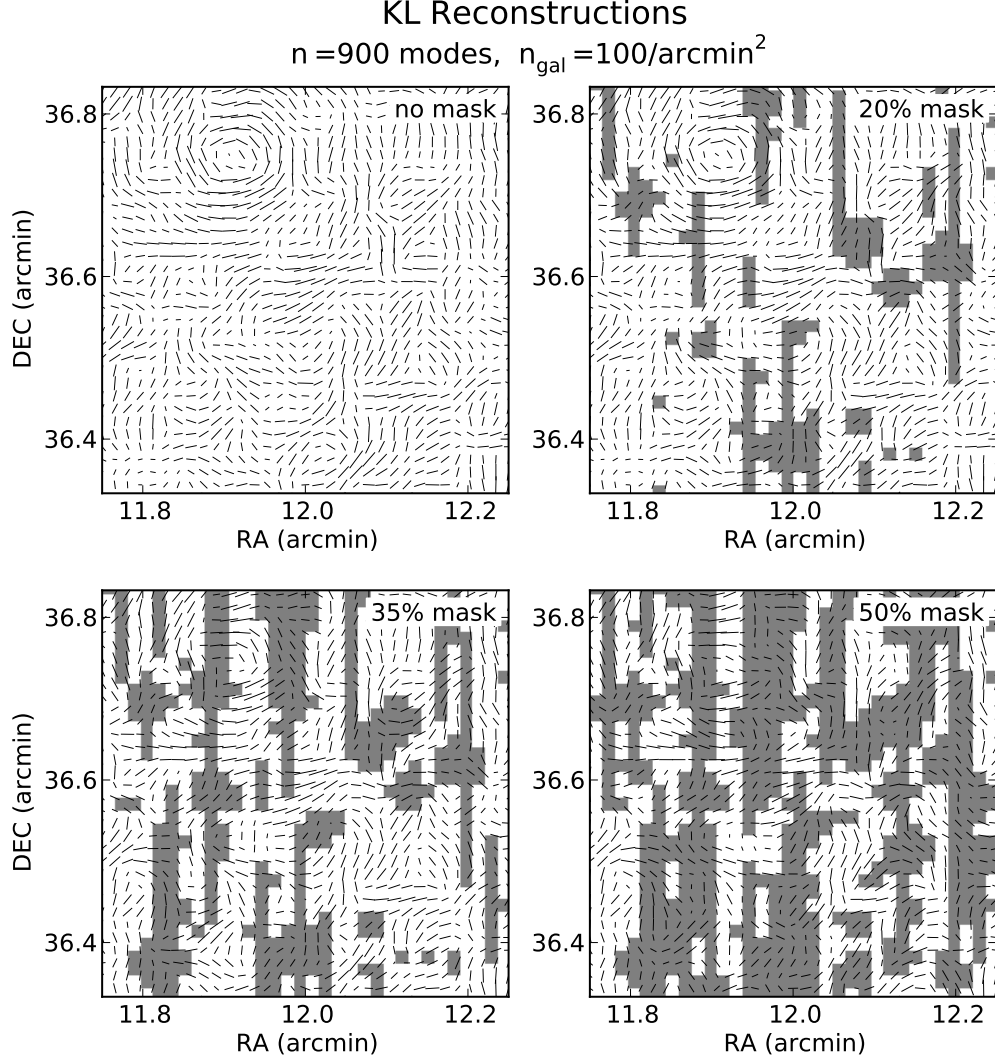


Figure 4.5: Here we show the same field as in Figure 4.4, reconstructed using $n = 900$ modes, with increasing levels of mask coverage. The density of source galaxies has been increased to 100 arcmin^{-2} , typical of a space-based weak lensing survey. At this noise level, smaller halos can be detected within the unmasked KL reconstruction (upper-left panel). Even at a 50% masking level, the large peak at $(\text{RA}, \text{DEC}) = (11.9, 36.75)$ is adequately recovered.

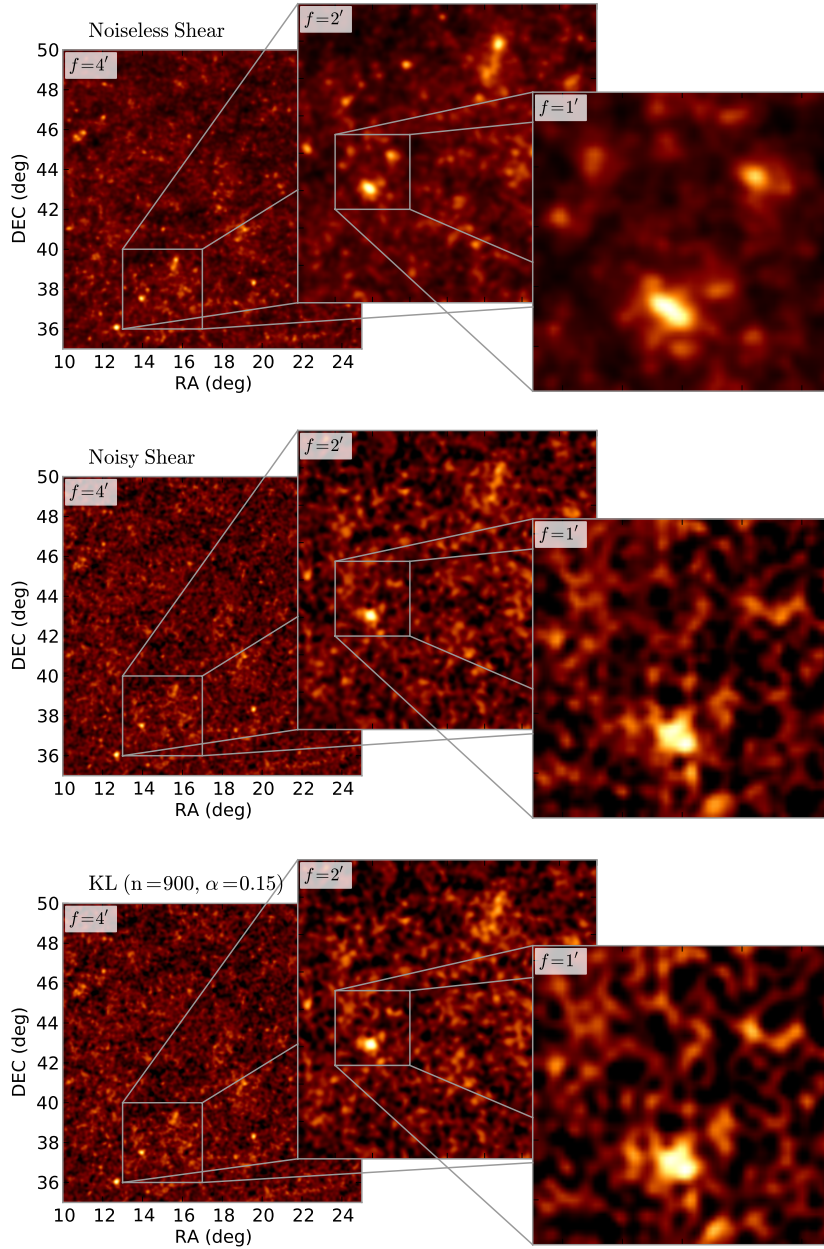


Figure 4.6: The large-field convergence map derived using the method of Kaiser & Squires (1993) from the noiseless input shear (*upper panels*), the noisy input shear (*middle panels*), and the 900-mode, $\alpha = 0.15$ reconstruction of the noisy shear, with 20% of pixels masked out (*lower panels*). The rightmost plots of each row cover one square degree. The larger-field maps are smoothed with Gaussian filters of width 4 and 2 arcmin, while the smaller fields are unsmoothed. These plots show that even with 20% masking of the input signal, the KL interpolation procedure recovers the most significant peaks, and offers improvement over the results derived from unmasked, observed shear. This improvement will be discussed more quantitatively below.

right panel shows the shear with shape noise for a DES-type survey ($\sigma_\epsilon = 0.3$, $\bar{n}_{gal} = 20 \text{ arcmin}^{-2}$). To the eye, the signal seems entirely washed out by the noise. Nevertheless, the shear signal is there, and can be fairly well-recovered using the first 900 KL modes (middle-left panel). For masked data, we must resort to the techniques of Section 4.2.5 to fill-in the missing data. The middle-right panel shows this reconstruction, with gray shaded regions representing the masked area. A visual comparison of the masked and unmasked $n = 900$ panels of Figure 4.4 confirms qualitatively that the KL interpolation is performing as desired. This is especially apparent near the large cluster located at (RA,DEC)=(11.9,36.7). The remaining two lower panels of Figure 4.4 show cases of over-fitting and under-fitting of the shear data. If too few KL modes are used, the structure of the input shear field is lost. If too many KL modes are used, the masked regions are over-fit, causing the interpolated shear values to become unnaturally large. This observation suggests one rubric by which the ideal number of modes can be chosen; see the discussion in Appendix C.

It is interesting to explore the limits of this interpolation algorithm. Figure 4.5 shows the KL reconstruction with increasing masked fractions, using a noise level typical of space-based lensing surveys ($n_{gal} = 100 \text{ arcmin}^{-2}$). Though the quality of the reconstruction understandably degrades, the lower panels show that large features can be recovered even with up to 50% of the pixels masked.

In Figure 4.6 we provide a comparison of the convergence maps generated from the noiseless shear (upper panels) and the KL-reconstructed noisy shear with 20% of pixels masked (lower panels). The convergence maps are smoothed by a Gaussian filter to ease comparison with the quantitative results of Sections 4.4-4.5, where we explore the distribution of peaks through an aperture mass filter. The aperture mass filter amounts to a particular smoothing function over the convergence field (see Section 4.4.1, below). Comparison of the upper and lower panels of Figure 4.6 give a qualitative indication of the performance of KL: high-convergence regions are recovered remarkably well, while convergence peaks of lower magnitude are obscured by the background noise: as we show in the following sections, this obscuration is largely the result of shape noise in the simulated shear measurements.

For a quantitative analysis of the effectiveness of the KL interpolation in convergence mapping, and the potential biases it introduces, a large-scale statistical measure is most

appropriate. In the following sections, we test the utility of this KL interpolation scheme within the framework of shear peak statistics.

4.4 *Shear Peak Statistics*

It has long been recognized that much useful cosmological information can be deduced from the masses and spatial distribution of galaxy clusters (e.g. Press & Schechter, 1974). Galaxy clusters are the largest gravitationally bound objects in the universe, and as such are exponentially sensitive to cosmological parameters (White et al., 1993). The spatial distribution of clusters and redshift evolution of their abundance and clustering is sensitive to both geometrical effects of cosmology, as well as growth of structure. Because of this, cluster catalogs can be used to derive constraints on many interesting cosmological quantities, including the matter density Ω_M and power spectrum normalization σ_8 (Lin et al., 2003), the density and possible evolution of dark energy (Linder & Jenkins, 2003; Vikhlinin et al., 2009), primordial non-gaussianities (Matarrese et al., 2000; Grossi et al., 2007), and the baryon mass fraction (Lin et al., 2003; Giodini et al., 2009).

Various methods have been developed to measure the mass and spatial distribution of galaxy clusters, and each are subject to their own difficult astrophysical and observational biases. They fall into four broad categories: optical or infrared richness, X-ray luminosity and surface brightness, Sunyaev-Zeldovich decrement, and weak lensing shear.

While it was long thought that weak gravitational lensing studies would lead to robust, purely mass-selected cluster surveys, it has since become clear that shape noise and projection effects limit the usefulness of weak lensing in determining the 3D cluster mass function (Hamana et al., 2004; Hennawi & Spergel, 2005; Mandelbaum et al., 2010; VanderPlas et al., 2011). The shear observed in weak lensing is non-locally related to the convergence, a measure of *projected* mass along the line of sight. The difficulty in deconvolving the correlated and uncorrelated projections in this quantity leads to difficulties in relating these projected peak heights to the masses of the underlying clusters in three dimensions. Recent work has shown, however, that this difficulty in relating the observed quantity to theory may be overcome through the use of statistics of the projected density itself.

Marian et al. (2009, 2010) first explored the extent to which 2D projections of the 3D

mass field trace cosmology. They found, rather surprisingly, that the statistics of the projected peaks closely trace the statistics of the 3D peak distribution: in N-body simulations, both scale with the Sheth & Tormen (1999) analytic scaling relations. The same correlated projections which bias cluster mass estimates contribute to a usable signal: statistics of projected mass alone can provide useful cosmological constraints, without the need for bias-prone conversions from peak height to cluster mass.

A host of other work has explored diverse aspects of these shear peak statistics, including tests of these methods with ensembles of N-body simulations (Wang et al., 2009; Kratochvil et al., 2010; Dietrich & Hartlap, 2010), the performance of various filtering functions and peak detection statistics (Pires et al., 2009; Schmidt & Rozo, 2010; Kratochvil et al., 2011), exploration of the spatial correlation of noise with signal within convergence maps (Fan et al., 2010), and exploration of shear-peak constraints on primordial non-gaussianity (Maturi et al., 2011). The literature has yet to converge on the ideal mapping procedure: convergence maps, Gaussian filters, various matched filters, wavelet transforms, and more novel filters are explored within the above references. There is also variation in how a “peak” is defined: simple local maxima, “up-crossing” criteria, fractional areas above a certain threshold, connected-component labeling, hierarchical methods, and Minkowski functionals are all shown to be useful. Despite diverse methodologies, all the above work confirms that there is useful cosmological information within the projected peak distribution of cosmic shear fields, and that this information adds to that obtained from 2-point statistics alone.

4.4.1 Aperture Mass Peaks

Based on this consensus, we use shear peak statistics to explore the possible bias induced by the KL interpolation method outlined above. We follow the aperture mass methodology of Dietrich & Hartlap (2010): The aperture mass magnitude at a point $\vec{\theta}_0$ is given by

$$M_{\text{ap}}(\vec{\theta}_0) = \int_{\Omega} d^2\theta Q_{\text{NFW}}(\vartheta = |\vec{\theta} - \vec{\theta}_0|) \gamma_t(\vec{\theta}; \vec{\theta}_0) \quad (4.18)$$

where $\gamma_t(\vec{\theta}; \vec{\theta}_0)$ is the component of the shear at location $\vec{\theta}$ tangential to the line $\vec{\theta} - \vec{\theta}_0$, and Q_{NFW} is the NFW-matched filter function defined in Schirmer et al. (2007):

$$Q_{\text{NFW}}(x; x_c) \propto \frac{1}{1 + e^{6-150x} + e^{-47+50x}} \frac{\tanh(x/x_c)}{x/x_c} \quad (4.19)$$

with $x = \vartheta/\vartheta_{\text{max}}$ and x_c a free parameter. We follow Dietrich & Hartlap (2010) and set $\vartheta_{\text{max}} = 5.6$ arcmin and $x_c = 0.15$. The integral in Equation 4.18 is over the whole sky, though the filter function Q effectively cuts this off at a radius ϑ_{max} . In the case of our pixelized shear field, the integral is converted to a discrete sum over all pixels, with ϑ equal to the distance between the pixel centers:

$$M_{\text{ap}}(\vec{\theta}_i) = \sum_j Q_{\text{NFW}}(\vartheta_{ij}) \gamma_t(\vec{\theta}_i; \vec{\theta}_j) \quad (4.20)$$

where we have defined $\vartheta_{ij} \equiv |\vec{\theta}_i - \vec{\theta}_j|$.

We can similarly compute the *B-mode* aperture mass, by substituting $\gamma_t \rightarrow \gamma_{\times}$ in Equations 4.18-4.20 (Crittenden et al., 2002). For pure gravitational weak lensing with an unbiased shear estimator, the B-mode signal is expected to be negligible, though second-order effects such as source clustering and intrinsic alignments can cause contamination on small angular scales (Crittenden et al., 2002; Schneider et al., 2002b). These effects aside, the B-mode signal can be used as a rough estimate of the systematic bias of a particular analysis method.

For our study, the aperture mass is calculated with the same resolution as the shear pixelization: 64^2 pixels per square degree. A pixel is defined to be a peak if its value is larger than that of the surrounding eight pixels: a simple local maximum criterion.

4.4.2 The Effects of Masking

When a shear peak statistic is computed across a field with masked regions, the masking leads to a bias in the peak height distribution (see Section 4.5 below). Moreover, due to the non-local form of the aperture mass statistic, a very large region is affected: in our case, a single masked pixel biases the aperture mass measurement of an area of size $\pi(2\vartheta_{\text{max}})^2 \approx 400$ arcmin². There are two naïve approaches one could use when measuring the aperture mass in this situation:

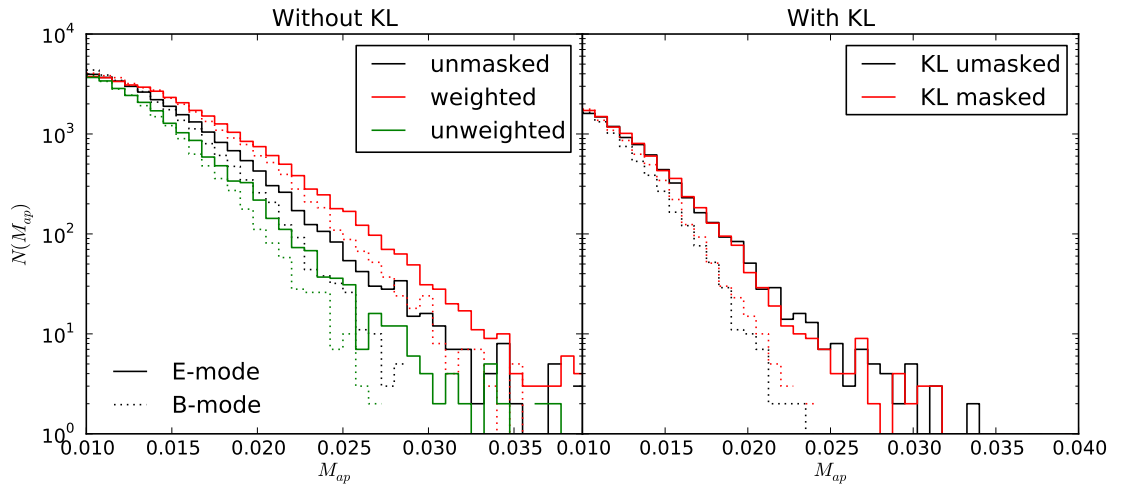


Figure 4.7: Comparison of the masked and unmasked peak distributions. *left panel:* the peak distributions without the use of KL. The black line is the result with no masking, while the red and green lines show the two naïve methods of correcting for the mask (see Section 4.4.2). *right panel:* the masked and unmasked peak distributions after applying KL. Neither naïve method of mask-correction adequately recovers the underlying peak distribution. It is evident, however, that the KL-based interpolation procedure recovers a mass map with a similar peak distribution to the unmasked KL map. It should be noted that the unmasked peak distribution (black line, left panel) is not identical to the unmasked peak distribution after application of KL (black line, right panel). This difference is addressed in Figure 4.8.

Unweighted: Here we simply set the shear value within each masked pixel to zero, and apply Equation 4.20. The shear within the masked regions do not contribute to the peaks, so the height of the peaks will be underestimated.

Weighted: Here we implement a weighting scheme which re-normalizes the filter Q_{NFW} to reflect the reduced contribution from masked pixels. The integral in equation 4.18 is replaced by the normalized sum:

$$M_{\text{ap}}(\vec{\theta}_i) = \frac{\sum_j Q_{\text{NFW}}(\vartheta_{ij}) \gamma_t(\vec{\theta}_j) w(\vec{\theta}_j)}{\sum_j Q_{\text{NFW}}(\vartheta_{ij}) w(\vec{\theta}_j)} \quad (4.21)$$

where $w(\vec{\theta}_j) = 0$ if the pixel is masked, and 1 otherwise. This should correct for the underestimation of peak heights seen in the unweighted case.

In order to facilitate comparison between this weighted definition of M_{ap} and the normal definition used in the unmasked and unweighted cases, we normalize the latter by $\sum_j Q_{\text{NFW}}(\vec{\theta}_{ij})$, which is a constant normalization across the field.

Note that in both cases, it is the *shear* that is masked, not the M_{ap} peaks. Aperture mass is a non-local measure, so that the value can be recovered even within the masked region. This means that masking will have a greater effect on the observed magnitude of the peaks than it will have on the count. In particular, on the small end of the peak distribution, where the peaks are dominated by shape noise, the masking of the shear signal is likely to have little effect on the distribution of peak counts. This can be seen in Figure 4.8.

4.4.3 M_{ap} Signal-to-Noise

It is common in shear peak studies to study signal-to-noise peaks rather than directly study aperture-mass or convergence peaks (e.g. Wang et al., 2009; Dietrich & Hartlap, 2010; Schmidt & Rozo, 2010). We follow this precedent here. The aperture mass (Eqn. 4.20) is defined in terms of the tangential shear. Because we assume that the shear measurement is dominated by isotropic, uncorrelated shape noise, the noise covariance of M_{ap} can be expressed

$$[\mathcal{N}_M]_{ij} \equiv \langle M_{\text{ap}}(\vec{\theta}_i) M_{\text{ap}}(\vec{\theta}_j) \rangle$$

$$= \frac{1}{2} \sum_k Q_{\text{NFW}}^2(\vartheta_{ik}) [\mathcal{N}_\gamma]_{kk} \delta_{ij} \quad (4.22)$$

where we have used the fact that shape noise is uncorrelated: $[\mathcal{N}_\gamma]_{ij} = \langle n_i n_j \rangle \propto \delta_{ij}$.

In the case of a KL-reconstruction of a masked shear field, the reconstructed shear has non-negligible correlation of noise between pixels. From Equations 4.15-4.17, it can be shown that

$$\begin{aligned} \mathcal{N}_{\hat{\gamma}} &\equiv \langle \hat{\gamma} \hat{\gamma}^\dagger \rangle \\ &= \left[\mathcal{N}_\gamma^{1/2} \Psi M^{-1} \Psi^\dagger \right] W^2 \left[\Psi M^{-1} \Psi^\dagger \mathcal{N}_\gamma^{1/2} \right] \end{aligned} \quad (4.23)$$

The covariance matrix $\mathcal{N}_{\hat{\gamma}}$ is no longer diagonal, but the noise remains isotropic under the linear transformation, so that $\mathcal{N}_{\hat{\gamma}_t} = \mathcal{N}_{\hat{\gamma}}/2$. The aperture mass noise covariance can thus be calculated in a similar way to the non-KL case:

$$[\mathcal{N}_M]_{ij} = \frac{1}{2} \sum_k \sum_\ell Q_{\text{NFW}}(\vartheta_{ik}) Q_{\text{NFW}}(\vartheta_{j\ell}) [\mathcal{N}_{\hat{\gamma}}]_{k\ell}. \quad (4.24)$$

This expression can be computed through standard linear algebraic techniques. The aperture mass signal-to-noise in each pixel is given by

$$[S/N]_i = M_{\text{ap}}(\vec{\theta}_i) / \sqrt{[\mathcal{N}_M]_{ii}} \quad (4.25)$$

4.5 Discussion

4.5.1 M_{ap} Peak Distributions

In Figures 4.7-4.10 we compare the peak distribution obtained with and without KL. We make three broad qualitative observations which point to the efficacy of KL in interpolation of masked shear fields, and in the filtration of shape-noise from these fields. We stress the qualitative nature of these results: quantifying these observations in a statistically rigorous way would require shear fields from an ensemble of cosmology simulations, which is beyond the scope of this work. These results nevertheless point to the efficacy of KL analysis in this context.

KL filtration corrects for the bias due to masking. Figure 4.7 compares the effect of masking on the resulting peak distributions with and without KL. The left panel shows

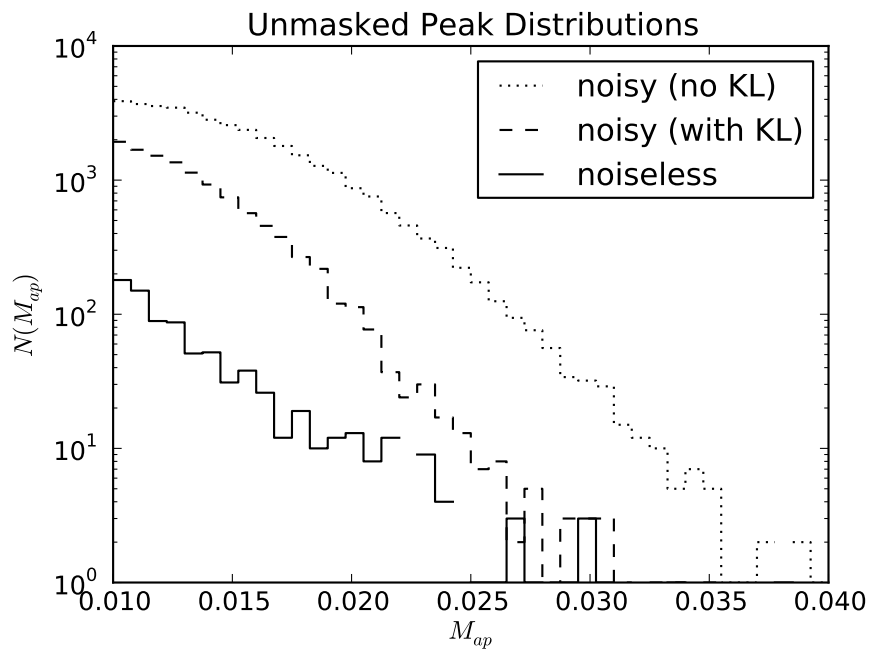


Figure 4.8: Comparison of the distribution of M_{ap} peaks for unmasked shear, before and after filtering the field with KL (dotted line and dashed line, respectively). The peak distribution in the absence of noise is shown for comparison (solid line). It is clear that the addition of shape noise leads to many spurious M_{ap} peaks: noise peaks outnumber true peaks by nearly a factor of 10 for smaller peak heights. Filtering by KL reduces these spurious peaks by about a factor of 3, and for larger peaks leads to a distribution similar in scale to that of the noiseless peaks.

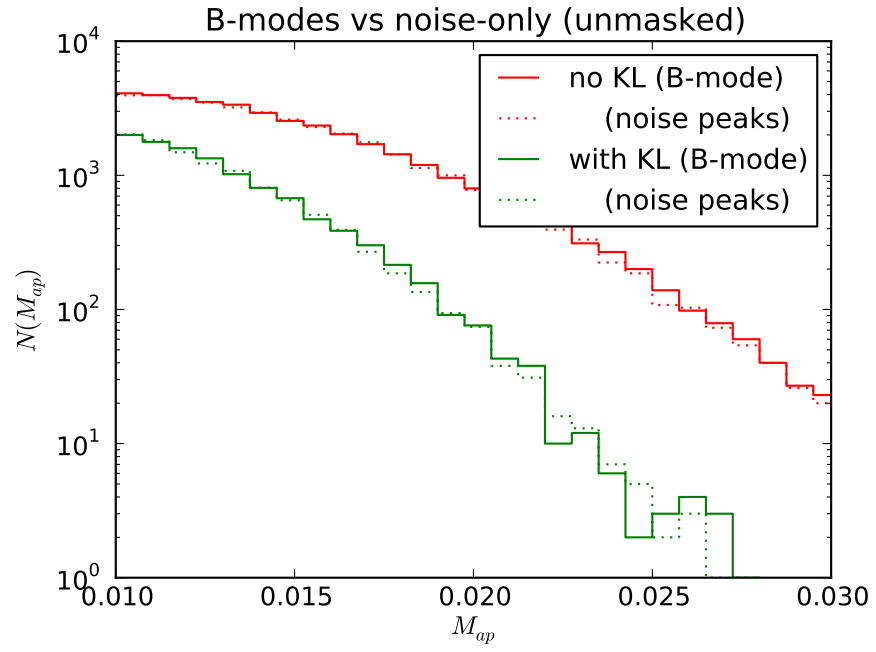


Figure 4.9: The comparison between B-mode peak distributions and the peak distributions for a shear field composed entirely of noise. As expected, the B-mode peak distributions are largely consistent with being due to noise only. Because of this, we can use B-mode peaks as a rough proxy for the noise.

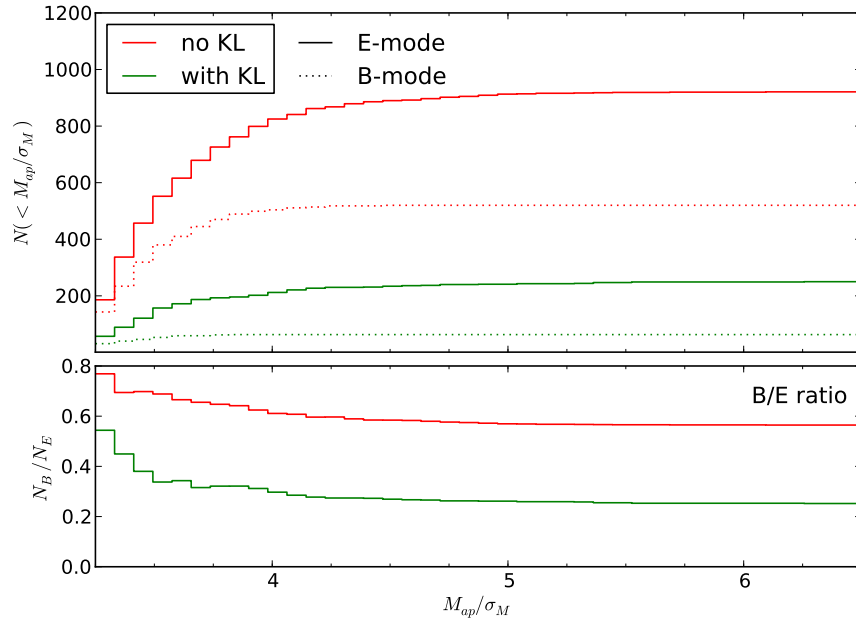


Figure 4.10: *top panel:* The cumulative distributions of peaks in signal-to-noise, for peaks with $M_{\text{ap}}/\sigma_M > 3.25$. This is the statistic used by Dietrich & Hartlap (2010) to discriminate between cosmological models. *bottom panel:* The ratio of B-mode to E-mode peak distributions. Filtration by KL reduces the relative number of B-mode peaks by about 1/3. Because B-mode peaks are a proxy for contamination by shape noise (see Figure 4.9), this indicates that KL-filtration results in peak distributions less affected by statistical errors. KL also reduces the total number of both E and B peaks by about 2/3; this effect can also be seen in Figure 4.8.

the unmasked noisy peak distribution, and the masked peak distributions resulting from the weighted and unweighted approaches described in Section 4.4.2. Neither method of accounting for the masking accurately recovers the unmasked distribution of peak heights. The unweighted approach (green line) leads to an underestimation of peak heights. This is to be expected, because it does not correct for the missing information in the masked pixels. The weighted approach, on the other hand, over-estimates the counts of the peaks. We suspect this is due to an analog of Eddington bias: the lower signal-to-noise ratio of the weighted peak statistic leads to a larger scatter in peak heights. Because of the steep slope of the peak distribution, this scatter preferentially increases the counts of larger peaks. This suspicion is confirmed by artificially increasing the noise in the unmasked peak function. Increasing σ_ϵ from 0.30 to 0.35 in the unmasked case results in a nearly identical peak function to the weighted masked case.

The right panel of Figure 4.7 shows that when KL is applied to the shear field, the distribution of the masked and unmasked peaks is very close, both for E-mode and B-mode peaks. This indicates the success of the KL-based interpolation outlined in Section 4.2.5. Even with 20% of the pixels masked, the procedure can recover a nearly identical peak distribution as from unmasked shear.

KL filtration reduces the number of noise peaks. Comparison of the unmasked lines in the left and right panels of Figure 4.7 shows that application of KL to a shear field results in fewer peaks at all heights. This is to be expected: when a reconstruction is performed with fewer than the total number of KL modes, information of high spatial frequency is lost. In this way, KL acts as a sort of low-pass filter tuned to the particular signal-to-noise characteristics of the data. Figure 4.8 over-plots the KL and non-KL peak distributions with the noiseless peak distribution. From this figure we see that the inclusion of shape noise results in nearly an order-of-magnitude more peaks than the noiseless case. The effect of noise on peak counts lessens slightly for higher- M_{ap} peaks: this supports the decision of Dietrich & Hartlap (2010) to limit their distributions to peaks with a signal-to-noise ratio greater than 3.25: the vast majority of peaks are lower magnitude, and are overwhelmed by the effect of shape noise.

Omission of higher-order KL modes of shear field reduces the number of these spurious

peaks by a factor of 3 or more. For low-magnitude peaks, ($M_{\text{ap}} < \sim 0.02$), KL still produces peak counts which are dominated by noise. For higher-magnitude peaks, the number of observed KL peaks more closely approaches the number of peaks in the noiseless case.

KL filtration reduces the presence of B-modes. To first order, weak lensing shear is expected to consist primarily of curl-free, E-mode signal. Because of this, the presence of B-modes can indicate a systematic effect. It is not obvious that filtration by KL will maintain this property: as noted in Section 4.2.4, KL modes individually are agnostic to E-mode and B-mode information. E&B information is only recovered within a complex-valued linear combination of the set KL modes.

Figure 4.9 shows a comparison between the unmasked B-mode peak functions from Figure 4.7 and the associated E-mode peak functions due to shape-noise only. For both the non-KL version and the KL version, the B-mode peak distributions closely follow the distributions of noise peaks. This supports the use of B-mode peaks as a proxy for the peaks due to shape noise, even when truncating higher-order KL modes.

The near-equivalence of B-modes and noise-only peaks shown in Figure 4.9 suggests a way of recovering the true peak function, by subtracting the B-mode count from the E-mode count as a proxy for the shape noise. This approach has one fatal flaw: because it involves computing the small difference between two large quantities, the result has extremely large uncertainties. It should be noted that this noise contamination of small peaks is not an impediment to using this method for cosmological analyses: the primary information in shear peak statistics is due to the high signal-to-noise peaks.

In the top panel of Figure 4.10, we show the cumulative distribution of peaks in signal-to-noise, for peaks with $S/N > 3.25$: the quantity used as a cosmological discriminant in Dietrich & Hartlap (2010). The difference in the total number of E-mode peaks in the KL and non-KL approaches echoes the result seen in Figure 4.8: truncation of higher-order KL modes acts as a low-pass filter, reducing the total number of peaks by a factor of ~ 3 . More interesting is the result shown in the lower panel of Figure 4.10, where the ratio of B-mode peak counts to E-mode peak counts is shown. Before application of KL, the B-mode contamination is above 30%. Filtration by KL reduces this contamination by a factor of ~ 3 , to about 10%. This indicates that the truncation of higher-order KL modes leads to

a preferential reduction of the B-mode signal, which traces the noise. This is a promising observation: the counts of high signal-to-noise peaks, which offer the most sensitivity to cosmological parameters (Dietrich & Hartlap, 2010), are significantly less contaminated by noise after filtering and reconstruction with KL. This is a strong indication that the use of KL could improve the cosmological constraints derived from studies of shear peak statistics.

Note that in Figure 4.10 we omit the masked results for clarity. The masked cumulative signal-to-noise peak functions have B/E ratios comparable to the unmasked versions, so the conclusions here hold in both the masked and unmasked cases.

4.5.2 *Remaining Questions*

The above discussion suggests that KL analysis of masked shear fields holds promise in constraining cosmological parameters of shear peaks in both masked and unmasked fields. KL greatly reduces the number of spurious noise peaks at all signal-to-noise levels. It minimizes the bias between masked and unmasked constructions, and leads to a factor of 3 suppression of the B-mode signal, which is a proxy for the spurious signal introduced through shape noise.

The question remains, however, how much cosmological information is contained in the KL peak functions. The reduction in level of noise peaks is promising, but the omission of higher-order modes in the KL reconstruction leads to a smoothing of the shear field on scales smaller than the cutoff mode. This smoothing could lead to the loss of cosmologically useful information. In this way, the choice of KL mode cutoff can be thought of as a balance between statistical and systematic error. The effect of these competing properties on cosmological parameter determination is difficult to estimate. Quantifying this effect will require analysis within a suite of synthetic shear maps, similar to the approach taken in previous studies (e.g. Dietrich & Hartlap, 2010; Kratochvil et al., 2010), and will be the subject of future work.

Another possible application of KL in weak lensing is to use KL to directly constrain 2-point information in the measured shear data. In contrast to the method outlined in the current work, KL basis functions can be computed for the unmasked region only. The

projection of observed data onto this basis can be used to directly compute cosmological parameters via the 2-point function, without ever explicitly calculating the power spectrum. This is similar to the approach taken for galaxy counts in Vogeley & Szalay (1996). This approach is the subject of Chapter 5.

Chapter 5

APPLICATION TO COSMOS LENSING DATA

This chapter will cover the application of KL parameter estimation to lensing data from the COSMOS survey, a ~ 1.5 square degree field observed by the Hubble Space Telescope. We use KL to express the data within the optimal orthonormal basis dictated by the survey geometry, and use the Bayesian inference framework developed in §2.4 to perform a simple parameter estimation using the KL basis in place of the usual Fourier basis. From this, we obtain parameter constraints on Ω_M and σ_8 which are similar to those from conventional angular correlation analyses, with a framework that is free from the systematic errors associated with incomplete sky coverage and irregular survey geometry.

This chapter represents a first exploration of this problem; the results consider a simple two dimensional analysis for two cosmological parameters. KL can naturally be extended to 3D tomographic approaches with any number of parameters; this will be the subject of future work.

5.1 Introduction

In this chapter we explore the evaluation of cosmological likelihoods using KL analysis of shear fields. In Chapter 4 we explored the use of KL analysis in shear surveys, focusing on the ability of KL modes to help fill-in missing information within the context of weak lensing convergence mapping and studies of the peak statistics of the resulting mass maps. Here we follow a different approach: we use KL analysis to aid in the calculation of cosmological likelihoods using two-point statistics within a Bayesian framework. This draws upon similar work done previously to constrain cosmological parameters using number counts of galaxy surveys (Vogeley & Szalay, 1996; Pope et al., 2004).

In §5.2 we review and discuss the strengths and weaknesses of constraining cosmological quantities using two-point shear statistics. In §5.3 we review KL analysis and its application

to shear surveys. In §5.4 we describe the COSMOS shear data used in this analysis, and we discuss these results in §5.5.

5.2 Two-point Statistics in Weak Lensing

As noted and outlined in Chapter 1, the large-scale structure of the Universe provides a powerful probe of cosmological parameters. Through gravitational instability, the initial matter fluctuations have grown to the nonlinear structure we see today. This happens in a hierarchical manner, with the smallest structures collapsing before the largest. One of the most powerful probes of this structure is the redshift-dependent power spectrum of matter density fluctuations, $P_k(z)$, which gives the amplitude of the Fourier mode with wave-number k at a redshift z . This approach has often been used to measure cosmological parameters through optical tracers of the underlying dark matter structure (e.g. Tegmark et al., 2006). In this chapter we explore the use of weak lensing measurements of the matter power spectrum. Recent work has shown the power of this lensing-based approach (Ichiki et al., 2009; Schrabback et al., 2010).

There are two approaches to measuring two-point information that are mathematically equivalent: the power spectrum $\mathcal{P}(\ell)$, and its Fourier transform $\xi(\theta)$. In practice, the most commonly used method of measuring two-point information is through correlation functions (see Schneider et al., 2002a). The main advantage of correlation functions is their ease of measurement: they can be straightforwardly estimated from the positions and shapes of galaxies, even in very complicated survey geometries. Their disadvantage is that the signal is highly correlated between different scales. Accounting for this correlation is very important when computing cosmological likelihoods, and often requires large suites of simulations.

Shear power spectra, on the other hand, have a number of nice properties. Compared to correlation functions, they provide a simpler mapping to theoretical expectations. They have weaker correlations between different multipoles: on the largest scales, where structure is close to Gaussian, the scales are expected to be statistically independent. Even on small scales where non-Gaussianity leads to correlated errors, these correlations have a relatively small effect on derived cosmological constraints (Takada & Jain, 2009). The disadvantage of shear power spectra as direct cosmological probes is the difficulty of measuring them from

data. In particular, survey geometry effects such as incomplete sky coverage and masking can lead to mixing of power on all angular scales. This mode-mixing is a direct result of the loss of orthogonality: spherical harmonics are orthogonal over the entire sky, but are not necessarily orthogonal over the incomplete patch of the sky represented by lensing surveys. Even in the case of future all-sky surveys, the masking from foreground sources will pose a problem. This means that the spherical harmonic decomposition on which power spectra are based is not unique for realistic surveys. It may be possible to construct a survey in order to limit the magnitude of these effects (see Kilbinger & Schneider, 2004; Kilbinger & Munshi, 2006, for some approaches). There have also been a few attempts to correct for this difficulty through direct deconvolution of the survey geometry from the correlation signal (Brown et al., 2003; Hikage et al., 2011), but because of the computational difficulty involved with these methods, results based on correlation function measures remain more common. Here we explore an alternate approach which relies on constructing a new set of orthogonal modes for the observed survey geometry. Because the new modes are orthogonal by construction, one can avoid the difficulties associated with mode mixing. We propose to take this latter approach using Karhunen-Lo  ve (KL) analysis.

5.3 *KL for Parameter Estimation*

As discussed more fully in Chapter 2, KL analysis and the related Principal Component Analysis are well-known statistical tools which have been applied in a wide variety of astrophysical situations, from e.g. analysis of the spatial power of galaxy counts (Vogeley & Szalay, 1996; Szalay et al., 2003; Pope et al., 2004) to characterization of stellar, galaxy, and QSO spectra (Connolly et al., 1995; Connolly & Szalay, 1999; Yip et al., 2004a,b), to studies of noise properties of weak lensing surveys (Kilbinger & Munshi, 2006; Munshi & Kilbinger, 2006), and a host of other situations too numerous to mention here. Informally, the power of KL/PCA rests in the fact that it allows a highly efficient representation of a set of data, highlighting the components that are most important in the dataset as a whole. Though the framework is discussed more completely in Chapter 2, we will review the most important points here. The discussion of KL analysis below derives largely from Vogeley & Szalay (1996), reexpressed for application in cosmic shear surveys.

Any D -dimensional data point may be completely represented as a linear combination of D orthogonal basis functions: this is a geometrical property, closely linked to the free choice of coordinate axes used to represent points in a D -dimensional space. For example, the data may be N individual galaxy spectra, each with flux measurements in D wavelength bins. Each spectrum can be thought of as a single point in D -dimensional parameter space, where each axis corresponds to the value within a single wavelength bin. Geometrically, there is nothing special about this choice of axes: one could just as easily rotate and translate the axes to obtain a different but equivalent representation of the same data.

In the case of a shear survey, our single data vector is the set of cosmic shear measurements across the sky. We will divide the sky into N cells in angular and redshift space, at coordinates $\mathbf{x}_i = (\theta_{x,i}, \theta_{y,i}, z_i)$. These cells may be spatially distinct, or they may overlap. From the ellipticity of the galaxies within each cell, we estimate the shear $\gamma_i \equiv \gamma^o(\mathbf{x}_i) = \gamma(\mathbf{x}_i) + n_\gamma(\mathbf{x}_i)$ where $\gamma(\mathbf{x}_i)$ is the true underlying shear, and $n_\gamma(\mathbf{x}_i)$ is the measurement noise. Our data vector is then $\boldsymbol{\gamma} = [\gamma_1, \gamma_2 \cdots \gamma_N]^T$.

We seek to express our set of measurements $\boldsymbol{\gamma}$ as a linear combination of N (possibly complex) orthonormal basis vectors $\{\boldsymbol{\Psi}_j(\mathbf{x}_i, j = 1, N)\}$ with complex coefficients a_j :

$$\gamma_i = \sum_{j=1}^N a_j \Psi_j(\mathbf{x}_i) \quad (5.1)$$

For conciseness, we'll create the matrix $\boldsymbol{\Psi}$ whose columns are the basis vectors $\boldsymbol{\Psi}_j$, so that the above equation can be compactly written $\boldsymbol{\gamma} = \boldsymbol{\Psi} \mathbf{a}$. Orthonormality of the basis vectors leads to the property $\boldsymbol{\Psi}^\dagger \boldsymbol{\Psi} = \mathbf{I}$, where \mathbf{I} is the identity matrix: that is, $\boldsymbol{\Psi}$ is a unitary matrix with $\boldsymbol{\Psi}^{-1} = \boldsymbol{\Psi}^\dagger$. Observing this, we can easily compute the coefficients for a particular data vector:

$$\mathbf{a} = \boldsymbol{\Psi}^\dagger \boldsymbol{\gamma}. \quad (5.2)$$

We will be testing the likelihood of a particular set of coefficients \mathbf{a} . The statistical properties of these coefficients can be written in terms of the covariance of the observed shear:

$$\langle \mathbf{a} \mathbf{a}^\dagger \rangle = \boldsymbol{\Psi}^\dagger \langle \boldsymbol{\gamma} \boldsymbol{\gamma}^\dagger \rangle \boldsymbol{\Psi} \equiv \boldsymbol{\Psi}^\dagger \boldsymbol{\xi} \boldsymbol{\Psi} \quad (5.3)$$

where we have defined the observed shear correlation matrix $\boldsymbol{\xi} \equiv \langle \boldsymbol{\gamma} \boldsymbol{\gamma}^\dagger \rangle$, and angled braces $\langle \cdots \rangle$ denote expectation value or ensemble average of a quantity.

In order to perform a likelihood analysis on the coefficients \mathbf{a} , we will require that \mathbf{a} be statistically orthogonal:

$$\langle \mathbf{a} \mathbf{a}^\dagger \rangle_{ij} = \langle a_i^2 \rangle \delta_{ij} \quad (5.4)$$

Comparing Equations 5.3 & 5.4 we see that the desired basis functions are the solution of the eigenvalue problem

$$\boldsymbol{\xi} \boldsymbol{\Psi}_j = \lambda_j \boldsymbol{\Psi}_j \quad (5.5)$$

where the eigenvalue $\lambda_j = \langle a_i^2 \rangle$. Comparison of this to the KL framework outlined in Chapter 2 shows that the unique basis with these properties is given by the KL decomposition of the shear field γ , represented by the correlation matrix of observations $\boldsymbol{\xi}$. By convention, we'll again order the eigenvalue/eigenvector pairs such that $\lambda_i \geq \lambda_{i+1} \forall i \in (1, N - 1)$. Expansion of the data γ into this basis is the discrete form of KL analysis.

In chapter 2 we discussed the Uniqueness, Efficiency, and Signal-to-noise optimality of KL modes. In particular, we showed that if signal and noise are uncorrelated, then the covariance of the observed shear can be decomposed as

$$\boldsymbol{\xi} = \boldsymbol{\mathcal{S}} + \boldsymbol{\mathcal{N}} \quad (5.6)$$

where $\boldsymbol{\mathcal{S}}$ is the covariance of the signal, and $\boldsymbol{\mathcal{N}}$ is the covariance of the noise. Because the noise covariance $\boldsymbol{\mathcal{N}} \equiv \langle \mathbf{n}_\gamma \mathbf{n}_\gamma^\dagger \rangle$ is proportional to the identity by assumption, diagonalization of $\boldsymbol{\xi}$ results in a simultaneous diagonalization of both the signal $\boldsymbol{\mathcal{S}}$ and the noise $\boldsymbol{\mathcal{N}}$. Based on this signal-to-noise optimization property, KL modes can be proven to be the optimal basis for testing of spatial correlations (see Appendix A of Vogeley & Szalay, 1996).

5.3.1 Shear Noise Properties

The signal-to-noise properties of shear mentioned above are based on the requirement that noise be “white”, that is, the noise covariance is $\boldsymbol{\mathcal{N}} \equiv \langle \mathbf{n}_\gamma \mathbf{n}_\gamma^\dagger \rangle = \sigma^2 \mathbf{I}$. Noise in measured shear is affected mainly by the intrinsic ellipticity and source density, but can also be prone to systematic effects that lead to noise correlations between pixels. When the survey geometry leads to shear with more complicated noise characteristics, a whitening transformation can be applied.

Given the measured data γ and noise covariance \mathcal{N} , we can define the whitened shear

$$\gamma' = \mathcal{N}^{-1/2} \gamma \quad (5.7)$$

With this definition, the shear covariance matrix becomes

$$\begin{aligned} \xi' &= \langle \gamma' \gamma'^{\dagger} \rangle \\ &= \mathcal{N}^{-1/2} \xi \mathcal{N}^{-1/2} \\ &= \mathcal{N}^{-1/2} [\mathcal{S} + \mathcal{N}] \mathcal{N}^{-1/2} \\ &= \mathcal{N}^{-1/2} \mathcal{S} \mathcal{N}^{-1/2} + \mathbf{I} \end{aligned} \quad (5.8)$$

We see that the whitened signal is $\mathcal{S}' = \mathcal{N}^{-1/2} \mathcal{S} \mathcal{N}^{-1/2}$ and the whitened noise is $\mathcal{N}' = \mathbf{I}$, the identity matrix. This transformation whitens the data covariance, so that the noise in each bin is constant and uncorrelated. Given the whitened measurement covariance ξ' , we can find the KL decomposition that satisfies the eigenvalue problem

$$\xi' \Psi'_j = \lambda'_j \Psi'_j \quad (5.9)$$

With KL coefficients given by

$$\mathbf{a}' = \Psi'^{\dagger} \mathcal{N}^{-1/2} \gamma \quad (5.10)$$

Note that because $\langle \gamma \rangle = 0$, the expectation value of the KL coefficients is

$$\begin{aligned} \langle \mathbf{a}' \rangle &= \mathcal{N}^{-1/2} \langle \gamma \rangle \\ &= 0 \end{aligned} \quad (5.11)$$

For the remainder of this chapter, it will be assumed that we are working with whitened quantities. The primes will be dropped for notational simplicity.

5.3.2 Constructing the Covariance Matrix

In many applications, the data covariance matrix can be estimated empirically, using the fact that

$$\tilde{\xi} = \lim_{N \rightarrow \infty} \sum_{i=1}^N \gamma_i \gamma_i^{\dagger} \quad (5.12)$$

Unfortunately, in surveys of cosmic shear, we have only a single sky to observe, so this approach does not work. Instead, we can construct the measurement covariance analytically by assuming a theoretical form of the underlying matter power spectrum.

The measurement covariance ξ_{ij} between two regions of the sky A_i and A_j is given by

$$\begin{aligned}\xi_{ij} &= \mathcal{S}_{ij} + \mathcal{N}_{ij} \\ &= \left[\int_{A_i} d^2x_i \int_{A_j} d^2x_j \xi_+(|\mathbf{x}_i - \mathbf{x}_j|) \right] + \mathcal{N}_{ij}\end{aligned}\quad (5.13)$$

where $\xi_+(\theta)$ is the “+” shear correlation function. $\xi_+(\theta)$ is expressible as an integral over the shear power spectrum weighted by the zeroth-order Bessel function (see, e.g. Schneider et al., 2002a):

$$\xi_+(\theta) = \frac{1}{2\pi} \int_0^\infty d\ell \ell P_\gamma(\ell) J_0(\ell\theta) \quad (5.14)$$

The angular shear power spectrum $P_\gamma(\ell)$ can be expressed as a weighted line-of-sight integral over the matter power

$$P_\gamma(\ell) = \int_0^{\chi_s} d\chi W^2(\chi) \chi^{-2} P_\delta\left(k = \frac{\ell}{\chi}; z(\chi)\right) \quad (5.15)$$

Here χ is the comoving distance, χ_s is the distance to the source, and $W(\chi)$ is the lensing weight function,

$$W(\chi) = \frac{3\Omega_{m,0}H_0^2}{2a(\chi)} \frac{\chi}{\bar{n}_g} \int_\chi^{\chi_s} dz n(z) \frac{\chi(z) - \chi}{\chi(z)} \quad (5.16)$$

where $n(z)$ is the empirical redshift distribution of galaxies. The nonlinear mass fluctuation power spectrum $P_\delta(k, z)$ can be predicted semi-analytically: in this work we use the halo model of Smith et al. (2003). With this as an input, we can analytically construct the measurement covariance matrix ξ using Equations 5.13-5.16.

5.3.3 Cosmological Likelihood Analysis with KL

The cosmological analysis with KL consists of the following steps: from the survey geometry and galaxy ellipticities, we measure the shear γ , estimate the noise covariance \mathcal{N} (see §5.4.1) and derive the whitened covariance matrix ξ . From ξ we compute the KL basis Ψ and λ . Using the KL basis, we compute the coefficients $\mathbf{a} = \Psi^\dagger \mathcal{N}^{-1/2} \gamma$. Given these KL coefficients

\mathbf{a} , we use a Bayesian framework to compute the posterior distribution of our cosmological parameters.

The problem of Bayesian inference with KL was discussed in §2.4. Here we will briefly outline the portions relevant to this chapter. Given observations D and prior information I , Bayes' theorem specifies the posterior probability of a model described by the parameters $\{\theta_i\}$:

$$P(\{\theta_i\}|DI) = P(\{\theta_i\}|I) \frac{P(D|\{\theta_i\}I)}{P(D|I)} \quad (5.17)$$

The term on the left of the equality is the *posterior* probability of the set of model parameters $\{\theta_i\}$, which is the quantity we are interested in. The likelihood function for the observed coefficients \mathbf{a} enters into the numerator $P(D|\{\theta_i\}I)$. The denominator $P(D|I)$ is essentially a normalization constant, set so that the total probability over the parameter space equals unity.

For a given model $\{\theta_i\}$, we can predict the expected distribution of model KL coefficients $\mathbf{a}_{\{\theta_i\}} \equiv \Psi^\dagger \mathcal{N}^{-1/2} \gamma$:

$$\begin{aligned} \mathbf{C}_{\{\theta_i\}} &\equiv \langle \mathbf{a}_{\{\theta_i\}} \mathbf{a}_{\{\theta_i\}}^\dagger \rangle \\ &= \Psi^\dagger \mathcal{N}^{-1/2} \boldsymbol{\xi}_{\{\theta_i\}} \mathcal{N}^{-1/2} \Psi \end{aligned} \quad (5.18)$$

Using this, the measure of departure from the model m is given by the quadratic form

$$\chi^2 = \mathbf{a}^\dagger \mathbf{C}_{\{\theta_i\}}^{-1} \mathbf{a} \quad (5.19)$$

The likelihood is then given by

$$\mathcal{L}(\mathbf{a}|\{\theta_i\}) = (2\pi)^{n/2} |\det(\mathbf{C}_{\{\theta_i\}})|^{-1/2} \exp(-\chi^2/2) \quad (5.20)$$

where n is the number of degrees of freedom: that is, the number of eigenmodes included in the analysis. The likelihood given by Equation 5.20 enters into Equation 5.17 when computing the posterior probability.

5.4 COSMOS data

To test the KL likelihood formalism, we use a shear catalog derived from the COSMOS survey¹. A full description of this catalog and detailed tests of its systematics are presented

¹We are grateful to Tim Schrabback et al. for making these data available to us

in Schrabback et al. (2010, hereafter S10); we will summarize some relevant details here. The catalog contains shape measurements of 446,934 source galaxies in a 1.64 square-degree field. The “bright” sample of 194,976 galaxies are those with well-behaved photometric redshifts drawn from the COSMOS30 pipeline (Hildebrandt et al., 2009, S10). The angular distribution of these galaxies is shown in the upper panel of Figure 5.1, and the redshift distribution is shown in the upper panel of Figure 5.2. The redshift distribution is marked by spikes indicating the presence of clusters of galaxies at the same redshift.

The remaining 446,909 galaxies are too faint to have been included in the reference catalog (the COSMOS30 redshifts are limited to $i^+ < 25$; See Ilbert et al., 2009), and S10 estimates their redshift distribution using the empirical relationship between redshift and absolute i -band magnitude. The spatial and redshift distributions of this “faint” galaxy sample are shown in the lower panels of Figures 5.1 and 5.2, respectively.

In addition, S10 identifies potential catastrophic outliers in the redshifts. Photometric redshifts gain significant leverage from broad spectral features such as the Lyman and Balmer spectral breaks. The Balmer limit is $\sim 364\text{nm}$, while the Lyman limit is $\sim 91\text{nm}$, so that the Balmer limit of a galaxy at redshift z_0 is at the same observed wavelength as the Lyman limit at redshift $z_0 + 3$. This can lead to a degeneracy in redshift determination that results in catastrophic outliers – that is, low redshift galaxies identified as high redshift, or high redshift galaxies identified as low redshift. In shear studies, the former acts to dilute the high- z shear signal, while the latter acts to add spurious signal at low redshift. To prevent the latter effect from affecting results, we follow S10 and remove galaxies with $i^+ > 24$ and redshifts $z < 0.6$. S10 provides several tests which show that this cut does not generate appreciable systematic error.

S10 performs a classical shear correlation function analysis to find constraints on σ_8 and Ω_M that are consistent with those derived from WMAP: for a flat ΛCDM cosmology, they find with 63% confidence $\sigma_8(\Omega_M/0.3)^{0.51} = 0.79 \pm 0.09$. S10 performs both a two-dimensional analysis and a three dimensional analysis: the constraints from each are consistent, with a slightly better figure of merit for the Ω_M vs. σ_8 constraint when the analysis is computed within several redshift bins. The strength of the 3D treatment comes when we drop assumptions about flatness or the dark energy equation of state: for a ΛCDM

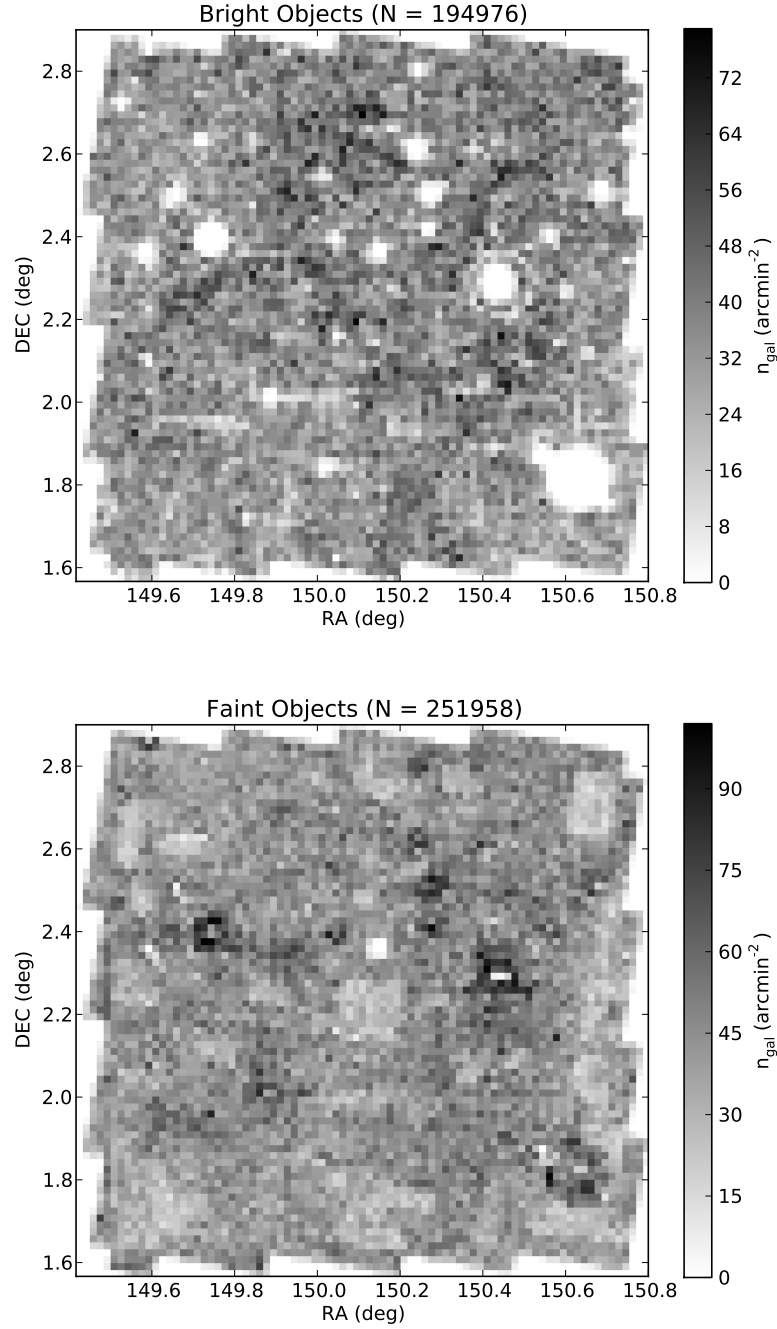


Figure 5.1: Angular locations of the 194,976 COSMOS galaxies with photometric redshift measurements (top panel) and the 251,958 COSMOS galaxies without photometric redshift estimates (bottom panel). The masking due to bright foreground sources is evident in both panels.

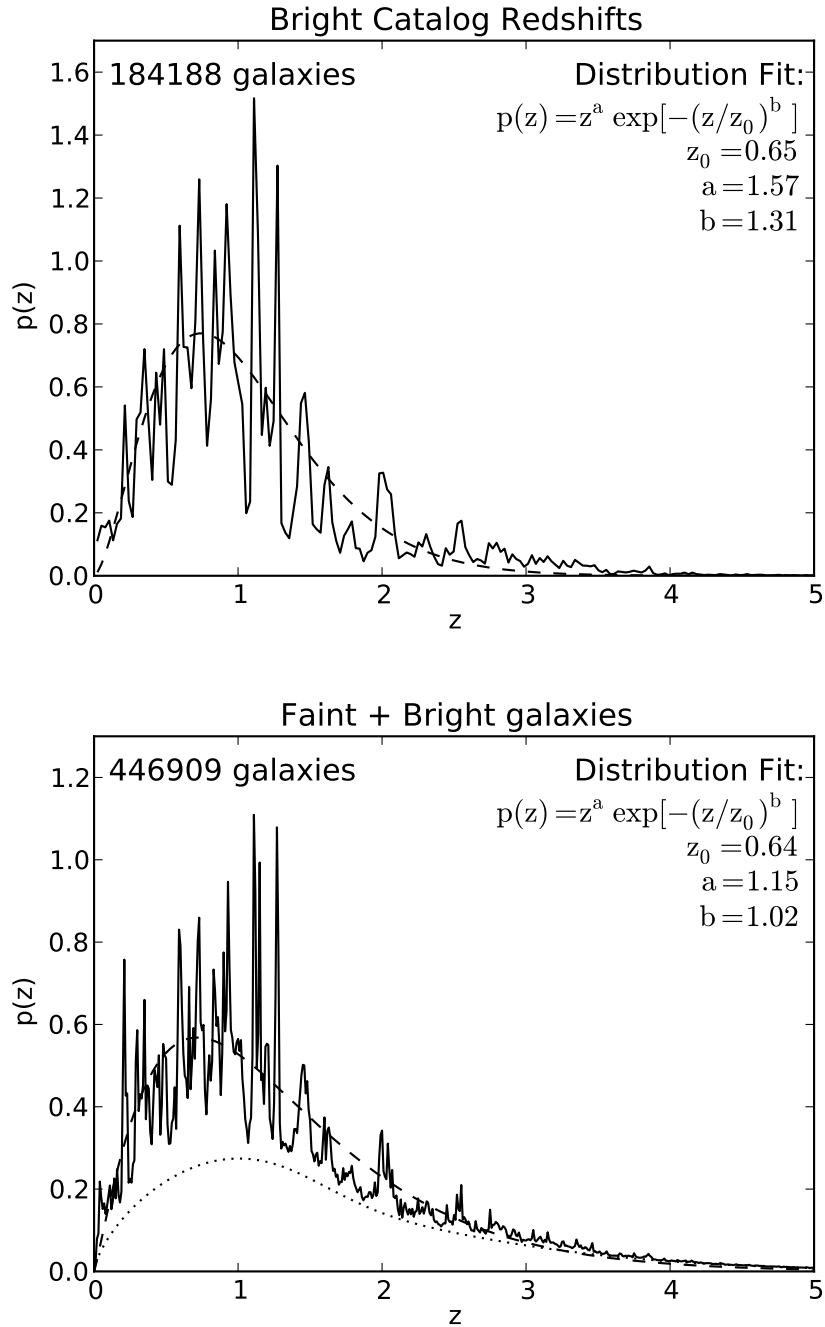


Figure 5.2: Redshift distributions of the COSMOS data. The top panel shows the distribution of photometric redshifts of the shear catalog cross-matched with the COSMOS30 photometric redshift catalog (Ilbert et al., 2009), while the bottom panel includes the inferred redshift distribution of the remaining faint galaxies.

cosmology with varying dark energy equation of state w , S10 finds at 90% confidence that $w < -0.41$. Though these constraints offer only a slight improvement over prior information from WMAP constraints from measurements of the CMB, we must note that they are derived from just over 1 square degree of observations, while the WMAP constraints use the full sky. Future wide-field lensing surveys will be able to place much more competitive constraints on these parameters.

Here we will not duplicate all the various analyses of S10: instead we will use the KL-based estimation formalism of §2.4 with shear eigenbases computed for the observed field via the formalism of §2.5. This will enable us to constrain two-point information using the KL formalism.

5.4.1 *Intrinsic Ellipticity estimation*

In order to apply the KL analysis techniques discussed above and in Chapter 2, we require an accurate determination of the noise for the observed shear. Assuming systematic errors are negligible, shape noise should be dominated by shot noise, which scales as $\mathcal{N}_{ii} = \hat{\sigma}_\epsilon^2/n_i$, with n_i representing the number of galaxies in bin i .

To test this assumption, we perform a bootstrap resampling of the observed shear in square pixels that are two arcminutes on a side. Generating 1000 bootstrap samples within each pixel, we compute the variance in each pixel. From Poisson statistics, we would expect the variance in each pixel to scale inversely with the number of measurements within each pixel: with this in mind we plot in Figure 5.3 the variance vs the number of galaxies and fit a curve of the form

$$\sigma_\gamma^2 = \frac{\sigma_{int}^2}{n_{gal}}, \quad (5.21)$$

where σ_{int} is the intrinsic ellipticity dispersion of the population. As shown in the upper panel of Figure 5.3, the best-fit curve has $\sigma_{int} = 0.393$. The residual distribution, shown in the lower panel of the figure, is close to Gaussian as expected.

In this figure, we see that the pixel-to-pixel fluctuation in shape noise is only a few percent. For the analysis below, we use for each pixel the noise estimates derived the bootstrap resampling within each pixel. Because bootstrapping is inaccurate for pixels with

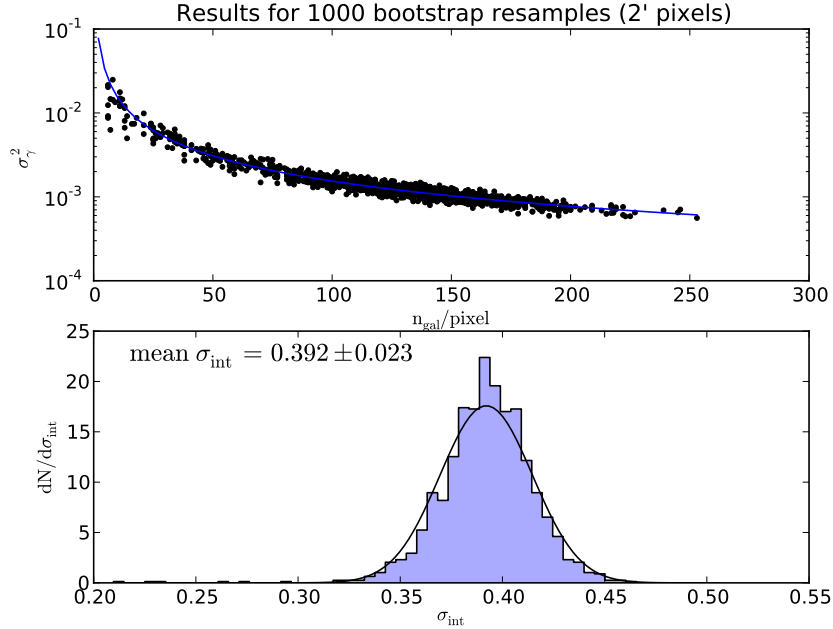


Figure 5.3: Bootstrap estimates of the shape noise for each pixel. The estimates reflect an intrinsic ellipticity of 0.393 ± 0.013 .

a small number of galaxies, if a pixel has fewer than 10 sources we use the best-fit estimate for the noise, $\mathcal{N}_{ii} = \hat{\sigma}_\epsilon^2/n_i$ with $\hat{\sigma}_\epsilon = 0.392$. Pixels with zero galaxies (i.e. masked pixels) are treated using the techniques developed in Section 5.3.

5.4.2 Whitenes KL modes

Using the pixel-by-pixel noise estimates from the previous section, we can now follow the formalism of §5.3 and construct the optimal orthonormal basis across the survey window defined by the selection function of the bright galaxies from the COSMOS survey. We use pixels that are two arcminutes on a side, in a grid of $40 \times 41 = 1640$ total pixels. We whiten the theoretical correlation matrix according to the noise properties of the observed data, and compute the eigenvalue decomposition of the resulting correlation matrix.

The first nine eigenmodes for the bright galaxy sample are shown in Figure 5.4. It is interesting to compare these to the modes shown in Figure 4.1, which are derived under

the assumption that each pixel has the same number of sources, and thus the same noise properties. The window function of the COSMOS survey is clearly present, as can be seen by comparing the masking apparent in the eigenmodes to that of the galaxy distribution shown in the upper panel of Figure 5.1. Moreover, the asymmetry of the mask acts as a perturbation that destroys the rotational symmetry evident in the idealized eigenmodes of the previous chapter (See Figure 4.1).

The eigenvalues of the whitened correlation matrix are shown in Figure 5.5. Because the covariance matrix is whitened, the noise is normalized to 1 within each mode. Similar to the results seen in the previous chapter, only a very small number of modes have signal-to-noise greater than 1. This figure also shows that the signal drops to zero at just over 1500 modes. This is due to the survey mask: approximately 120 of the 1640 modes are completely masked, such that they have no signal and do not contribute to the correlation matrix.

As discussed above, an advantage of KL is its ability to yield an optimal low-rank approximation of a set of observations, by truncating the low signal-to-noise modes in a reconstruction. The choice of which modes to truncate for a reconstruction or other analysis is not straightforward: as discussed in Chapters 3-4, this decision amounts to a tradeoff between systematic bias and statistical error. Below we impose a cutoff for modes with signal-to-noise ratios of less than $\sim 1/10$, corresponding to mode number 800. This lies approximately at the inflection point of the signal-to-noise curve.

5.4.3 *Is our shear Gaussian?*

The KL formalism for shear analysis assumes that the shear is well-described by a Gaussian random field described by a covariance matrix, with mean zero. If this is the case, then (by the arguments of Chapter 2) we would expect the observed KL coefficients of the whitened signal to be Gaussian distributed with zero mean and variance equal to the associated eigenvalue. Figure 5.6 shows a histogram of the observed coefficients scaled by the corresponding eigenvalue. As is evident, both the real part and the imaginary part of the scaled coefficients are consistent with being drawn from a standard normal distribution. This is consistent

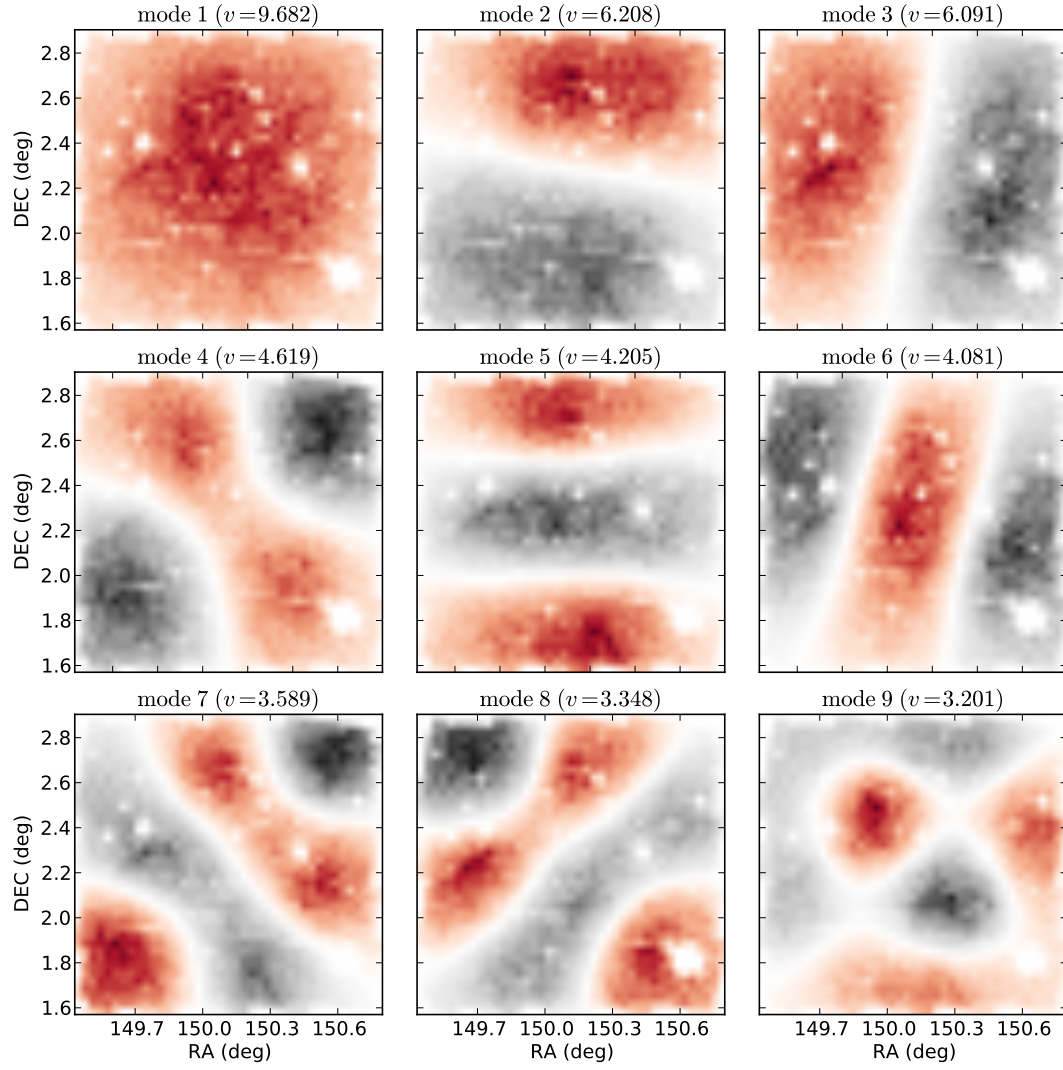


Figure 5.4: The first nine 2D KL signal-to-noise eigenmodes for the COSMOS bright objects. This uses square pixels that are two arcminutes on a side, leading to $41 \times 40 = 1640$ pixels over the entire field. Compare these results to the KL modes shown in Figure 4.1.

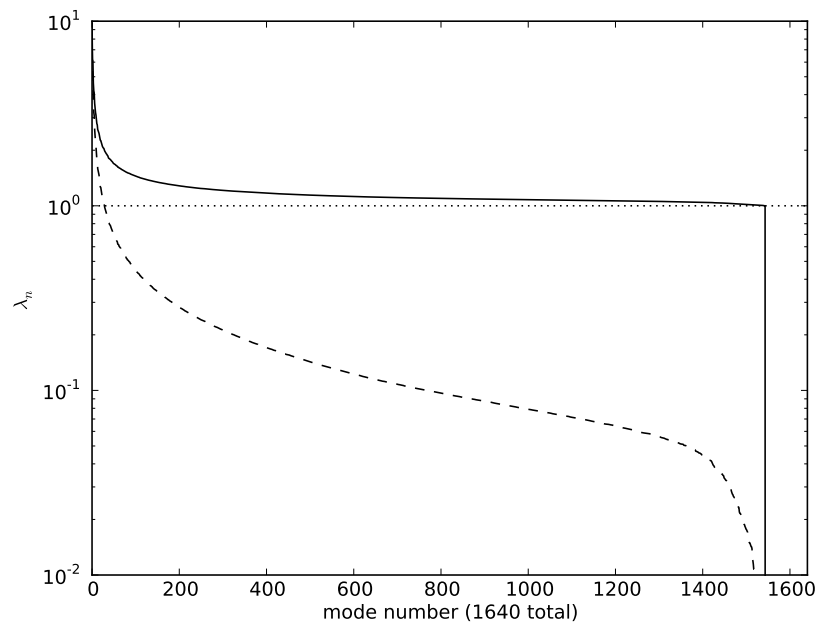


Figure 5.5: The distribution of KL eigenvalues for the eigenmodes shown in Figure 5.4. There are $41 \times 40 = 1640$ pixels, but approximately 90 of these contain no sources and are part of the mask. This is reflected in the fact that the final 90 KL modes have zero eigenvalue.

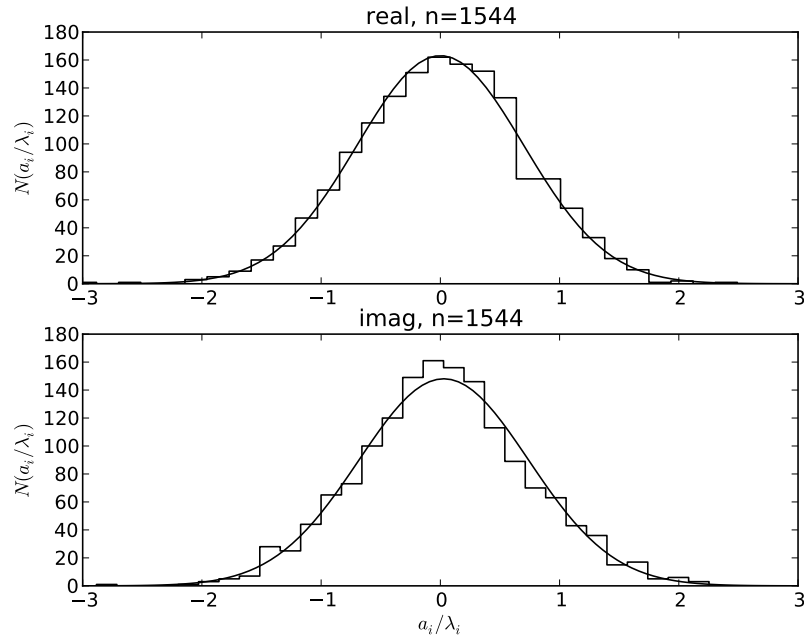


Figure 5.6: The histogram of normalized coefficients $a_i/\sqrt{\lambda_i}$. If the shear is truly a Gaussian random field, this distribution should be a Gaussian with unit variance.

with our assumption that the shear is drawn from a Gaussian random field, and that the noise properties estimated in §5.4.1 are accurate.

5.4.4 Relationship to Power Spectrum

As we did in Figure 4.2, for each KL mode we compute the associated two-dimensional power spectrum to determine the relationship between each mode and the Fourier power it represents. For the unmasked KL modes explored in the previous chapter, this relationship displayed a fairly tight scatter between KL mode number and Fourier mode number. As seen in Figure 5.7, however, we see that the masked KL modes have a much larger scatter in associated Fourier modes, especially for higher KL mode numbers.

The analysis reflected in this plot can help in the choice of which KL modes to truncate: the pixel scale is two arcmin, which corresponds to a dimensionally-averaged Nyquist

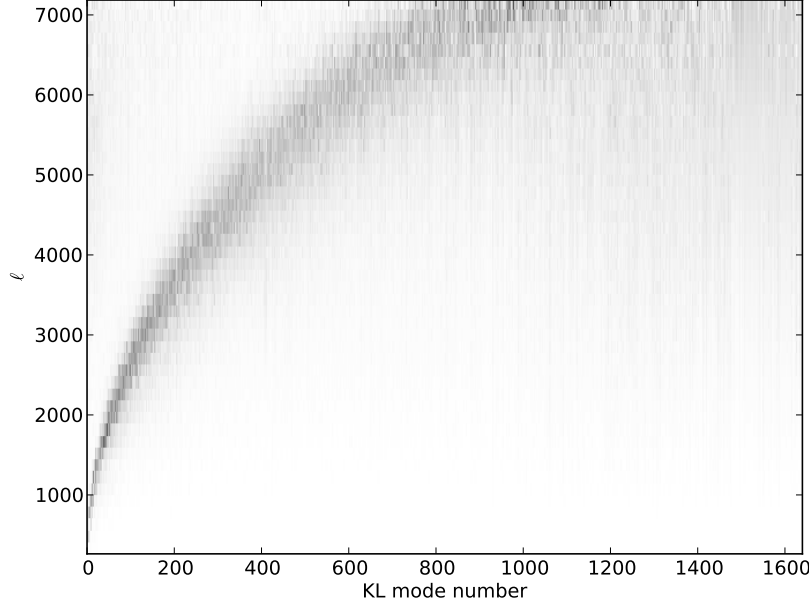


Figure 5.7: The Fourier power represented by each KL mode. For each KL mode number, the vertical band shows the distribution of power with angular wavenumber ℓ . In general, the larger KL modes correspond to larger values of ℓ , though there is significant mode mixing.

frequency of

$$\ell = \left(\frac{1}{\sqrt{2}} \right) \left(\frac{2\pi \text{ rad}}{2 \text{ arcmin}} \right) \approx 7200. \quad (5.22)$$

So modes which do not have significant Fourier power on angular scales $\ell < 7200$ are likely to be limited in their usefulness for parameter estimation from shear on this grid. This scale does not tell the whole story, however. The KL analysis tells us that the smaller scales probed by the higher-order modes have progressively smaller signal-to-noise ratios. For this reason, we choose the mode cutoff at scales less than 7200, which corresponds to $n \sim 800$ modes. As was the case in Chapter 4, the optimal choice of mode cutoff is hard to quantify precisely, and represents a fundamental tradeoff between statistical and systematic errors. Modes larger than our cutoff of 800 have an expected signal-to-noise of less than 1/10.

5.5 Results

The result of the KL-based Bayesian inference for cosmological parameter estimation is shown in Figure 5.8. To compute the eigenmodes, we assume a flat Λ CDM cosmology with $\Omega_M = 0.27$, $\Omega_L = 0.73$, $\sigma_8 = 0.812$, and $h = 0.71$. These KL modes are computed for the angular and redshift distribution of the bright galaxy sample, and the KL-based Bayesian inference is performed assuming a flat cosmology. We use only a single redshift bin in this case, which is comparable to the first analysis performed in S10.

This leads to a best-fit cosmology $\Omega_M = 0.23 \pm 0.06$, $\sigma_8 = 0.83 \pm 0.09$, where the error bars represent 1σ deviations about the maximum *a priori* value. This does not capture the entire story, however, as there is a strong degeneracy between the parameters (note that WMAP data offers complementary constraints in this plane, and can be used to break this degeneracy: see S10). Following S10, we describe this degeneracy by computing a power-law fit to the posterior distribution, to find

$$\sigma_8(\Omega_M/0.3)^{1.03} = 0.88 \pm 0.14. \quad (5.23)$$

This should be compared to the S10 result for the 2D analysis, $\sigma_8(\Omega_M/0.3)^{0.62} = 0.62 \pm 0.11$.

Compared to S10, our results show a 50% broader constraint on σ_8 , as well as a stronger degeneracy between σ_8 and Ω_M (reflected in the exponent of the relation). This discrepancy is likely due to the fact that we use only the bright galaxies in this analysis, while the S10 results use both bright and faint galaxies, as well as the fact that S10 marginalizes over nuisance parameters (the Hubble parameter and redshift systematic corrections) while we fix these at the expected values.

S10 notes that the low value of σ_8 seen in their 2D analysis is likely an artifact of cosmic variance: the strongest contributions to lensing signals in COSMOS are from $z > 0.7$, which boosts the shear signal for higher redshift sources but leads to a lower signal at intermediate redshifts. Using the full 3D analysis, S10 is able to separate these regions, leading to results consistent with those from WMAP.

Here we have limited the analysis to two dimensions, but this is by no means a fundamental limitation of KL. As long as we can sufficiently estimate the correlation of signal and

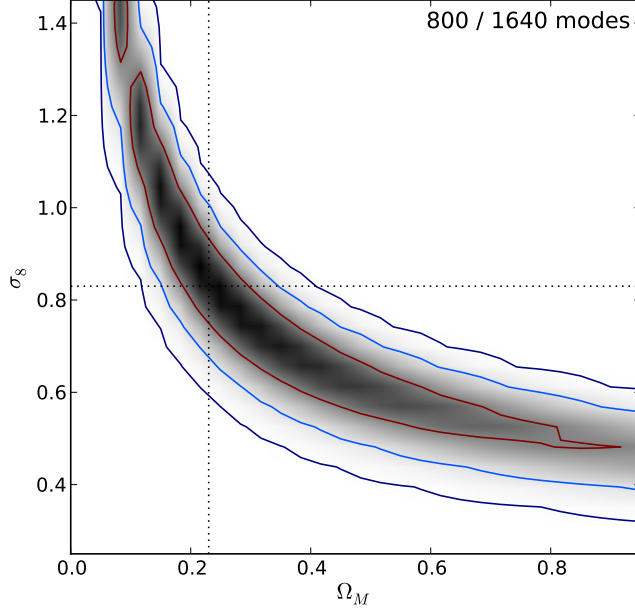


Figure 5.8: The posterior distribution in the (Ω_M, σ_8) plane for a 2D analysis of the bright galaxy sample. This uses 800 of the 1640 modes, such that the truncated modes have average signal-to-noise ratios of $< \sim 1/10$, and an approximate angular scale of $\ell \sim 7000$, which corresponds to 3 arcmin or 1.5 pixel-lengths.

noise, KL can be used to analyze an arbitrary geometry: in future work we will extend the present analysis to three dimensions, fully taking into account the redshifts of the sources.

5.6 Next Steps

The above analysis presents a firm basis for further exploring the ability of KL to provide a natural basis for extracting two-point information from weak lensing surveys. Further work is needed to fully understand the effect of the mode truncation on results, as well as other effects such as the pixel size, the assumptions of noise, and the effect of the assumed fiducial cosmology.

There are also some potentially interesting and useful features of the algorithm: first of all, the KL framework naturally extends from two dimensions to three. Unlike the rigidly tomographic approach used in conventional correlation function studies, KL allows each

pixel to have its redshift distribution individually specified, potentially leading to a more robust use of source redshift information. For this reason, KL is a promising technique for a full 3D analysis, and will give insight into the density and perhaps equation of state of dark energy.

Second, assumptions about noise and bias can be built-in to the KL model. For example, S10 does a careful job of correcting for the shape of the HST PSF before computing the observed correlation function. With KL, we could instead account for these biases in the KL basis itself, allowing us to perform our cosmological analysis one step closer to the observed data.

Third, there is the question of how this approach can scale from the one square degree of COSMOS to the 20,000 square degrees of LSST. The LSST weak lensing analysis has potential to give very tight constraints on cosmological parameters, especially the possible evolution of dark energy. It will be increasingly important to address and explore how this KL framework can be scaled to the size of future surveys.

Chapter 6

CONCLUSION

In the above chapters, we have developed the Karhunen-Loève analysis as a useful tool for several aspects of the analysis of present and future weak lensing surveys. In Chapter 2, we discussed the details of the KL formalism. We showed that KL is a powerful technique that enables data to be represented as a linear combination of orthogonal modes that are constructed such that the modes are optimal representations of the signal-to-noise ratio.

In Chapter 3, we demonstrated that KL can be used to construct an optimal linear framework for the mapping of three dimensional structure from weak lensing surveys. The KL filtering leads to an algorithm which is orders of magnitude faster than previously studied approaches, and allows quantitative constraints on the effectiveness of mapping for given survey depths and geometries.

In Chapter 4, we demonstrated that KL can be used to address a practical problem for two and three dimensional mass mapping: the interpolation of shear signal across masked regions of a given survey. The reconstruction takes into account theoretical expectations of the shear correlation, and results in peak counts that are more consistent with those of the underlying distribution. The KL approach also results in a natural filtration of low-magnitude noisy peaks, which has the potential to increase the performance of cosmological likelihood calculations from peak statistics of shear.

In Chapter 5, we show how KL can be used directly as a tool to derive cosmological parameter constraints from two-point information within a Bayesian inference framework. Because KL can naturally account for arbitrary survey masks and geometries, it allows for robust determination of likelihoods without the need for computationally expensive calibration against N-body simulations. As a proof-of-concept, we perform a two-dimensional likelihood analysis to derive constraints on σ_8 and Ω_M which are consistent with those derived from conventional correlation-function approaches using the same data.

In these three important areas of weak lensing analysis, the KL approach has proven valuable in addressing the practical problems associated with the science of weak lensing. KL's robust, computationally efficient approach has the potential to be very useful in many areas of future weak lensing science.

This thesis opens nearly as many questions as it answers. In the future, we would like to explore more deeply how the shear KL basis can be used to address real problems in data analysis. Chapters 4 and 5 end with discussions of some remaining questions: can the KL analysis of projected shear peaks lead to robust cosmology constraints from realistic datasets? Can the KL power spectrum approach be extended to 3D and make use of our knowledge about the correlated statistical and systematic errors in real weak lensing data?

Beyond that, we can ask other questions: is KL the best basis to use for these sorts of studies? In chapter 2, we show that KL gives the optimal low-rank reconstruction and noise filtering among all possible linear, orthonormal bases. This does not, however, exclude the possibility of using other non-standard representations of the data, such as non-orthonormal or overcomplete bases. Such approaches are common in the fields of sparse coding and compressed sensing, and may also be fruitful methods within the field of weak lensing.

BIBLIOGRAPHY

- Aitken, A. 1934, Proc. R. Soc. Edinb, 55, 42
- Alpher, R. A., Bethe, H., & Gamow, G. 1948, Phys. Rev., 73, 803
- Alpher, R. A., & Herman, R. C. 1948, Physical Review, 74, 1737
- Bacon, D. J., & Taylor, A. N. 2003, MNRAS, 344, 1307
- Bartelmann, M., & Schneider, P. 2001, Phys. Rep., 340, 291
- Birkhoff, G., & Langer, R. 1923, Relativity and modern physics (Harvard University Press)
- Brown, M. L., Taylor, A. N., Bacon, D. J., et al. 2003, MNRAS, 341, 100
- Chevallier, M., & Polarski, D. 2001, International Journal of Modern Physics D, 10, 213
- Clowe, D., Bradač, M., Gonzalez, A. H., et al. 2006, ApJ, 648, L109
- Connolly, A. J., & Szalay, A. S. 1999, AJ, 117, 2052
- Connolly, A. J., Szalay, A. S., Bershad, M. A., Kinney, A. L., & Calzetti, D. 1995, AJ, 110, 1071
- Courant, R., & Hilbert, D. 1989, Methods of mathematical physics, Wiley classics library No. v. 1 (Wiley)
- Crittenden, R. G., Natarajan, P., Pen, U., & Theuns, T. 2002, ApJ, 568, 20
- de Putter, R., & White, M. 2005, New A, 10, 676
- Dietrich, J. P., & Hartlap, J. 2010, MNRAS, 402, 1049
- Djorgovski, S., & Davis, M. 1987, ApJ, 313, 59
- Dodelson, S., Shapiro, C., & White, M. 2006, Phys. Rev. D, 73, 023009

- Efstathiou, G., & Fall, S. M. 1984, MNRAS, 206, 453
- Eisenstein, D. J., Zehavi, I., Hogg, D. W., et al. 2005, ApJ, 633, 560
- Faber, S. M., & Jackson, R. E. 1976, ApJ, 204, 668
- Fan, Z., Shan, H., & Liu, J. 2010, ApJ, 719, 1408
- Freedman, W. L., Madore, B. F., Gibson, B. K., et al. 2001, ApJ, 553, 47
- Giodini, S., Pierini, D., Finoguenov, A., et al. 2009, ApJ, 703, 982
- Gorski, K. M. 1994, ApJ, 430, L85
- Grossi, M., Dolag, K., Branchini, E., Matarrese, S., & Moscardini, L. 2007, MNRAS, 382, 1261
- Hamana, T., Takada, M., & Yoshida, N. 2004, MNRAS, 350, 893
- Heavens, A. 2003, MNRAS, 343, 1327
- Hennawi, J. F., & Spergel, D. N. 2005, ApJ, 624, 59
- Hikage, C., Takada, M., Hamana, T., & Spergel, D. 2010, ArXiv e-prints
- . 2011, MNRAS, 412, 65
- Hildebrandt, H., Pielorz, J., Erben, T., et al. 2009, A&A, 498, 725
- Hoekstra, H. 2003, MNRAS, 339, 1155
- Hogg, D. W. 1999, Distance measures in cosmology, cite arxiv:astro-ph/9905116
- Hu, W., & Keeton, C. R. 2002, Phys. Rev. D, 66, 063506
- Hubble, E. 1929, Proceedings of the National Academy of Science, 15, 168
- Ichiki, K., Takada, M., & Takahashi, T. 2009, Phys. Rev. D, 79, 023520
- Ilbert, O., Capak, P., Salvato, M., et al. 2009, ApJ, 690, 1236

- Kaiser, N., & Squires, G. 1993, *ApJ*, 404, 441
- Kessler, R., Becker, A. C., Cinabro, D., et al. 2009, *ApJS*, 185, 32
- Kilbinger, M., & Munshi, D. 2006, *MNRAS*, 366, 983
- Kilbinger, M., & Schneider, P. 2004, *A&A*, 413, 465
- Kolb, E. W., & Turner, M. S. 1990, *The early universe*.
- Komatsu, E., Smith, K. M., Dunkley, J., et al. 2011, *ApJS*, 192, 18
- Kratochvil, J. M., Haiman, Z., & May, M. 2010, *Phys. Rev. D*, 81, 043519
- Kratochvil, J. M., Lim, E. A., Wang, S., et al. 2011, in *Bulletin of the American Astronomical Society*, Vol. 43, American Astronomical Society Meeting Abstracts #217, #225.02–+
- Krause, E., & Hirata, C. M. 2010, *A&A*, 523, A28
- Leavitt, H. S., & Pickering, E. C. 1912, *Harvard College Observatory Circular*, 173, 1
- Lin, Y., Mohr, J. J., & Stanford, S. A. 2003, *ApJ*, 591, 749
- Linder, E. V. 2003, *Physical Review Letters*, 90, 091301
- Linder, E. V., & Jenkins, A. 2003, *MNRAS*, 346, 573
- Longair, S. 2008, *Galaxy Formation, Astronomy and Astrophysics Library* (Springer)
- LSST Science Collaborations, Abell, P. A., Allison, J., et al. 2009, *ArXiv e-prints*
- Maartens, R. 2011, *Royal Society of London Philosophical Transactions Series A*, 369, 5115
- Mandelbaum, R., Seljak, U., Baldauf, T., & Smith, R. E. 2010, *MNRAS*, 405, 2078
- Marian, L., Smith, R. E., & Bernstein, G. M. 2009, *ApJ*, 698, L33
- . 2010, *ApJ*, 709, 286
- Massey, R., Rhodes, J., Leauthaud, A., et al. 2007, *ApJS*, 172, 239

- Matarrese, S., Verde, L., & Jimenez, R. 2000, *ApJ*, 541, 10
- Matsubara, T., Szalay, A. S., & Landy, S. D. 2000, *ApJ*, 535, L1
- Maturi, M., Fedeli, C., & Moscardini, L. 2011, ArXiv e-prints
- Mellier, Y. 1999, *ARA&A*, 37, 127
- Munshi, D., & Kilbinger, M. 2006, *A&A*, 452, 63
- Narayan, R., & Bartelmann, M. 1996, ArXiv Astrophysics e-prints
- Navarro, J. F., Frenk, C. S., & White, S. D. M. 1997, *ApJ*, 490, 493
- Neyrinck, M. C., Szapudi, I., & Szalay, A. S. 2009, *ApJ*, 698, L90
- . 2010, ArXiv e-prints
- Oguri, M., Bayliss, M. B., Dahle, H., et al. 2012, *MNRAS*, 420, 3213
- Padmanabhan, N., Seljak, U., & Pen, U. L. 2003, *New Astronomy*, 8, 581
- Peacock, J. 1999, *Cosmological Physics*, Cambridge Astrophysics Series (Cambridge University Press)
- Peebles, P. 1993, *Principles of Physical Cosmology*, Princeton Series in Physics (Princeton University Press)
- Perlmutter, S., Aldering, G., Goldhaber, G., et al. 1999, *ApJ*, 517, 565
- Phillips, M. M. 1993, *ApJ*, 413, L105
- Pires, S., Starck, J., Amara, A., et al. 2009, *MNRAS*, 395, 1265
- Pope, A. C., Matsubara, T., Szalay, A. S., et al. 2004, *ApJ*, 607, 655
- Press, W. H., & Schechter, P. 1974, *ApJ*, 187, 425
- Riess, A. G., Filippenko, A. V., Challis, P., et al. 1998, *AJ*, 116, 1009
- Rines, K., Diaferio, A., & Natarajan, P. 2007, *ApJ*, 657, 183

- Ryden, B. 2003, *Introduction to cosmology* (Addison-Wesley)
- Sarkar, P., Yadav, J., Pandey, B., & Bharadwaj, S. 2009, *MNRAS*, 399, L128
- Scherrer, R. J., Berlind, A. A., Mao, Q., & McBride, C. K. 2010, *ApJ*, 708, L9
- Schirmer, M., Erben, T., Hetterscheidt, M., & Schneider, P. 2007, *A&A*, 462, 875
- Schmidt, F., & Rozo, E. 2010, *ArXiv e-prints*
- Schneider, P., Eifler, T., & Krause, E. 2010, *A&A*, 520, A116+
- Schneider, P., van Waerbeke, L., Jain, B., & Kruse, G. 1998, *MNRAS*, 296, 873
- Schneider, P., van Waerbeke, L., Kilbinger, M., & Mellier, Y. 2002a, *A&A*, 396, 1
- Schneider, P., van Waerbeke, L., & Mellier, Y. 2002b, *A&A*, 389, 729
- Schrabback, T., Hartlap, J., Joachimi, B., et al. 2010, *A&A*, 516, A63+
- Seitz, S., & Schneider, P. 1996, *A&A*, 305, 383
- Seo, H., Sato, M., Dodelson, S., Jain, B., & Takada, M. 2011, *ApJ*, 729, L11+
- Shapiro, C. 2009, *ApJ*, 696, 775
- Sheth, R. K., & Tormen, G. 1999, *MNRAS*, 308, 119
- Simon, P., Taylor, A. N., & Hartlap, J. 2009, *MNRAS*, 399, 48
- Smith, R. E., Peacock, J. A., Jenkins, A., et al. 2003, *MNRAS*, 341, 1311
- Smoot, G. F., Bennett, C. L., Kogut, A., et al. 1992, *ApJ*, 396, L1
- Spergel, D. N., Verde, L., Peiris, H. V., et al. 2003, *ApJS*, 148, 175
- Szalay, A. S., Jain, B., Matsubara, T., et al. 2003, *ApJ*, 591, 1
- Takada, M., & Jain, B. 2003, *MNRAS*, 344, 857
- . 2004, *MNRAS*, 348, 897

—. 2009, MNRAS, 395, 2065

Taylor, A. N. 2001, ArXiv Astrophysics e-prints

Tegmark, M. 1997, ApJ, 480, L87+

Tegmark, M., Eisenstein, D. J., Strauss, M. A., et al. 2006, Phys. Rev. D, 74, 123507

Tully, R. B., & Fisher, J. R. 1977, A&A, 54, 661

VanderPlas, J. T., Connolly, A. J., Jain, B., & Jarvis, M. 2011, ApJ, 727, 118

—. 2012, ApJ, 744, 180

Vikhlinin, A., Kravtsov, A. V., Burenin, R. A., et al. 2009, ApJ, 692, 1060

Vogeley, M. S., & Szalay, A. S. 1996, ApJ, 465, 34

Wang, S., Haiman, Z., & May, M. 2009, ApJ, 691, 547

Wechsler, R. H. 2004, Clusters of Galaxies: Probes of Cosmological Structure and Galaxy Evolution

White, S. D. M., Efstathiou, G., & Frenk, C. S. 1993, MNRAS, 262, 1023

Yadav, J., Bharadwaj, S., Pandey, B., & Seshadri, T. R. 2005, MNRAS, 364, 601

Yip, C. W., Connolly, A. J., Szalay, A. S., et al. 2004a, AJ, 128, 585

Yip, C. W., Connolly, A. J., Vanden Berk, D. E., et al. 2004b, AJ, 128, 2603

Appendix A

RANDOM FIELDS, CORRELATION FUNCTIONS, AND POWER SPECTRA

In this appendix we discuss some of the details of the mathematics behind random fields, and their correlation functions and power spectra. In Appendix A.2 we apply this to the cosmological density field introduced in Chapter 1, and from this define the power spectrum normalization σ_8 . Some common window functions and their Fourier transforms are listed in Appendix A.3.

A.1 Background on Gaussian random fields

Consider a field $g(\vec{x})$ in n dimensions. We'll enforce a few restrictions on this field to make it easier to work with. Note that $\langle \cdot \rangle$ denotes a volume-average:

1. vanishing: $\langle g(\vec{x}) \rangle = 0$ for all \vec{x} .
2. homogeneous: $g(\vec{x} + \vec{y})$ is statistically equivalent to $g(\vec{x})$ for all \vec{x} and \vec{y} .
3. isotropic: $g(\mathbf{R}\vec{x})$ is statistically equivalent to $g(\vec{x})$ for all \vec{x} and any unitary rotation matrix \mathbf{R} .

These conditions become very useful when we study the (auto) correlation function, defined as

$$C_{gg}(\vec{r}) \equiv \langle g(\vec{x})g^*(\vec{x} + \vec{r}) \rangle \quad (\text{A.1})$$

which for a homogeneous and isotropic field depends only on the distance $r = |\vec{r}|$. It becomes useful to decompose g into orthogonal Fourier components:¹

$$g(\vec{x}) = \int \frac{d^n k}{(2\pi)^n} \hat{g}(\vec{k}) e^{-i\vec{k} \cdot \vec{x}} \quad (\text{A.2})$$

$$\hat{g}(\vec{k}) = \int d^n x g(\vec{x}) e^{i\vec{x} \cdot \vec{k}} \quad (\text{A.3})$$

From these, we can see that the n-dimensional Dirac delta function can be written

$$\delta_D^n(\vec{x} - \vec{x}') = \frac{1}{(2\pi)^n} \int d^n k e^{-i\vec{k} \cdot (\vec{x} - \vec{x}')} \quad (\text{A.4})$$

such that

$$\int d^n x f(\vec{x}) \delta_D^n(\vec{x} - \vec{x}') = f(\vec{x}') \quad (\text{A.5})$$

We now define the Power Spectrum of g to be the Fourier transform of the auto-correlation function, which, due to isotropy, depends only on the magnitude of \vec{k} :

$$\begin{aligned} P_g(k) &= \int d^n x e^{-i\vec{x} \cdot \vec{k}} C_{gg}(x) \\ C_{gg}(x) &= \frac{1}{(2\pi)^n} \int d^n k e^{i\vec{x} \cdot \vec{k}} P_g(k) \end{aligned} \quad (\text{A.6})$$

A bit of math shows that the Power Spectrum is proportional to the Fourier-space correlation function:

$$\hat{C}_{gg}(\vec{k} - \vec{k}') \equiv \langle \hat{g}(\vec{k}) \hat{g}^*(\vec{k}') \rangle = (2\pi)^n \delta_D^n(\vec{k} - \vec{k}') P_g(|\vec{k}|). \quad (\text{A.7})$$

Along with isotropy and homogeneity, this result implies

$$P_g(k) \propto \langle |\hat{g}(k)|^2 \rangle. \quad (\text{A.8})$$

The proportionality constant is finite only for a discrete Fourier series (i.e. a finite averaging volume).

¹Note that the Fourier transform convention in eqns A.2-A.3 is useful in that it leads to a particularly simple form of the convolution theorem, without any gratuitous factors of $\sqrt{2\pi}$:

$$h(\vec{x}) = \int d^n x' f(\vec{x}') g(\vec{x} - \vec{x}') \quad \Longleftrightarrow \quad \hat{h}(\vec{k}) = \hat{f}(\vec{k}) \hat{g}(\vec{k})$$

A.1.1 Smoothing of Gaussian Fields

When measuring a realization of Gaussian field, we often make the measurement within a region defined by a window function $W(\vec{x}/R)$. By convention, we express window functions in terms of \vec{x}/R , where R is a characteristic length scale of the window. This window may reflect a sharp boundary in space (e.g. a spherical tophat function) or perhaps an observation efficiency in space (e.g. a 3D Gaussian). In either case, our observed overdensity is given by

$$g_W(\vec{x}) = \int d^n x' W\left(\frac{\vec{x}' - \vec{x}}{R}\right) g(\vec{x}') \quad (\text{A.9})$$

where $W(\vec{x}/R)$ is normalized such that

$$\int d^n x W(\vec{x}/R) = 1. \quad (\text{A.10})$$

This can be simplified if we can define the Fourier transform pair of a window function in the convention of equations A.2 and A.3 (cf. Liddle & Lyth 2000):

$$\begin{aligned} \widetilde{W}(\vec{k}R) &= \int W(\vec{x}/R) e^{i\vec{k}\cdot\vec{x}} d^n x \\ W(\vec{x}/R) &= \frac{1}{(2\pi)^n} \int \widetilde{W}(\vec{k}R) e^{-i\vec{k}\cdot\vec{x}} d^n k \end{aligned} \quad (\text{A.11})$$

This definition is convenient because, when combined with equation A.2, some straightforward algebra leads to the convolution theorem:

$$\hat{g}_W(\vec{k}) = \widetilde{W}(\vec{k}R) \hat{g}(\vec{k}) \quad (\text{A.12})$$

It is also useful to calculate the cross-correlation between two windows,

$$\langle g_{W_1}(\vec{x}_1) g_{W_2}^*(\vec{x}_2) \rangle = \int d^n x W_1\left(\frac{\vec{x} - \vec{x}_1}{R}\right) \int d^n x' W_2\left(\frac{\vec{x}' - \vec{x}_2}{R}\right) \langle g(\vec{x}) g^*(\vec{x}') \rangle \quad (\text{A.13})$$

Using equations A.6 and A.11, we can re-express equation A.13 as a single integral over the wave number:

$$\langle g_{W_1}(\vec{x}_1) g_{W_2}^*(\vec{x}_2) \rangle = \frac{1}{(2\pi)^n} \int d^n k P_g(k) \widetilde{W}_1(\vec{k}R) \widetilde{W}_2(\vec{k}R) e^{i\vec{k}\cdot(\vec{x}_1 - \vec{x}_2)} \quad (\text{A.14})$$

Appendix A.3 lists a few common window functions and their Fourier transforms.

A.2 Cosmological Mass Power Spectrum

In studies of the cosmological distribution of matter, we are interested in the comoving matter density $\rho(\vec{x})$, which defines the mass density at every comoving point \vec{x} in the universe. In order to take advantage of the preceding formalism, we can subtract the mean cosmological density $\bar{\rho}(\vec{x})$, and define a dimensionless density contrast $\delta(\vec{x})$, such that

$$\delta(\vec{x}) = \frac{\rho(\vec{x}) - \bar{\rho}(\vec{x})}{\bar{\rho}(\vec{x})}. \quad (\text{A.15})$$

By the assumptions of the Cosmological Principle, for small deviations $\delta(\vec{x})$ is an isotropic, homogeneous random field. We can better understand the distribution of $\delta(\vec{x})$ by looking at the mean square deviation

$$\begin{aligned} \langle |\delta(\vec{x})|^2 \rangle &= C_{\delta\delta}(0) \\ &= \frac{1}{(2\pi)^3} \int d^3k P_\delta(k) \\ &= \frac{1}{2\pi^2} \int k^2 dk P_\delta(k) \end{aligned} \quad (\text{A.16})$$

The power spectrum of density contrast given by equation A.6 can be an inconvenient quantity to work with, because it has dimensions of volume. We can take the lead from equation A.16 and define a dimensionless form of the power spectrum

$$\Delta^2(k) = \frac{k^3}{2\pi^2} P_\delta(k) \quad (\text{A.17})$$

This is constructed so that equation A.16 can be written in a simple form:

$$\langle |\delta(\vec{x})|^2 \rangle = \int_0^\infty \Delta^2(k) d(\ln k) \quad (\text{A.18})$$

This convention is due to Peacock (1999). For mathematical convenience, we'll continue to work with the $P_\delta(k)$ convention, with the understanding that we can switch back and forth any time using equation A.17.

A.2.1 Power Spectrum Normalization

In practice, the functional form of the power spectrum is determined only up to a proportionality constant, such that

$$P_\delta(k) = P_0 P'_\delta(k) \quad (\text{A.19})$$

where $P'_\delta(k)$ is the unnormalized form. For historical reasons, the normalization constant P_0 is commonly expressed in terms of the parameter σ_8 , which is defined as the mean density fluctuation within a sphere of radius 8 Mpc. To compute this, we use a top-hat window function:

$$W_T(\vec{x}/R) = \begin{cases} 1, & |\vec{x}|/R \leq 1 \\ 0, & |\vec{x}|/R > 1 \end{cases} \quad (\text{A.20})$$

The density fluctuation within this window is found using equation A.14:

$$\sigma_R^2 = \frac{1}{(2\pi)^3} \int d^3\vec{k} P_\delta(k) [\widetilde{W}_T(\vec{k}R)]^2 \quad (\text{A.21})$$

where the window function is assumed to be shallow enough that there is no cosmological evolution of the signal.

For the top-hat window function of equation A.20, with $k = |\vec{k}|$, the Fourier transform of equation A.20 (cf. eqn. A.11) is

$$\widetilde{W}_T(kR) = \frac{3}{(kR)^3} [\sin(kR) - kR \cos(kR)]. \quad (\text{A.22})$$

σ_8 can be calculated using equation A.21 and A.22 with $R = 8\text{Mpc}$ for a given $P_\delta(k)$. The WMAP 7-year measurement gives $\sigma_8 = 0.816 \pm 0.024$ (Komatsu et al., 2011). Using this value, the correct normalization can be computed for any functional form of the power spectrum.

A.2.2 Window functions and Measurement Covariance

In a 3D lensing analysis, we are searching for a signal within a series of windows defined as

$$W_{ij}(\vec{x}) = W_{ij}(\xi, \vec{\theta}) = q_i(\xi) \cdot F_j(\vec{\theta}) \quad (\text{A.23})$$

where ξ is the radial comoving distance, and $\vec{\theta}$ is the angular position on the sky. To convert between angle on the sky and projected comoving separation, we multiply by the transverse comoving distance (eqn. 16 in Hogg 1999), given by

$$f_\kappa(\xi) = \begin{cases} \kappa^{-1/2} \sin(\kappa^{1/2}\xi) & (\kappa > 0) \\ \xi & (\kappa = 0) \\ (-\kappa)^{-1/2} \sinh[(-\kappa)^{1/2}\xi] & (\kappa < 0) \end{cases} \quad (\text{A.24})$$

Our observed overdensity in window W_{ij} is given by

$$\begin{aligned}\delta_{ij} &= \int d^3x W_{ij}(\vec{x}) \delta(\vec{x}) \\ &= \int d\xi \int d^2\theta [f_\kappa(\xi)]^2 F_j(\vec{\theta}) q_i(\xi) \delta\left(f_\kappa(\xi) \vec{\theta}, \xi\right)\end{aligned}\quad (\text{A.25})$$

F_j is the function describing the shape of the j^{th} pixel, while q_i is the function describing the i^{th} redshift bin. These window functions should be normalized as in equation A.10, such that

$$\int d\xi [f_\kappa(w)]^2 q_i(\xi) = 1 \quad (\text{A.26})$$

and

$$\int d^2\theta F_j(\vec{\theta}) = 1 \quad (\text{A.27})$$

We are usually concerned with the covariance matrix of the signal, given by

$$\begin{aligned}[S_{\delta\delta}]_{nm} &= \langle \delta_{i_n j_n} \delta_{i_m j_m}^* \rangle \\ &= \int d^2\theta F_{j_n}[\vec{\theta}] \int d^2\theta' F_{j_m}[\vec{\theta}'] \\ &\quad \times \int d\xi [f_\kappa(\xi)]^2 q_{i_n}[\xi] \int d\xi' [f_\kappa(\xi')]^2 q_{i_m}[\xi'] \\ &\quad \times \left\langle \delta\left(f_\kappa(\xi) \vec{\theta}, \xi\right) \delta^*\left(f_\kappa(\xi') \vec{\theta}', \xi'\right) \right\rangle\end{aligned}\quad (\text{A.28})$$

This can be simplified using the Limber approximation.

A.2.3 The Limber Approximation

Consider a projection of the density field along a certain radial direction

$$g_i(\vec{\theta}) = \int d\xi p_i(\xi) \delta\left(f_\kappa(\xi) \vec{\theta}, \xi\right). \quad (\text{A.29})$$

The cross correlation is

$$\begin{aligned}S_{g_i g_j}(\vec{\theta} - \vec{\theta}') &= \langle g_i(\vec{\theta}) g_j^*(\vec{\theta}') \rangle \\ &= \int d\xi p_i(\xi) \int d\xi' p_j(\xi') \left\langle \delta[f_\kappa(\xi) \vec{\theta}, \xi] \delta^*[f_\kappa(\xi') \vec{\theta}', \xi'] \right\rangle\end{aligned}\quad (\text{A.30})$$

Let's express $\delta(\vec{x})$ in terms of the Fourier integral, equation A.2. This gives

$$\begin{aligned}S_{g_i g_j}(\vec{\theta} - \vec{\theta}') &= \int d\xi p_i(\xi) \int d\xi' p_j(\xi') \int \frac{d^3k}{(2\pi)^3} \int \frac{d^3k'}{(2\pi)^3} \left\langle \hat{\delta}(\vec{k}, \xi) \hat{\delta}^*(\vec{k}', \xi') \right\rangle \\ &\quad \times \exp\left[-i f_\kappa(\xi) \vec{\theta} \cdot \vec{k}_\perp - i k_\parallel w\right] \exp\left[i f_\kappa(\xi') \vec{\theta}' \cdot \vec{k}'_\perp + i k'_\parallel w'\right].\end{aligned}\quad (\text{A.31})$$

Here \vec{k}_\perp is the 2-dimensional projection of \vec{k} perpendicular to the line of sight, and k_\parallel is the projection of \vec{k} along the line of sight. The second argument of $\hat{\delta}(\vec{k}, \xi)$ parametrizes evolution with time via $|c \cdot dt| = a \cdot d\xi$.

Because the power spectrum $P_\delta(k)$ decreases linearly with k as $k \rightarrow 0$, there must be a coherence scale L_c such that the correlation is near zero for $|\xi - \xi'| \equiv \Delta\xi > L_c$. The first part of the Limber approximation is to assume that S_{gg} vanishes at these distances. Next we make the assumption that $p_i(\xi)$ and $p_j(\xi')$ do not vary appreciably over the small range where $S_{g_i g_j}$ is non-vanishing, and that this range is small enough that $f_\kappa(\xi) \approx f_\kappa(\xi')$. This allows us to rewrite the above expression in a simpler way:

$$\begin{aligned} S_{g_i g_j}(\vec{\theta} - \vec{\theta}') &= \int d\xi p_i(\xi) p_j(\xi) \int \frac{d^3 k}{(2\pi)^3} \int \frac{d^3 k'}{(2\pi)^3} \langle \hat{\delta}(\vec{k}, \xi) \hat{\delta}^*(\vec{k}', \xi) \rangle \\ &\quad \times \exp \left[-i f_\kappa(\xi) (\vec{\theta} \cdot \vec{k}_\perp - \vec{\theta}' \cdot \vec{k}'_\perp) - i \xi k_\parallel \right] \int d\xi' \exp(i \xi k'_\parallel) \end{aligned} \quad (\text{A.32})$$

The integral over ξ' is simply $2\pi \delta_D(k'_\parallel)$ via equation A.4, and the Fourier space correlation function is proportional to $P_\delta(k) \delta_D^3(\vec{k} - \vec{k}')$ via equation A.7:

$$\begin{aligned} S_{g_i g_j}(\vec{\theta} - \vec{\theta}') &= \int d\xi p_i(\xi) p_j(\xi) \int \frac{d^3 k}{(2\pi)^2} \int d^3 k' \delta_D^3(\vec{k} - \vec{k}') \delta_D(k'_\parallel) P_\delta(k) \\ &\quad \times \exp \left[-i f_\kappa(\xi) (\vec{\theta} \cdot \vec{k}_\perp - \vec{\theta}' \cdot \vec{k}'_\perp) - i \xi k_\parallel \right] \end{aligned} \quad (\text{A.33})$$

Carrying out the integrals over the two delta functions we see

$$S_{g_i g_j}(\vec{\theta}_{ij}) = \int d\xi p_i(\xi) p_j(\xi) \int \frac{d^2 k_\perp}{(2\pi)^2} P_\delta(k_\perp, \xi) \exp \left[-i f_\kappa(\xi) \vec{\theta}_{ij} \cdot \vec{k}_\perp \right] \quad (\text{A.34})$$

$$= \int d\xi p_i(\xi) p_j(\xi) \int \frac{k dk}{2\pi} P_\delta(k, \xi) J_0[f_\kappa(\xi) \theta k] \quad (\text{A.35})$$

where we have defined $\vec{\theta}_{ij} = \vec{\theta} - \vec{\theta}'$, and $J_0(x)$ is a Bessel function of the first kind, which comes from the angular integral via

$$J_n(x) = \frac{1}{2\pi} \int_{-\pi}^{\pi} e^{-i(n\tau - x \sin \tau)} d\tau \quad (\text{A.36})$$

We see that all k_\parallel terms have vanished, which leads to the main result of the Limber approximation: there is no correlation between the density contrast in windows that do not overlap in redshift. This is quickly seen from the leading integral in equation A.34. If the windows $p_i(\xi)$ and $p_j(\xi)$ do not overlap, then the expression integrates to zero.

Now that we have a simple expression for the 2-dimensional projected correlation functions, we can use equation A.6 to define the 2-dimensional cross power spectrum of the measured covariance,

$$P_{g_i g_j}(\ell) = \int d^2\theta e^{i\vec{\theta} \cdot \vec{\ell}} S_{g_i g_j}(\vec{\theta}). \quad (\text{A.37})$$

Combining equations A.34 and A.37, we have

$$\begin{aligned} P_{g_i g_j}(\ell) &= \int d^2\theta \int d\xi p_i(\xi) p_j(\xi) \int \frac{d^2 k_\perp}{(2\pi)^2} P_\delta(k_\perp, \xi) \exp \left[i\vec{\theta} \cdot (\vec{\ell} - f_\kappa(\xi) \vec{k}_\perp) \right] \\ &= \int d\xi p_i(\xi) p_j(\xi) \int d^2 k_\perp P_\delta(k_\perp, \xi) \delta_D^2(\vec{\ell} - f_\kappa(\xi) \vec{k}_\perp) \\ &= \int d\xi \frac{p_i(\xi) p_j(\xi)}{[f_\kappa(\xi)]^2} P_\delta \left(\frac{\ell}{f_\kappa(\xi)}, \xi \right). \end{aligned} \quad (\text{A.38})$$

A.2.4 Applying the Limber Approximation

Examining equation A.28, we see that the integrals over ξ and ξ' appear in equation A.30, with $p_i(\xi) \rightarrow q_{i_n}(\xi)[f_\kappa(\xi)]^2$ and $p_j(\xi') \rightarrow q_{i_m}(\xi')[f_\kappa(\xi')]^2$. Thus we can rewrite equation A.28 using the Limber approximation:

$$[S_{\delta\delta}]_{nm} = \int d^2\theta F_{j_n}[\vec{\theta}] \int d^2\theta' F_{j_m}[\vec{\theta}'] S_{nm}(\vec{\theta} - \vec{\theta}') \quad (\text{A.39})$$

Now using the procedure from section A.1.1, we can write this approximation as an integral in Fourier space over the cross power spectrum given by equation A.38. We'll consider the simple case where each pixel has the same angular shape described by $F(\vec{\theta})$, so that $F_{j_n}(\vec{\theta}) = F(\vec{\theta} - \vec{\theta}_n)$ and $F_{j_m}(\vec{\theta}) = F(\vec{\theta} - \vec{\theta}_m)$. Defining $\vec{\theta}_{nm} = |\vec{\theta}_n - \vec{\theta}_m|$,

$$\begin{aligned} [S_{\delta\delta}]_{nm} &= \frac{1}{(2\pi)^2} \int d^2\ell \tilde{F}_{j_n}(\vec{\ell}) \tilde{F}_{j_m}(\vec{\ell}) P_{nm}(\ell) e^{i\vec{\ell} \cdot \vec{\theta}_{nm}} \\ &= \frac{1}{2\pi} \int \ell d\ell \tilde{F}_{j_n}(\ell) \tilde{F}_{j_m}(\ell) P_{nm}(\ell) J_0(\ell \theta_{nm}) \end{aligned} \quad (\text{A.40})$$

where the second line holds if the window functions are circularly symmetric, with the Bessel function given by equation A.36. The projected power spectrum $P_{nm}(\vec{\ell})$ is given by equation A.38 with appropriate substitution for $p_{i,j}$:

$$P_{nm}(\ell) = \int d\xi [f_\kappa(\xi)]^2 q_{i_n}(\xi) q_{i_m}(\xi) P_\delta \left(\frac{\ell}{f_\kappa(\xi)}, \xi \right). \quad (\text{A.41})$$

Note the factor of $[f_\kappa(\xi)]^2$ in the numerator, which has its root in the spherical coordinate differential $d^3x \rightarrow r^2 dr \cdot d\Omega$.

Our main application of this formalism will involve discrete non-overlapping redshift bins with uniform weighting. That is,

$$q_i(\xi) = \begin{cases} A_i, & \xi_{\min}^{(i)} < \xi < \xi_{\max}^{(i)} \\ 0, & \text{otherwise} \end{cases} \quad (\text{A.42})$$

with the normalization constant computed via the condition in equation A.26:

$$A_i = \left[\int_{\xi_{\min}^{(i)}}^{\xi_{\max}^{(i)}} [f_\kappa(\xi)]^2 d\xi \right]^{-1}. \quad (\text{A.43})$$

To summarize, the correlation between two windows n and m becomes, with $i_{n,m}$ indexing the redshift window, and n, m indexing the angular window,

$$\begin{aligned} [S_{\delta\delta}]_{nm} &= \delta_{i_n i_m}^K \omega(|\theta_{nm}|) \\ \omega(\theta) &= \frac{1}{2\pi} \int_0^\infty \ell d\ell |\tilde{F}(\ell)|^2 P_{nm}(\ell) J_0(\ell\theta) \\ P_{nm}(\ell) &= \frac{1}{A^2} \int_{\xi_{\min}^{(i)}}^{\xi_{\max}^{(i)}} d\xi [f_\kappa(\xi)]^2 P_\delta\left(\frac{\ell}{f_\kappa(\xi)}, \xi\right). \\ A &= \int_{\xi_{\min}^{(i)}}^{\xi_{\max}^{(i)}} d\xi [f_\kappa(\xi)]^2 \end{aligned} \quad (\text{A.44})$$

where δ_{ij}^K is the Kronecker delta. This result should be compared to equations 39-41 of Simon et al. (2009). The only difference is that we have correctly accounted for the normalization of the redshift bin. Note that if we assume $f_\kappa(\xi)$ is constant across each redshift bin, the two formulations are equivalent.

For our analysis, we will use angular pixels with radius θ_s , so that the Fourier transform of the window function is given by equation A.51 and the equation giving the signal covariance becomes

$$[S_{\delta\delta}]_{nm} = \frac{2}{\pi\theta_s^2} \int d\xi \frac{q_{i_n}[\xi] q_{i_m}[\xi]}{f_\kappa(\xi)^2} \int \frac{d\ell}{\ell} P_\delta\left(\frac{\ell}{f_\kappa(\xi)}, \xi\right) [J_1(\theta_s \ell)]^2 J_0(\theta_{nm} \ell) \quad (\text{A.45})$$

A.3 Window Functions and their Fourier Transforms

Here we list a few common window functions and their Fourier transforms

A.3.1 Gaussian Window Functions

The n -dimensional Gaussian window function is defined as

$$W(\vec{x}/R) = \frac{1}{(2\pi R^2)^{n/2}} \exp\left(\frac{-|\vec{x}|^2}{2R^2}\right) \quad (\text{A.46})$$

The Fourier transform is straightforward because the dimensions decouple and we're left with n 1-dimensional Gaussian integrals. The resulting window function is

$$\widetilde{W}(\vec{k}R) = \exp\left(\frac{-|\vec{k}|^2 R^2}{2}\right) \quad (\text{A.47})$$

which itself is a Gaussian.

A.3.2 Top-hat Window Functions

The n -dimensional tophat window function is given by

$$W(\vec{x}/R) = A_n \times \begin{cases} 1, & |\vec{x}| \leq R \\ 0, & |\vec{x}| > R \end{cases} \quad (\text{A.48})$$

with

$$A_n = \frac{\Gamma(n/2 + 1)}{(R\sqrt{\pi})^n} \quad (\text{A.49})$$

where $\Gamma(y)$ is the gamma function. The normalization is simply the inverse of the volume of an n -sphere of radius R . For $n = 2$ and $n = 3$, the normalizations are the familiar $1/(\pi R^2)$ and $3/(4\pi R^3)$, respectively. For the top-hat window function, there is no simple expression for the Fourier transform for arbitrary n . Here we compute three special cases:

$n = 1$:

$$\begin{aligned} A_1 &= (2R)^{-1} \\ \widetilde{W}(\vec{k}R) &= A_1 \int_{-R}^R dr e^{ikr} \\ &= \frac{\sin(kR)}{kR} \end{aligned} \quad (\text{A.50})$$

$n = 2$:

$$\begin{aligned}
 A_2 &= (\pi R^2)^{-1} \\
 \widetilde{W}(\vec{k}R) &= A_2 \int_0^R r dr \int_0^{2\pi} \exp[ikr \cos \phi] d\phi \\
 &= \frac{2}{R^2} \int_0^R r J_0(kr) dr \\
 &= \frac{2J_1(kR)}{kR}
 \end{aligned} \tag{A.51}$$

$n = 3$:

$$\begin{aligned}
 A_3 &= (4\pi R^3/3)^{-1} \\
 \widetilde{W}(\vec{k}R) &= A_3 \int_0^R r^2 dr \int_0^\pi \sin(\theta) d\theta \int_0^{2\pi} \exp[ikr \cos \phi] d\phi \\
 &= \frac{3}{R^3} \int_0^R r^2 J_0(kr) dr \\
 &= {}_1F_2\left(\frac{1}{2}; 1, \frac{5}{2}; -\frac{k^2 R^2}{4}\right)
 \end{aligned} \tag{A.52}$$

where, $J_n(x)$ are Bessel functions of the first kind (see eqn A.36) and the last line is a generalized hypergeometric function, ${}_nF_m(a_0 \cdots a_n; b_0 \cdots b_m; x)$.

Appendix B

EFFICIENT IMPLEMENTATION OF THE SVD ESTIMATOR

As noted in Section 3.2.2, taking the SVD of the transformation matrix $\widetilde{M}_{\gamma\delta} \equiv \mathcal{N}_{\gamma\gamma}^{-1/2} M_{\gamma\delta}$ is not trivial for large fields. This appendix will first give a rough outline of the form of $M_{\gamma\delta}$, then describe our tensor decomposition method which enables quick calculation of the singular value decomposition. For a more thorough review of the lensing results, see e.g. Bartelmann & Schneider (2001).

Our goal is to speed the computation of the SVD by writing $\widetilde{M}_{\gamma\delta}$ as a tensor product $\mathbf{A} \otimes \mathbf{B}$. Here “ \otimes ” is the Kronecker product, defined such that, if \mathbf{A} is a matrix of size $n \times m$, \mathbf{B} is a matrix of arbitrary size,

$$\mathbf{A} \otimes \mathbf{B} \equiv \begin{pmatrix} A_{11}B & A_{12}B & \cdots & A_{1m}B \\ A_{21}B & A_{22}B & \cdots & A_{2m}B \\ \vdots & \vdots & \ddots & \vdots \\ A_{n1}B & A_{n2}B & \cdots & A_{nm}B \end{pmatrix} \quad (\text{B.1})$$

In this case, the singular value decomposition $\mathbf{A} \otimes \mathbf{B} = U_{AB} \Sigma_{AB} V_{AB}^\dagger$ satisfies

$$\begin{aligned} U_{AB} &= U_A \otimes U_B \\ \Sigma_{AB} &= \Sigma_A \otimes \Sigma_B \\ V_{AB} &= V_A \otimes V_B \end{aligned} \quad (\text{B.2})$$

where $U_A \Sigma_A V_A^\dagger$ is the SVD of A , and $U_B \Sigma_B V_B^\dagger$ is the SVD of B . Decomposing $\widetilde{M}_{\gamma\delta}$ in this way can greatly speed the SVD computation.

B.0.3 Angular and Line-of-Sight Transformations

The transformation from shear to density, encoded in $M_{\gamma\delta}$, consists of two steps: an angular integral relating shear γ to convergence κ , and a line-of-sight integral relating the convergence κ to the density contrast δ .

The relationship between γ and κ is a convolution over all angular scales,

$$\gamma(\boldsymbol{\theta}, z_s) \equiv \gamma_1 + i\gamma_2 = \int d^2\theta' \mathcal{D}(\boldsymbol{\theta}' - \boldsymbol{\theta}) \kappa(\boldsymbol{\theta}', z_s), \quad (\text{B.3})$$

where $\mathcal{D}(\boldsymbol{\theta})$ is the Kaiser-Squires kernel (Kaiser & Squires, 1993). This has a particularly simple form in Fourier space:

$$\hat{\gamma}(\boldsymbol{\ell}, z_s) = \frac{\ell_1 + i\ell_2}{\ell_1 - i\ell_2} \hat{\kappa}(\boldsymbol{\ell}, z_s). \quad (\text{B.4})$$

where $\hat{\gamma}$ and $\hat{\kappa}$ are the Fourier transforms of γ and κ and $\boldsymbol{\ell} \equiv (\ell_1, \ell_2)$ is the angular wavenumber.

The relationship between κ and δ is an integral along each line of sight:

$$\kappa(\boldsymbol{\theta}, z_s) = \int_0^{z_s} dz W(z, z_s) \delta(\boldsymbol{\theta}, z) \quad (\text{B.5})$$

where $W(z, z_s)$ is the lensing efficiency function at redshift z for a source located at redshift z_s (refer to STH09 for the form of this function).

Upon discretization of the quantities γ , κ , and δ (described in Section 3.2.1), the integrals in Equations B.3-B.5 become matrix operations. The relationship between the data vectors $\boldsymbol{\gamma}$ and $\boldsymbol{\kappa}$ can be written

$$\boldsymbol{\gamma} = [\mathbf{P}_{\gamma\kappa} \otimes \mathbf{1}_s] \boldsymbol{\kappa} + \mathbf{n}_\gamma \quad (\text{B.6})$$

where $\mathbf{1}_s$ is the $N_s \times N_s$ identity matrix and $\mathbf{P}_{\gamma\kappa}$ is the matrix representing the linear transformation in Equations B.3-B.4. The quantity $[\mathbf{P}_{\gamma\kappa} \otimes \mathbf{1}_s]$ simply denotes that $\mathbf{P}_{\gamma\kappa}$ operates on each of the N_s source-planes represented within the vector $\boldsymbol{\kappa}$. Similarly, the relationship between the vectors $\boldsymbol{\kappa}$ and $\boldsymbol{\delta}$ can be written

$$\boldsymbol{\kappa} = [\mathbf{1}_{xy} \otimes \mathbf{Q}_{\kappa\delta}] \boldsymbol{\delta} \quad (\text{B.7})$$

where $\mathbf{1}_{xy}$ is the $N_{xy} \times N_{xy}$ identity matrix, and the tensor product signifies that the operator $\mathbf{Q}_{\kappa\delta}$ operates on each of the N_{xy} lines-of-sight in $\boldsymbol{\delta}$. $\mathbf{Q}_{\kappa\delta}$ is the $N_s \times N_l$ matrix which represents the discretized version of equation B.5. Combining these representations allows us to decompose the matrix $\mathbf{M}_{\gamma\delta}$ in Equation 3.1 into a tensor product:

$$\mathbf{M}_{\gamma\delta} = \mathbf{P}_{\gamma\kappa} \otimes \mathbf{Q}_{\kappa\delta}. \quad (\text{B.8})$$

B.0.4 Tensor Decomposition of the Transformation

We now make an approximation that the noise covariance $\mathcal{N}_{\gamma\gamma}$ can be written as a tensor product between its angular part \mathcal{N}_P and its line of sight part \mathcal{N}_Q :

$$\mathcal{N}_{\gamma\gamma} = \mathcal{N}_P \otimes \mathcal{N}_Q. \quad (\text{B.9})$$

Because shear measurement error comes primarily from shot noise, this approximation is equivalent to the statement that source galaxies are drawn from a single redshift distribution, with a different normalization along each line-of-sight. For realistic data, this approximation will break down as the size of the pixels becomes very small. We will assume here for simplicity that the noise covariance is diagonal, but the following results can be generalized for non-diagonal noise. Using this noise covariance approximation, we can compute the SVDs of the components of $\widetilde{M}_{\gamma\delta}$:

$$\begin{aligned} U_P \Sigma_P V_P^\dagger &= \mathcal{N}_P^{-1/2} P_{\gamma\kappa} \\ U_Q \Sigma_Q V_Q^\dagger &= \mathcal{N}_Q^{-1/2} Q_{\kappa\delta} \end{aligned} \quad (\text{B.10})$$

In practice the SVD of the matrix $P_{\gamma\kappa}$ need not be computed explicitly. $P_{\gamma\kappa}$ encodes the discrete linear operation expressed by Equations B.3-B.4: as pointed out by STH09, in the large-field limit $P_{\gamma\kappa}$ can be equivalently computed in either real or Fourier space. Thus to operate with $P_{\gamma\kappa}$ on a shear vector, we first take the 2D Fast Fourier Transform (FFT) of each source-plane, multiply by the kernel $(\ell_1 + i\ell_2)/(\ell_1 - i\ell_2)$, then take the inverse FFT of the result. This is orders-of-magnitude faster than a discrete implementation of the real-space convolution. Furthermore, the conjugate transpose of this operation can be computed by transforming $\ell \rightarrow -\ell^*$, so that

$$P_{\gamma\kappa}^\dagger P_{\gamma\kappa} = I \quad (\text{B.11})$$

and we see that $P_{\gamma\kappa}$ is unitary in the wide-field limit. This fact, along with the tensor product properties of the SVD, allows us to write $\widetilde{M}_{\gamma\delta} = U \Sigma V^\dagger$ where

$$\begin{aligned} U &\approx \mathbf{1}_{xy} \otimes U_Q \\ \Sigma &\approx \mathcal{N}_P^{-1/2} \otimes \Sigma_Q \\ V^\dagger &\approx P_{\gamma\kappa} \otimes V_Q^\dagger \end{aligned} \quad (\text{B.12})$$

The only explicit SVD we need to calculate is that of $\mathcal{N}_Q^{-1/2} \mathbf{Q}_{\kappa\delta}$, which is trivial in cases of interest. The two approximations we have made are the applicability of the Fourier-space form of the $\gamma \rightarrow \kappa$ mapping (Eqn. B.4), and the tensor decomposition of the noise covariance (Eqn. B.9).

Appendix C

CHOICE OF KL PARAMETERS

The KL analysis outlined in Section 4.2 has only two free parameters: the number of modes n and the Wiener filtering level α . Each of these parameters involves a trade-off: using more modes increases the amount of information used in the reconstruction, but at the expense of a decreased signal-to-noise ratio. Decreasing the value of α to 0 reduces the smoothing effect of the prior, but can lead to a nearly singular convolution matrix $\mathbf{M}_{(n,\alpha)}$, which results in unrealistically large shear values in the poorly-constrained areas of the map (i.e. masked regions).

To inform our choice of the number of modes n , we recall the trend of spatial scale with mode number seen in Figure 4.2. Our purpose in using KL is to allow interpolation in masked regions. To this end, the angular scale of the mask should inform the choice of angular scale of the largest mode used. An eigenmode which probes scales much smaller than the size of a masked region will not contribute meaningful information to the reconstruction within that masked region. Considering the pixels within our mask, we find that 99.5% of masked pixels are within 2 pixels of a shear measurement. This corresponds to an angular scale of $\ell = 6140$. Consulting Figure 4.2, we see that modes larger than about $n = 900$ out of 4096 will probe length scales significantly smaller than the mask scale. Thus, we choose $n = 900$ as an appropriate cutoff for our reconstructions.

To inform our choice of the Wiener filtering level α , we examine the agreement between histograms of M_{ap} peaks for a noise-only DES field with and without masking (see Section 4.4). We find that for large (small) values of α , the number of high- M_{ap} peaks is underestimated (overestimated) in the masked case as compared to the unmasked case. Empirically, we find that the two agree at $\alpha = 0.15$; we choose this value for our analysis. Note that this tuning is done on noise-only reconstructions, which can be generated for

observed data by assuming that shape noise dominates:

$$[\mathcal{N}_\gamma]_{ij} = \frac{\sigma_\epsilon}{n_i^2} \delta_{ij}. \quad (\text{C.1})$$

The α -tuning can thus be performed on artificial noise realizations which match the observed survey characteristics.

We make no claim that $(n, \alpha) = (900, 0.15)$ is the optimal choice of free parameters for KL: determining this would involve a more in-depth analysis. They are simply well-motivated choices which we use to make a case for further study.

CURRICULUM VITAE

Jacob T. Vanderplas

Education

- 2012: PhD in Astronomy *University of Washington*, Seattle WA
 2008: MSc in Astronomy *University of Washington*, Seattle WA
 2003: BSc in Physics *Calvin College*, Grand Rapids, MI

Professional Experience

- 2006-2012: Graduate research assistant. *University of Washington*, Seattle WA
 Advised by:
 Andrew Connolly: 2008-2012
 Bhuvnesh Jain (U. Penn): 2009-2012
 Andrew Becker: 2006-2008
 Craig Hogan: 2006-2007
- 2010-2012: Planetarium Digitization Project Coordinator
 University of Washington, Seattle, WA
- 2008-2010: Planetarium Educational Outreach Coordinator
 University of Washington, Seattle, WA
- 2006-2008: Graduate teaching assistant, introductory Astronomy
 University of Washington, Seattle, WA
- 2004-2006: Experiential Science Educator
 Mount Hermon Outdoor Science School, Santa Cruz, CA
- 2004-2006: Mountaineering Instructor
 Summit Adventure, Bass Lake, CA

Volunteer Experience

2009-2012: Science Communication Fellow

Pacific Science Center, Seattle WA

2007-2012: Trip Leader for Inner-city Youth

Sierra Club Inner City Outings, Seattle WA

Non-technical and Public Talks

2009-2012: “Scientist Spotlight” and “Portal to the Public” events,
(3-4 times per year)

Pacific Science Center, Seattle WA

April 2012: Colloquium: *Dark Matter, Dark Energy, and the Fate of the Universe*
Calvin College, Grand Rapids, MI

November 2011: Invited talk: Gravity, Lensing the Universe
KCTS9 Science Cafe, Seattle WA

June 2010 - Nov. 2011: Invited World Wide Telescope demonstrations (Microsoft)
Supercomputing 2011, Seattle WA
Partners in Learning Global Forum 2011, Washington DC
Popular Mechanics Breakthrough Awards 2011, New York NY
ISTE 2010, Denver CO

March 2011: Invited Talk: Understanding the Dark Side of the Universe
Science with a Twist: Star Wars
Pacific Science Center, Seattle WA

February 2011: Talk: Interconnection in Art and Cosmology
Astronomy-inspired art show, University of Washington

May 2009: Dark Matter, Gravitational Lensing, and Cosmology
Battle Point Astronomical Society, Bainbridge Island WA

Technical Talks & Presentations

- July 2012: Tutorial: Machine Learning in Python
 Talk: **astroML**: Machine Learning for Astronomy
 Scipy 2012, Austin TX
- March 2012: Invited tutorial: Scientific Machine Learning with **scikit-learn**
 PyData 2012, Mountain View CA
- December 2011: Poster: Shear Mapping with Karhunen-Loeve Analysis
 NIPS 2011, Grenada, Spain
- June 2011: Invited talk: Digital Planetariums for the Masses
 AstroViz 2011, Seattle WA
- April-May 2011: Talk: KL Interpolation of Weak Lensing Shear
 INPA Seminar, Lawrence Berkeley National Laboratory
 Cosmology Seminar, UC Davis
 KIPAC Cosmology Seminar, Stanford University/SLAC
- February 2011: Talk: Weak Lensing Peak Statistics
 Cosmology Seminar, University of Pennsylvania
- January 2011: Poster: Finding the Odd-one Out in Spectroscopic Surveys
 Poster: 3D Reconstruction of the Density Field
 217th AAS meeting, Seattle WA
- July 2010: Talk: A New Approach to Tomographic Mapping
 Ten Years of Cosmic Shear, Edinburgh, UK
- April 2010: Talk: New Ideas for 3D Mapping with Cosmic Shear
 Cosmology Seminar, University of Pennsylvania
- October 2009: Talk: Locally Linear Embedding of Astronomy Data
 Microsoft Research, Redmond, WA
- November 2007: Invited talk: SALT-2 Light-curve Fitting for SDSS Supernovae
 SDSS Collaboration Meeting, Fermilab

Publication List

1. **VanderPlas, J. T.**; Connolly, A. J.; Jain, B.; Jarvis, M.
Interpolating Masked Weak-lensing Signal with Karhunen-Love Analysis. ApJ 744:180 (2012)
2. Pedregosa, Fabian; Varoquaux, Gal; Gramfort, Alexandre; Michel, Vincent; Thirion, Bertrand; Grisel, Olivier; Blondel, Mathieu; Prettenhofer, Peter; Weiss, Ron; Dubourg, Vincent; **Vanderplas, Jake**; Passos, Alexandre; Cournapeau, David; Brucher, Matthieu; Perrot, Matthieu; Duchesnay, douard.
Scikit-learn: Machine Learning in Python. JMLR, 12:2825 (2011)
3. Xiong, L.; Poczos, B.; Schneider, J.; Connolly, A.; **VanderPlas, J.**
Hierarchical Probabilistic Models for Group Anomaly Detection. AISTATS (2011)
4. Jain, Bhuvnesh; **VanderPlas, Jake.**
Tests of modified gravity with dwarf galaxies JCAP 10:32 (2011)
5. Daniel, Scott F.; Connolly, Andrew; Schneider, Jeff; **Vanderplas, Jake**; Xiong, Liang.
Classification of Stellar Spectra with Local Linear Embedding. AJ 142:203 (2011)
6. **VanderPlas, J. T.**; Connolly, A. J.; Jain, B.; Jarvis, M.
Three-dimensional Reconstruction of the Density Field: An SVD Approach to Weak-lensing Tomography. ApJ 727:118 (2011)
7. Lampeitl, H.; Nichol, R. C.; Seo, H.-J.; Giannantonio, T.; Shapiro, C.; Bassett, B.; Percival, W. J.; Davis, T. M.; Dilday, B.; Frieman, J.; Garnavich, P.; Sako, M.; Smith, M.; Sollerman, J.; Becker, A. C.; Cinabro, D.; Filippenko, A. V.; Foley, R. J.; Hogan, C. J.; Holtzman, J. A.; Jha, S. W.; Konishi, K.; Marriner, J.; Richmond, M. W.; Riess, A. G.; Schneider, D. P.; Stritzinger, M.; van der Heyden, K. J.; **Vanderplas, J. T.**; Wheeler, J. C.; heng, C.

First-year Sloan Digital Sky Survey-II supernova results: consistency and constraints with other intermediate-redshift data sets. MNRAS 401:2331 (2010)

8. LSST Science Collaboration

LSST Science Book. arXiv:0912.0201 (2009)

9. Kessler, Richard; Becker, Andrew C.; Cinabro, David; **Vanderplas, Jake**; Frieman, Joshua A.; Marriner, John; Davis, Tamara M.; Dilday, Benjamin; Holtzman, Jon; Jha, Saurabh W.; Lampeitl, Hubert; Sako, Masao; Smith, Mathew; Zheng, Chen; Nichol, Robert C.; Bassett, Bruce; Bender, Ralf; Depoy, Darren L.; Doi, Mamoru; Elson, Ed; Filippenko, Alexei V.; Foley, Ryan J.; Garnavich, Peter M.; Hopp, Ulrich; Ihara, Yutaka; Ketzeback, William; Kollatschny, W.; Konishi, Kohki; Marshall, Jennifer L.; McMillan, Russet J.; Miknaitis, Gajus; Morokuma, Tomoki; Mrtzell, Edvard; Pan, Kaike; Prieto, Jose Luis; Richmond, Michael W.; Riess, Adam G.; Romani, Roger; Schneider, Donald P.; Sollerman, Jesper; Takanashi, Naohiro; Tokita, Kouichi; van der Heyden, Kurt; Wheeler, J. C.; Yasuda, Naoki; York, Donald.

First-Year Sloan Digital Sky Survey-II Supernova Results: Hubble Diagram and Cosmological Parameters. ApJS 185:32 (2009)

10. **Vanderplas, Jake**; Connolly, Andrew.

Reducing the Dimensionality of Data: Locally Linear Embedding of Sloan Galaxy Spectra. AJ 138:1365 (2009)

11. Sollerman, J.; Mrtzell, E.; Davis, T. M.; Blomqvist, M.; Bassett, B.; Becker, A. C.; Cinabro, D.; Filippenko, A. V.; Foley, R. J.; Frieman, J.; Garnavich, P.; Lampeitl, H.; Marriner, J.; Miquel, R.; Nichol, R. C.; Richmond, M. W.; Sako, M.; Schneider, D. P.; Smith, M.; **Vanderplas, J. T.**; Wheeler, J. C.

First-Year Sloan Digital Sky Survey-II (SDSS-II) Supernova Results: Constraints on Nonstandard Cosmological Models. ApJ 703:1374 (2009)

12. Kessler, Richard; Bernstein, Joseph P.; Cinabro, David; Dilday, Benjamin; Frieman,

Joshua A.; Jha, Saurabh; Kuhlmann, Stephen; Miknaitis, Gajus; Sako, Masao; Taylor, Matt; **Vanderplas, Jake**. *SNANA: A Public Software Package for Supernova Analysis*.

PASP 121:1028 (2009)